

Dissertation
submitted to the
Combined Faculties of the Natural Sciences and for Mathematics
of the Ruperto-Carola University of Heidelberg, Germany
for the degree of
Doctor of Natural Sciences

put forward by
M.Sc. Mario Alexander Nachbar
Born in: Wangen i.Allg. (Germany)
Oral examination: 13.06.2018

The microphysics of mesospheric cloud formation

on Earth and Mars

-

Laboratory experiments

Referees: Prof. Dr. Thomas Leisner
Prof. Dr. Klaus Pfeilsticker

Abstract

Polar Mesospheric Clouds (PMCs) are H₂O ice clouds occurring at high latitudes in the summer mesopause of Earth. They have a counterpart in the mesosphere of Mars consisting of CO₂ ice particles. Both types of clouds most likely form via heterogeneous nucleation on nanometer-sized meteoric smoke particles. However, the onset conditions for ice particle formation are only poorly known. Therefore, I investigated the microphysical formation process of these clouds in the laboratory. Experiments on adsorption, nucleation and growth processes of H₂O and CO₂ molecules on meteoric smoke analogue particles were performed using the MICE-TRAPS setup. For Earth, it was found that amorphous solid water is the primary phase which forms under the extreme temperatures of the summer mesopause. The vapor pressure of this ice phase was measured and is 2 to 4 times higher than previously assumed. Nevertheless, ice formation is activated at low supersaturation, which is described by a newly developed activation model. In contrast, CO₂ ice formation on Mars initiates at high supersaturation, which is described using classical nucleation theory with the parameters determined in this work. The results presented in this dissertation significantly enhance the understanding of mesospheric ice cloud formation on Earth and Mars.

Zusammenfassung

Im Sommer lassen sich auf der Erde Wassereiswolken in der Mesopause beobachten. Erstaunlicherweise bilden sich ähnliche Wolken in der Mesosphäre des Mars, welche jedoch aus CO₂ bestehen. Beide Arten von Wolken bilden sich höchstwahrscheinlich durch heterogene Nukleation auf Nanometer großen Meteoritenstaub-Partikeln. Unter welchen Bedingungen die Bildung von Eispartikeln einsetzt, ist jedoch kaum bekannt. Deshalb beschäftige ich mich in dieser Arbeit mit dem mikrophysikalischen Entstehungsprozess dieser Wolken. Mit Hilfe des MICE-TRAPS Aufbaus wurden experimentell die Adsorptions-, Nukleations- und Wachstumsprozesse von H₂O und CO₂ Molekülen auf Meteoritenstaub-Analoga untersucht. Die Ergebnisse für H₂O zeigen, dass sich unter den extrem kalten Temperaturen der Sommer-Mesopause amorphes Eis bildet. Der Dampfdruck dieser Eisphase wurde gemessen und ist 2 bis 4 mal höher als bisher angenommen. Trotzdem setzt die Eispartikelbildung bei niedriger Übersättigung ein, was sich durch ein in dieser Arbeit entwickeltes Aktivierungsmodell beschreiben lässt. Im Gegensatz dazu bilden sich CO₂-Wolken auf dem Mars nur bei sehr hoher Übersättigung. Der Bildungsprozess der CO₂-Eis Partikel lässt sich anhand klassischer Nukleationstheorie mit in dieser Arbeit bestimmten Parametern beschreiben. Die Ergebnisse dieser Arbeit verbessern entscheidend das bisher lückenhafte Verständnis des Entstehungsprozesses mesosphärischer Wolken auf der Erde und dem Mars.

List of own publications

Publications included in this work

Parts of the results presented in this dissertation have been published. The corresponding publications are listed below including author contributions. In this work, I adopted these publications and thus identical wording may occur.

- [Nachbar et al., 2016]: **Nachbar, M.**, Duft, D., Mangan, T. P. , Martin, J. C. G., Plane, J. M. C., and Leisner, T. Laboratory measurements of heterogeneous CO₂ ice nucleation on nanoparticles under conditions relevant to the Martian mesosphere. *Journal of Geophysical Research - Planets*, 121(5):753–769, 2016. doi: 10.1002/2015JE004978.

MN carried out the experiments with support of DD, TM and JM. MN performed the data analysis. MN prepared the manuscript with contributions from all co-authors. JP and TL supervised the experiments.

- [Nachbar et al., 2018a]: **Nachbar, M.**, Duft, D., and Leisner, T. The vapor pressure over nano-crystalline ice. *Atmospheric Chemistry and Physics*, 8(5):3419–3431, 2018a. doi: 10.5194/acp-18-3419-2018.

MN and DD designed the experiments. MN carried out the MICE-TRAPS experiments. MN and DD carried out the pressure gauge experiments. MN performed the data analysis. MN prepared the manuscript with contributions from all co-authors. DD and TL supervised the experiments.

- [Nachbar et al., 2018b]: **Nachbar, M.**, Duft, D., Kiselev, A., and Leisner, T. Composition, Mixing State and Water Affinity of Meteoric Smoke Analogue Nanoparticles Produced in a Non-Thermal Microwave Plasma Source. *Zeitschrift fuer Physikalische Chemie*, 2018. doi:10.1515/zpch-2017-1053.

MN carried out the experiments and performed the data analysis. MN and DD prepared the manuscript with contributions from all co-authors. AK and TL supervised the experiments.

Publications not included in this work

- [Weller et al., 2014]: Weller, R., Levin, I., Schmithuesen, D., **Nachbar, M.**, Asseng, J., and Wagenbach, D. On the variability of atmospheric Rn-222 activity concentrations measured at Neumayer, coastal Antarctica. *Atmospheric Chemistry and Physics*, 14(8): 3843–3853, 2014. doi: 10.5194/acp-14-3843-2014.
- [Duft et al., 2015]: Duft, D., **Nachbar, M.**, Eritt, M., and Leisner, T. A Linear Trap for Studying the Interaction of Nanoparticles with Supersaturated Vapors. *Aerosol Science and Technology*, 49(9):682–690, 2015. doi: 10.1080/02786826.2015.1063583.

Contents

1. Introduction	1
2. Polar mesospheric clouds on Earth	5
2.1. Climatology of PMCs	5
2.2. Condensation nuclei	9
2.3. Onset conditions for cloud formation	11
2.4. Ice phases in the terrestrial mesopause	13
2.4.1. Metastable ice phases	13
2.4.2. Review of vapor pressure measurements	14
3. Mesospheric CO₂ clouds on Mars	19
3.1. Climatology of mesospheric CO ₂ clouds	19
3.2. Condensation nuclei	21
3.3. Onset conditions for cloud formation	21
4. Microphysics of ice cloud formation	25
4.1. The Kelvin effect	25
4.2. Homogeneous nucleation	28
4.3. Heterogeneous nucleation	29
4.4. Influence of charge	34
4.5. Ice particle growth	38
5. Experimental setup	41
5.1. The MICE-TRAPS apparatus	41
5.1.1. The particle source	41
5.1.2. The TRAPS apparatus	43
5.1.3. The MICE ion trap	44
5.2. Relative vapor pressure measurements using an ionization gauge	47
6. H₂O vapor pressure measurements	51
6.1. Methods	51
6.1.1. Measurements using MICE-TRAPS	51
6.1.2. Relative measurements with an ionization gauge	57
6.2. Results	58
6.3. Discussion	61
6.3.1. Comparison to literature data	61
6.3.2. The effect of nano-crystals on the vapor pressure	62

6.3.3. The vapor pressure over nano-crystalline ice and ASW	65
6.3.4. Comparison to DSC measurements	68
6.4. Conclusions	71
7. H₂O nucleation experiments	73
7.1. Methods	73
7.2. Results	75
7.2.1. Desorption energy	75
7.2.2. Critical saturations	78
7.3. Discussion	80
7.3.1. Activation model	80
7.3.2. Charge effects	83
7.3.3. Onset conditions for PMC formation	84
7.4. Conclusions	86
8. CO₂ nucleation experiments	89
8.1. Methods	89
8.2. Results	92
8.2.1. Desorption energy	92
8.2.2. Contact parameter	93
8.3. Discussion	94
8.3.1. Desorption energy and contact parameter	94
8.3.2. Onset conditions for cloud formation	98
8.4. Conclusions	100
9. Summary	103
9.1. Polar mesospheric clouds on Earth	103
9.2. Mesospheric CO ₂ clouds on Mars	104
9.3. Outlook	104
A. Characterization of the MSP analogues	107
B. List of parameters	111
Bibliography	113

1. Introduction

"A sea of luminous silvery white cloud"

Robert C. Leslie, Nature Vol. 32 p. 245, 1885

The first reported sighting of mysteriously glowing clouds after sunset was made in 1885 by Robert C. Leslie [Leslie, 1885, 1886]. It was clear that the clouds must receive their light from the sun, even well after sunset, hinting at a high altitude. Because of their visual appearance, these clouds were termed Noctilucent Clouds (NLCs). Since 1885, many efforts were made to document and study this astonishing phenomenon, both from the Earth's surface and with space born instruments.

Today we know that these clouds appear in the polar summer mesopause of the Earth's atmosphere. The summer mesopause is located at an altitude of about 80 to 90 km and is the coldest layer in the Earth's atmosphere. Mean daily temperatures at high latitudes fall from about 190 K in winter to about 120 K in summer [Holton, 1982; Luebken et al., 2009]. Moreover, water vapor concentrations peak during summer months due to an enhanced photolytic oxidation of methane [Thomas et al., 1989; Seele and Hartogh, 1999]. These two effects combined cause highly supersaturated conditions at high latitudes, giving rise to the formation and growth of ice particles. When the ice particles reach about 30 nm in radius and their concentration is on the order of 100 cm^{-3} , they become optically visible from ground or space [e.g. Rapp and Thomas, 2006; Bardeen et al., 2010; Kiliani et al., 2015]. Because their occurrence is restricted to high latitudes, these clouds are frequently, as in this work, termed Polar Mesospheric Clouds (PMCs).

Temperature and water vapor concentration are the two crucial parameters triggering PMC formation. Since oxidation of methane is the most important water source in the mesosphere and CO_2 acts as a cooling agent [Berger and von Zahn, 1999; Akmaev and Fomichev, 1998; Roble and Dickinson, 1989], PMCs may be a tracer for long-term changes due to anthropogenic emissions of CO_2 and methane [e.g. Thomas et al., 1989; Thomas and Olivero, 2001]. Colder temperatures and higher H_2O concentrations are expected to cause more and brighter PMCs. Analyses of long-term trends in PMC properties, however, are at present contradicting. Whether or not PMCs may be utilized one day to determine long-term trends caused by anthropogenic CO_2 and CH_4 emissions is still under debate [e.g. Thomas et al., 2003; von Zahn, 2003; DeLand et al., 2007; Kirkwood et al., 2008; Pertsev et al., 2014; Hervig et al., 2016].

Recently, attempts have been made to use PMCs as a passive tracer for the dynamical structure of the summer mesopause. Satellite [e.g. Rong et al., 2015] and lidar [e.g. Kaifler et al., 2013] observations as well as ground based images [e.g. Demissie et al., 2014] have for example been used to infer wind velocities and gravity wave parameters.

When the observation of PMCs is intended to draw conclusions about long-term trends or thermal and dynamic conditions of the summer mesopause, it is necessary to understand the processes leading to PMCs in detail. One of the most critical processes is the initial ice formation. This process is called nucleation and is most likely initiated heterogeneously on recondensed meteoric material, so called Meteoric Smoke Particles (MSPs) [e.g. Hervig et al., 2012; Havnes et al., 2014; Antonsen et al., 2017]. However, many details about the ice formation process on these particles are still not well understood [e.g. Rapp and Thomas, 2006]. The deposition of different metastable ice phases is possible at the extremely cold temperatures of the summer mesopause below 150 K [e.g. Hobbs, 1974]. Besides crystalline cubic or stacking disordered ice, Amorphous Solid Water (ASW) might form [Hervig and Gordley, 2010; Murray and Jensen, 2010; Murray et al., 2015]. Material properties of these ice phases like the surface tension or the saturation vapor pressure are not well characterized, but significantly influence the nucleation process. Additionally, the contact parameter m and the desorption energy ΔF_{des} , the two key parameters in classical nucleation theory, are not well constrained for MSPs in the summer mesopause. Consequently, the onset conditions for ice particle formation in the summer mesopause are only poorly known. This is why many authors emphasize the need for laboratory experiments on the heterogeneous ice nucleation process at the extreme conditions of the summer mesopause [e.g. Rapp and Thomas, 2006; Gumbel and Megner, 2009; Megner and Gumbel, 2009]. Such experiments are presented in this work and intend answer two key questions concerning PMC formation:

- **What is the predominant ice phase involved in PMC formation?**
- **What are onset conditions for PMC formation?**

Very surprisingly, the Mars rover of the Pathfinder mission observed a cloud layer above 70 km altitude in 1997 which is very similar to PMCs on Earth [Smith et al., 1997; Clancy and Sandor, 1998]. After this discovery, these clouds have been observed many times in the Martian mesosphere [e.g. Montmessin et al., 2006, 2007; Clancy et al., 2007; Määttänen et al., 2010; Vincendon et al., 2011; Stevens et al., 2017]. They were mainly spotted at 60 to 100 km altitude at tropical to sub-tropical latitudes during pre- and post-aphelion season. In contrast to PMCs on Earth, the majority of these clouds consists of CO₂ [Vincendon et al., 2011], the main constituent (95 %) of the Martian atmosphere.

As on Earth, mesospheric CO₂ clouds on Mars are believed to form heterogeneously [Listowski et al., 2014; Määttä et al., 2010], with the nature of the CO₂-ice nuclei still under discussion. Potential candidates are Meteoric Smoke Particles (MSPs), upward propagating Martian Dust Particles (MDPs), and dirty H₂O ice particles [Listowski et al., 2014; Plane et al., 2018]. At temperatures relevant for the Martian mesosphere (70 to 120 K), CO₂ is known to be present in only one crystalline state [Souda, 2006] with a well constrained vapor pressure [e.g. Meyers and Van Dusen, 1933; Azreg-Ainou, 2005]. However, the onset conditions for CO₂ ice particle formation are only poorly known due to a lack of CO₂ nucleation experiments conducted with realistic nuclei materials for ambient conditions relevant to the mesosphere of Mars. Such experiments are presented in this work and intend to answer one key question concerning CO₂ ice cloud formation in the mesosphere of Mars:

- **What are onset conditions for CO₂ ice cloud formation?**

This thesis addresses all three questions with the help of laboratory experiments. The ice nucleation and ice growth behavior of H₂O and CO₂ on singly charged MSP analogues were investigated in the Trapped Reactive Atmospheric Particle Spectrometer (TRAPS). In TRAPS, the particles were selected by size and further stored in an ion trap called Molecular flow Ice Cell (MICE). I designed, built, and characterized MICE as part of my Master's Thesis. [Nachbar, 2014]. In MICE, the particles were subject to conditions relevant for the mesosphere of Earth and Mars in terms of temperature and supersaturation of H₂O or CO₂. The adsorption, nucleation, and subsequent growth process of H₂O or CO₂ on the MSP analogues was studied by analyzing the mass of the particles as function of the residence time in MICE with a time of flight mass spectrometer.

This dissertation is organized as follows. Chapter 2 and 3 review the current knowledge about PMCs on Earth and mesospheric clouds on Mars. Chapter 4 introduces the theoretical background to the microphysics of ice particle formation and ice growth processes. Chapter 5 introduces the experimental setup with focus on the nanoparticle production and MICE. The subsequent three chapters present the results and provide answers to the three questions formulated above. Chapter 6 presents results on saturation vapor pressure measurements of H₂O ice phases at conditions relevant to the terrestrial mesopause. Chapter 7 describes the H₂O nucleation experiments and Chapter 8 reports on CO₂ nucleation experiments. Chapter 9 summarizes all results and discusses the progress achieved by this work for the understanding of ice cloud formation in the mesosphere of Earth and Mars. This thesis is partly based on three publications which were published in peer-reviewed journals during the course of this study [Nachbar et al., 2016, 2018a,b].

2. Polar mesospheric clouds on Earth

2.1. Climatology of PMCs

Polar Mesospheric Clouds (PMCs) are an impressive optical phenomenon of ice particles formed in the summer mesopause region. These beautiful ice layers were observed from the Earth's surface as a silvery white cloud layer for the first time in 1885 [e.g. Leslie, 1885, 1886]. A picture of a typical ground based observation is shown in Figure 2.1. After sunset the ice particles are still illuminated by the sun due to their high

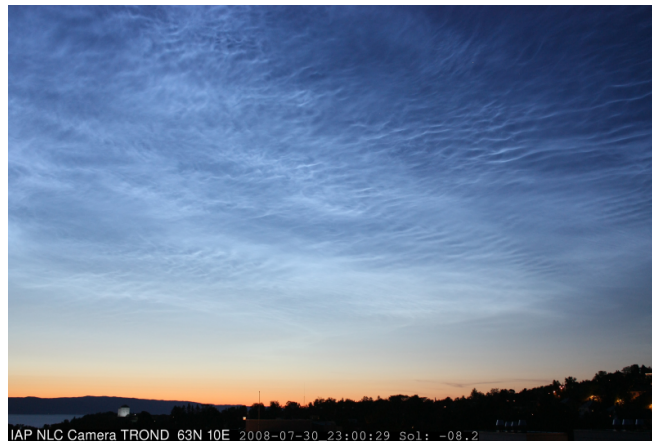


Figure 2.1.: PMCs as seen from Trondheim (30.07.2008 - 23:00 UT). Figure from Demissie et al. [2014].

altitude (≈ 82 km) so that they scatter light to the Earth's surface. The wave like pattern of the clouds is caused by gravity waves which pass through or break at the mesopause. Based on their visual appearance when observed from the Earth's surface, they are often referred to as Noctilucent Clouds (NLCs). Since 1885 many efforts were made to document and study these clouds either from the Earth's surface or with space-borne instruments [e.g. Thomas and Olivero, 2001; Thomas et al., 2003; von Zahn, 2003; DeLand et al., 2007; Kirkwood et al., 2008; Demissie et al., 2014; Pertsev et al., 2014; Kaifler et al., 2013; Rong et al., 2015; Hervig et al., 2016]. The clouds are observed at high latitudes (above about 50° N/S) about every third night from mid May till end of August [e.g. Thomas, 1991; Kirkwood et al., 2008].

PMCs are a phenomenon related to the extreme thermal conditions of the summer mesopause, the coldest layer of the Earth's atmosphere. It defines the boundary between the mesosphere, where the temperature decreases with altitude, and the thermosphere, where the temperature increases with altitude. The height of the mesopause depends on season and latitude and varies between 80 and 100 km. Especially during summer gravity waves produced in the troposphere may propagate through the mesosphere and tend to break at about 90 km altitude [Berger and von Zahn, 1999; Berger, 2008]. This effect increases with latitude and leads to a cooling effect during summer at mid to high latitudes [Holton, 1982]. Figure 2.2 is an illustration of the seasonal temperature variation of the mesopause observed with a potassium lidar system ($\lambda = 769.9$ nm) between 2001 and 2003 over Spitzbergen (78°N) [Luebken et al., 2009]. Here, mean summer temperatures fall below 120 K and are about 70 K colder

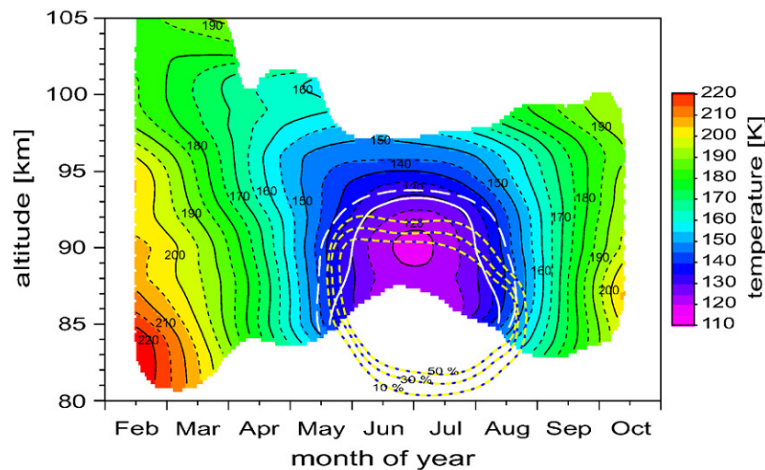


Figure 2.2.: Seasonal variation of daily mean temperatures at the mesopause region over Spitzbergen (78°N) between 2001 and 2003. Within the areas enclosed by the white solid and dashed lines supersaturation with respect to hexagonal ice I_h is present according to two different water vapor profiles. The dashed yellow lines indicate events of Polar Mesospheric Summer Echoes. Reprinted from Luebken et al. [2009], with permission from Elsevier.

than during winter. The coldest point during summer is located at about 90 km altitude.

Beside the H_2O transported from the lower atmosphere to the mesosphere, photochemical oxidation of methane is the main source of H_2O molecules in the summer mesopause. In the lower mesosphere, oxygen radicals from the photolytic destruction of ozone oxidate methane resulting in the production of approximately two H_2O molecules per methane molecule [Le Texier et al., 1988; Thomas et al., 1989]. The photolytic destruction of ozone heats the lower mesosphere. This heating effect, combined with the cooling of the upper mesosphere, gives rise to a super-adiabatic temperature gradient introducing upward motion [Korner and Sonnemann, 2001]. This leads to an

upward transport of water molecules resulting in H_2O concentrations of a few parts per million in the mesopause region [Seele and Hartogh, 1999]. The combination of low temperature and increased water vapor concentration during summer results in supersaturated conditions as indicated by the white lines in Figure 2.2. The saturation ratio S is defined as the ratio of H_2O vapor pressure to H_2O saturation vapor pressure. Saturations in excess of $S=1$ represent supersaturated conditions. In 40 % to 50 % of all cases with supersaturated conditions, saturation ratios exceeded 100 and in 10 % to 20 % even 10 000 [Luebken et al., 2009]. Such high supersaturations give rise to the formation of ice particles which may be observed as PMCs. Note that supersaturated conditions are present from mid May till August which coincides with the occurrence season of PMCs [e.g. Thomas, 1991; Kirkwood et al., 2008].

The general picture of the formation process of PMCs is depicted in the left panel of Figure 2.3 [Rapp and Thomas, 2006]. During summer supersaturated conditions

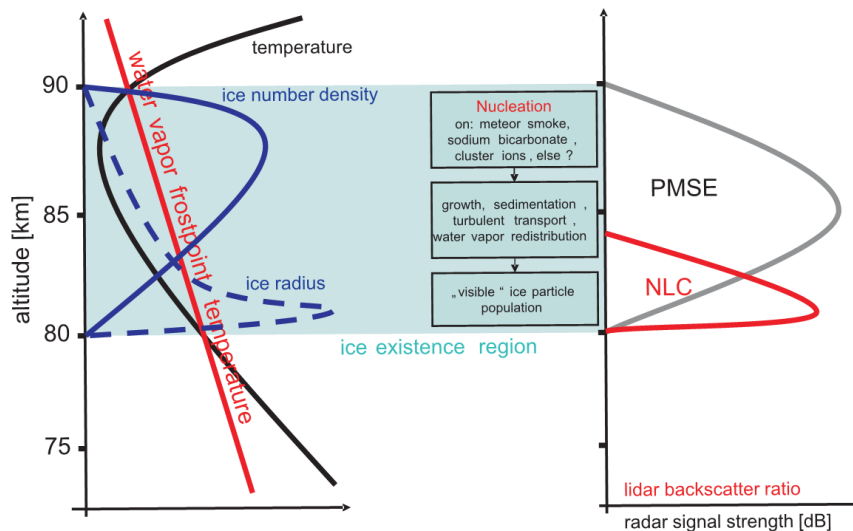


Figure 2.3.: Left panel: Schematic representation of the life cycle of mesospheric ice particles. Right panel: Ice particles visible as NLCs or PMCs are only present at the lower boundary of the supersaturated conditions. The whole ice layer, however, influences the ambient plasma giving rise to Polar Mesospheric Summer Echoes (PMSE). Reprinted from Rapp and Thomas [2006], with permission from Elsevier.

are present between about 80 and 90 km of height. Ice particle formation activates at the altitude with the highest supersaturation, which is close to the altitude of coldest temperature (typically between 86 km and 90 km). After formation the ice particles sediment to lower altitudes. They grow due to supersaturated conditions with the residence time being influenced by the mean vertical wind and turbulent transport. When ice particles reach about 30 nm in radius and concentrations are on the order of 100 cm^{-3} , they become optically visible and can be seen from ground or with space

born instruments as PMCs. This is typically the case at about 82 km altitude (see right panel of Figure 2.3). However, even smaller ice particles can be detected from ground in the presence of turbulent conditions. Ice particles pick up electrons and therefore can deplete the free electron density in the mesopause. Variations in the free electron density at dimensions of a few meter cause a backscattering signal of radar measurements in the very high frequency wavelength regime. This phenomenon is called Polar Mesospheric Summer Echoes (PMSEs), which are caused when ice particles are present in combination with neutral air turbulence [Rapp and Lubken, 2004]. In most of the summer time observations, PMSEs have been observed as indicated by the dashed yellow lines in Figure 2.2.

This view of the general climatology of PMCs is broadly accepted, but many important details are still unknown and complicate the interpretation of PMC observations. The highest uncertainty appears to be the initial ice formation process [e.g. Rapp and Thomas, 2006]. This process is called nucleation. Homogeneous nucleation describes the process of forming an ice particle out of the gas phase which is large enough to be stable in the surrounding environment and thus is able to grow. Heterogeneous nucleation describes the ice formation process if a preexisting particle, a so called nucleus, is involved. The nucleus reduces the activation barrier for ice cluster formation. This reduction of the activation barrier increases the probability of ice particle formation. Several different nucleation mechanisms have been proposed in the mesopause region. Besides homogeneous nucleation [Murray and Jensen, 2010], nucleation on strongly polar molecules [Plane, 2000] and heterogeneous nucleation on so called Meteoric Smoke Particles (MSPs) [Turco et al., 1982] have been proposed. The latter is regarded to be the most important nucleation mechanism [e.g. Rapp and Thomas, 2006], especially when MSPs are electrically charged [Gumbel and Megner, 2009; Megner and Gumbel, 2009]. MSPs are introduced in detail in Chapter 2.2. In brief, they are nanometer sized particles composed of re-condensed ablated meteoric material.

However, many details of heterogeneous nucleation on MSPs remain unclear. First, the exact composition of MSPs is still under discussion. Second, the parameters which in nucleation theory describe the ice formation process are unknown for potential MSP compositions at conditions of the mesopause. This is mainly because no nucleation experiments on realistic MSP analogues at mesopause conditions existed so far. Additionally, deposition of different metastable ice phases is possible at temperatures below 150 K typically occurring in the summer mesopause [e.g. Hobbs, 1974]. Besides the crystalline cubic or stacking disordered ice, Amorphous Solid Water (ASW) might form [Hervig and Gordley, 2010; Murray and Jensen, 2010; Murray et al., 2015]. Material properties like the surface tension or the saturation vapor pressure of these ice phases are not well characterized, but significantly alter the nucleation process.

The next sections introduce MSPs, discuss the current status of uncertainties in predicting onset conditions for PMC formation and introduce the different ice phases which might form under conditions of the summer mesopause.

2.2. Condensation nuclei

Meteoric Smoke Particles (MSPs) are believed to be the major type of nuclei which is available for the formation process of PMCs [e.g. Rapp and Thomas, 2006; Gumbel and Megner, 2009; Megner and Gumbel, 2009]. MSPs are nanometer sized particles which are composed of re-condensed ablated meteoric material. Between 5 and 270 tons of cosmic dust are entering the atmosphere of Earth each day [Plane, 2012]. Recent best estimates point to an average particle precipitation rate of about 40 tons per day [Carrillo-Sanchez et al., 2016]. Here, the greatest proportion are micrometer size cosmic dust particles. They enter the atmosphere and ablate in the upper mesosphere and lower thermosphere via sputtering (ejection of surface atoms due to collision with air molecules) and evaporation of mostly volatile atoms after melting of the meteoric particle [Vondrak et al., 2008]. In the Earth atmosphere only about 20 % of the cosmic dust material ablates [Carrillo-Sanchez et al., 2015, 2016]. The cosmic dust particles ablate mostly between 80 and 90 km altitude with the major elemental components being Fe, Si and Mg [Vondrak et al., 2008]. The ablated atoms react with O₃, O₂, CO₂ and H₂O forming oxides, hydroxides and carbonates, which re-condense to so called Meteoric Smoke Particles (MSPs) [Plane et al., 2015].

The minimum radius of a particle which could potentially serve as nucleus for ice formation is believed to be about 1.1 nm for typical conditions in the summer mesopause [e.g. Rapp and Thomas, 2006; Megner and Gumbel, 2009; Asmus et al., 2014]. Hence, if MSPs actually are the major type of condensation nuclei for PMCs, the concentration of MSPs above that critical size needs to be sufficient to explain PMC ice particle concentrations. Typical ice particle concentrations are in the order of 100 cm⁻³ [Bardeen et al., 2010; Kiliani et al., 2015]. First attempts to characterize the size distribution and concentration of MSPs in the mesopause were made in a 1D-atmospheric model [Hunten et al., 1980]. The model shows concentrations of a few thousand per cm³ with radii larger than 1 nm. However, more sophisticated 2D- [Megner et al., 2008a,b] and 3D-models [Bardeen et al., 2008] show that a meridional circulation in the mesopause introduces an effective transport of MSPs from the summer to the winter pole. As a result, the MSP concentration is significantly reduced during summer. The MSP concentration for particle radii above 1 and 0.5 nm as well as the total MSP concentration simulated with the 2D-model of Megner et al. [2008b] for 68°N on July 10th is shown in Figure 2.4. These profiles question the relevance of MSPs as nuclei for the formation of ice particles in the mesopause. Particles with radii well below 1 nm must activate ice growth in order to form clouds with ice particle concentrations of 100 cm⁻³. However, modeled profiles as shown in Figure 2.4 are still subject to large uncertainties since model parameters describing the coagulation rate of MSPs, the Eddy Diffusion and the amount of meteoric input are not well constrained.

The variation of the MSP concentration between summer and winter was qualitatively confirmed with solar occultation measurements [Hervig et al., 2009]. In addition, several rocket-born measurements using different kinds of particle detectors were used to

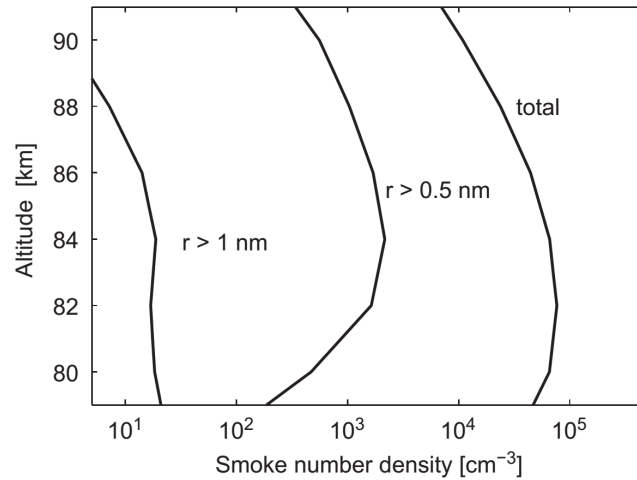


Figure 2.4.: MSP size distribution in the mesopause at 68°N on July 10th as modeled by Megner et al. [2008b]. Reprinted from Gumbel and Megner [2009], with permission from Elsevier.

constrain the MSP size and concentration profiles predicted by models [e.g. Asmus et al., 2017; Robertson et al., 2014; Plane et al., 2014; Rapp et al., 2012]. Such measurements are rare and only display a snap-shot of the mesosphere and thermosphere. The rockets are typically launched in absence of ice particles (mostly during winter) and the detectors are only able to measure the charged particle number and size distribution. All studies have in common that in the altitude range of 80 to 90 km all charged particles carry a negative charge and size distributions qualitatively match the model results i.e. the majority of the detected particles are smaller than 1 nm in radius. However, in order to evaluate these measurements for the total MSP concentration profile, the percentage of negatively charged particles needs to be known. Model results estimate the percentage of negatively charged particles to about 10% at PMC height and season [Plane et al., 2014, 2015].

The presumption of particles with radii larger than 1.1 nm giving rise to ice particle formation is unfounded. Gravity waves initiate large temperature variations on the order of 10 K [Rapp et al., 2002]. These temperature variations cause high supersaturations for a short time period which allow ice formation on particles smaller than 1 nm. In addition, Gumbel and Megner proposed that the charged population below 1 nm may form ice particles at typical summer mesopause conditions due to the influence of charge-dipole interactions on the nucleation process [Gumbel and Megner, 2009; Megner and Gumbel, 2009].

Recent satellite and rocket-borne observations support the importance of MSPs as ice nuclei in the summer mesopause. Hervig et al. [2012] used solar occultation mea-

measurements to study PMC extinction profiles at 4 different wavelengths from the ultraviolet to the infrared. The measured extinction profiles are not conform with those expected for pure ice particles but need MSP material with 0.01 vol. % to 3 vol. % included in the ice matrix. The extinction profiles are consistent with wüstite (FeO) or magnesio-wüstite ($\text{Mg}_x\text{Fe}_{1-x}\text{O}$, $x=0.1-0.6$) rather than metal-silicates. This finding is in agreement with measurements of the work function of MSPs during a rocket campaign within the ECOMA project in 2010 [Rapp et al., 2012]. In addition, analysis of collision fragments of PMC ice particles with the MUDD detector recently proved the existence of meteoric material in PMC ice particles [Havnes et al., 2014; Antonsen et al., 2017]. An estimation of the size distribution of the MSPs included in the ice particles agrees with modeled MSP size distributions.

2.3. Onset conditions for cloud formation

Although PMC formation is very likely initiated via heterogeneous nucleation on MSPs, the highest uncertainty in interpreting PMC observations appears to be the formation process of the clouds [e.g. Rapp and Thomas, 2006]. Two different approaches are used by the PMC science community to predict onset conditions for PMC formation. (1) Ice particle formation activates as soon as the saturation exceeds the Kelvin effect [e.g. Berger and Luebken, 2015; Schmidt et al., 2017], or (2) ice particle formation is described using the surface diffusion approach of Classical Nucleation Theory (CNT) [e.g. Rapp and Thomas, 2006; Bardeen et al., 2010; Asmus et al., 2014]. The two approaches are introduced in detail in Chapter 4. In brief, the Kelvin effect describes the equilibrium saturation over an ice particle, which is elevated for small particles. Using these calculations it is assumed that MSPs are perfect ice nuclei. CNT on the other hand assumes that H_2O molecules adsorb on the surface of the nucleus and collide with other molecules via surface diffusion to form clusters. These clusters might eventually get large enough to be stable and activate depositional ice growth. Such a process is called nucleation, which is mainly described by two parameters: (1) the desorption energy ΔF_{des} and (2) the contact parameter m . The nucleation rate per particle depends on the saturation. The saturation at which nucleation occurs is called critical saturation S_{cr} .

Figure 2.5 shows critical saturations with respect to hexagonal ice $S_{\text{cr,h}}$ as a function of particle radius at a typical summer mesopause temperature of 120 K. The blue line shows the results of Kelvin effect calculations. The red shaded area represents $S_{\text{cr,h}}$ calculations using CNT with the current consensus of material parameters for MSPs ($\Delta F_{\text{des}} = 2.9 \times 10^{-20}$ J/molec and $m = 0.6 - 0.95$). The black dashed horizontal line indicates a typical mesopause H_2O concentration of $2 \times 10^{14} \text{ m}^{-3}$ (2 ppm at about 87 km altitude). The difference in critical saturations between CNT and Kelvin effect calculations illustrates the large discrepancies of current models in predicting conditions at which ice particles form. According to Kelvin effect calculations, particles with radii larger than about 0.7 nm serve as ice nuclei at 120 K and a typical water vapor

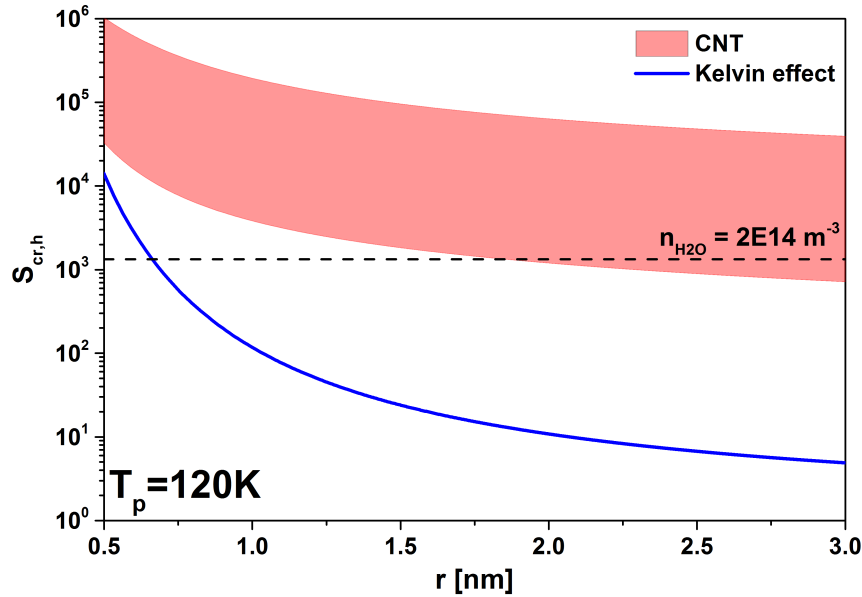


Figure 2.5.: Critical saturations $S_{cr,h}$ as a function of particle size at 120 K particle temperature. Shown are Kelvin effect calculations (blue line) and CNT calculations using typically assumed parameters (red shaded area). The horizontal dashed line represents a typical mesopause H_2O concentration of $2 \times 10^{14} m^{-3}$.

concentration. The concentration of MSPs larger than this critical radius is expected to be on the order of $100 cm^{-3}$ [Megner et al., 2008a; Gumbel and Megner, 2009]. Hence, Kelvin effect calculations are able to explain typical ice particle concentrations of PMCs, which are on the order of $100 cm^{-3}$ [e.g. Bardeen et al., 2010; Kiliani et al., 2015]. CNT calculations on the contrary predict ice particle formation on particles with radii larger than 2 nm. The concentration of particles with radii larger than 2 nm is expected to be below $10 cm^{-3}$ and thus the CNT calculations can not explain the formation of PMCs.

The calculations of critical saturations assume deposition of hexagonal ice I_h . A potential formation of metastable ice phases increases uncertainties in predicting critical saturations. Ice phases which might be present in the summer mesopause are introduced in the next section. Furthermore, charge effects are expected to cause a decrease of critical saturations for the charged MSP population [Gumbel and Megner, 2009; Megner and Gumbel, 2009].

The description of the ice particle formation process strongly influences model results on PMC properties [Wilms et al., 2016]. Hence, whenever the observation of PMCs shall be used to draw conclusions about long-term trends or thermal and dynamical conditions of the summer mesopause, the ice particle formation process needs to be understood in detail. To this end, the tremendously large uncertainties in predicting

conditions at which ice particles form in the mesopause of Earth need to be reduced. In order to overcome these uncertainties nucleation experiments on realistic MSP materials and particle sizes as well as for realistic mesopause conditions are strongly needed. Such experiments were undertaken within the framework of the present thesis. They are presented and discussed in Chapter 7. Figure 2.5 serves as a reference case for comparison to the experimental results.

2.4. Ice phases in the terrestrial mesopause

In order to predict the H_2O vapor pressure and thus the critical saturation at which ice formation is initiated in the summer mesopause, knowledge of the ice phase and its saturation vapor pressure are of great importance. At temperatures relevant for cloud formation processes in the terrestrial mesopause ($T < 150 \text{ K}$), solid water (ice) may be encountered in several metastable forms [e.g. Hobbs, 1974]. Although these water ice polymorphs are of interest for many atmospheric processes as well as for interstellar ices, their saturation vapor pressures are not well known. The following briefly reviews the current knowledge on the different ice phases of interest at conditions relevant to the terrestrial mesopause.

2.4.1. Metastable ice phases

Hexagonal ice I_h is the lowest energy phase and thus the most stable phase of solid water below the freezing point under typical terrestrial atmospheric conditions. However, at temperatures relevant for cloud formation processes in the mesopause of Earth ($T < 150 \text{ K}$) water may form several metastable solids. At atmospheric pressures and temperatures below about 130 K , Amorphous Solid Water (ASW) is expected to form via deposition from the vapor phase [e.g. Hobbs, 1974]. It has been proposed that ASW is the low temperature form of supercooled water, but this assumption is currently still under discussion [e.g. Speedy, 1992; Johari et al., 1994; Murphy and Koop, 2005]. Over time, upon warming of ASW or by direct deposition between about 130 and 200 K , cubic ice I_c may form [e.g. Hobbs, 1974; Keyser and Leu, 1993]. Recently, studies using diffraction measurements and numerical simulations suggested that rather than pure cubic ice, crystalline sequences of cubic ice interlaced with sequences of hexagonal ice form [e.g. Shallcross and Carpenter, 1957; Kuhs et al., 2012; Thuermer and Nie, 2013; Malkin et al., 2015; Murray et al., 2015; Hudait et al., 2016; Lupi et al., 2017]. This ice polymorph has been called stacking disordered ice I_{sd} . Cubic ice I_c and hexagonal ice I_h are both based on stacked layers of water molecules in sixfold symmetry, differing only in the stacking sequence of these layers. Hence, most physical properties of cubic and hexagonal ice are similar [Kuhs et al., 2012]. Consequently, the vapor pressure of ice I_{sd} is expected to be only slightly higher compared to ice I_h .

In general, a metastable ice polymorph features a Gibbs free energy difference $\Delta G_{m \rightarrow h}(T)$ with respect to the stable hexagonal ice I_h . $\Delta G_{m \rightarrow h}(T)$ can be separated into an enthalpy $\Delta H_{m \rightarrow h}(T)$ and an entropy $\Delta S_{m \rightarrow h}(T)$ contribution according to

$$\Delta G_{m \rightarrow h}(T) = \Delta H_{m \rightarrow h}(T) - T \Delta S_{m \rightarrow h}(T). \quad (2.4.1)$$

The vapor pressure p_{sat}^m of a metastable ice form is increased with respect to ice I_h which is described by

$$\frac{p_{\text{sat}}^m}{p_{\text{sat}}^h} = \exp\left(\frac{\Delta G_{m \rightarrow h}(T)}{RT}\right), \quad (2.4.2)$$

with the temperature T and the ideal gas constant R .

The transformation of ice I_{sd} to ice I_h has been studied extensively with Differential Scanning Calorimetry (DSC) measurements above 180 K [e.g. [Mc Millan and Los, 1965](#); [Sugisaki et al., 1968](#); [Handa et al., 1986](#); [Mayer and Hallbrucker, 1987](#)]. These studies determined the enthalpy difference $\Delta H_{sd \rightarrow h}$ between the two ice phases to be in the range of 20 Jmol⁻¹ to 180 Jmol⁻¹. Under the assumption that $\Delta S_{sd \rightarrow h}$ is close to 0 for all temperatures [[Tanaka, 1998](#); [Tanaka and Okabe, 1996](#)], $\Delta G_{sd \rightarrow h}$ equals $\Delta H_{sd \rightarrow h}$. According to Equation 2.4.2, this corresponds to a vapor pressure difference of 1 to 18 % between ice I_{sd} and ice I_h in the temperature range of 130 to 190 K. This model for ice I_{sd} is supported by measurements from [Shilling et al. \[2006\]](#). In their study they deposited hexagonal ice at 210 K from the vapor phase and measured the saturation pressure between 180 and 190 K with a MKS Baratron capacitance manometer. In addition, they deposited ASW at 90 K, heated the sample up which was accompanied with the transformation to ice I_{sd} and measured its vapor pressure at the same temperatures. The vapor pressure of their metastable crystalline sample turned out to be elevated by 10 % with respect to their ice I_h sample.

2.4.2. Review of vapor pressure measurements

Comparing vapor pressure data of metastable water ice samples is difficult at conditions relevant for the terrestrial mesopause. At these temperatures, the metastable ices transform over time to the more stable polymorph. The ice sample under investigation might therefore partly be composed of different ice phases. In order to compare data on vapor pressures obtained from different groups, the exact phase of the ice sample needs to be known. In addition, measurements of the saturation vapor pressure down to pressures of 10⁻⁸ Pa (130 K) are experimentally very challenging. However, a limited number of desorption rate measurements employing quadrupole mass spectrometers and quartz crystal microbalances are available. Under the well supported assumption that the sticking coefficient for water molecules on water ice is 1 at these temperatures [[Brown et al., 1996](#); [Batista et al., 2005](#); [Gibson et al., 2011](#); [Kong et al., 2014](#)], measured desorption rates can be used to infer saturation vapor pressures from the following equation:

$$p_{\text{sat}}(T) = \frac{4kTj_T}{v_{th,T}}. \quad (2.4.3)$$

Here, $v_{th,T}$ is the mean thermal velocity of water molecules in the vapor phase at sample temperature T , k is the Boltzmann constant and j_T is the measured desorption rate in $[\text{molec m}^{-2} \text{s}^{-1}]$.

A great number of parameterizations for the saturation vapor pressure of the stable hexagonal ice I_h have been developed which agree well with existing experimental data down to temperatures of 170 K [e.g. Jansco et al., 1970; Marti and Mauersberger, 1993; Wagner, 1994; Mauersberger and Krankowsky, 2003; Wagner et al., 2011; Fericola et al., 2012; Bielska et al., 2013]. Below 170 K, theoretical thermodynamic approaches using measurements of thermodynamic equilibrium properties like the molar heat capacity have been used to describe the vapor pressure [Feistel and Wagner, 2006, 2007; Murphy and Koop, 2005]. A very simple expression for the vapor pressure over ice I_h , which is expected to be accurate within 1% down to 110 K, was proposed by Murphy and Koop [2005]. This parameterization is frequently used in the atmospheric science community and is given by

$$p_{\text{sat}}^h = \exp \left(9.550426 - \frac{5723.265}{T} + 3.53068 \ln T - 0.00728332 \cdot T \right) [\text{Pa}] . \quad (2.4.4)$$

The upper panel of Figure 2.6 shows the vapor pressure of ice I_h between 130 and 175 K using Equation 2.4.4. The lower panel shows reported sublimation rate measurements below 175 K for metastable crystalline ice (red data points and curves) and ASW (blue data points and curves) normalized to the hexagonal ice phase. The parameterization for ice I_{sd} represented by a Gibbs free energy difference $\Delta G_{\text{sd} \rightarrow \text{h}}$ of 20 Jmol^{-1} to 180 Jmol^{-1} using Equation 2.4.2 is shown by the red shaded area.

Sack and Baragiola [1993] deposited ASW between 30 and 120 K on a quartz crystal microbalance and investigated the desorption rate during the transformation from ASW to crystalline ice as well as the desorption rate of crystalline ice after complete crystallization at constant temperature. They carefully avoided contributions of water molecules from external sources by shielding the ice sample with cold surfaces held at 12 K. They state uncertainties of the measured desorption rates but do not mention uncertainties in temperature measurements. Sublimation rates of their ASW samples were dependent on the substrate thickness and deposition temperature. The sublimation rate of the crystalline ice after complete crystallization of the ASW sample, however, was independent on the growth conditions of the sample. Thus, the same crystalline ice polymorph forms independent on the ASW deposition procedure. I digitized and converted their data representing ice crystallized from ASW (Figure 2 in Sack and Baragiola [1993]) to vapor pressures normalized to ice I_h with a temperature uncertainty of 0.6 K. The results are reproduced as red squares. The data is significantly higher compared to both, ice I_h and the parameterization for ice I_{sd} .

Brown et al. [1996] deposited crystalline ice below 150 K and measured the temperature dependent desorption rate with a quadrupole mass spectrometer between 140 and 160 K during temperature ramping experiments. Figure 2.6 shows their parameterized data as relative vapor pressures by the red solid line. Speedy et al. [1996] used the same experiment to measure the desorption rate of ASW deposited at 85 K and parameter-

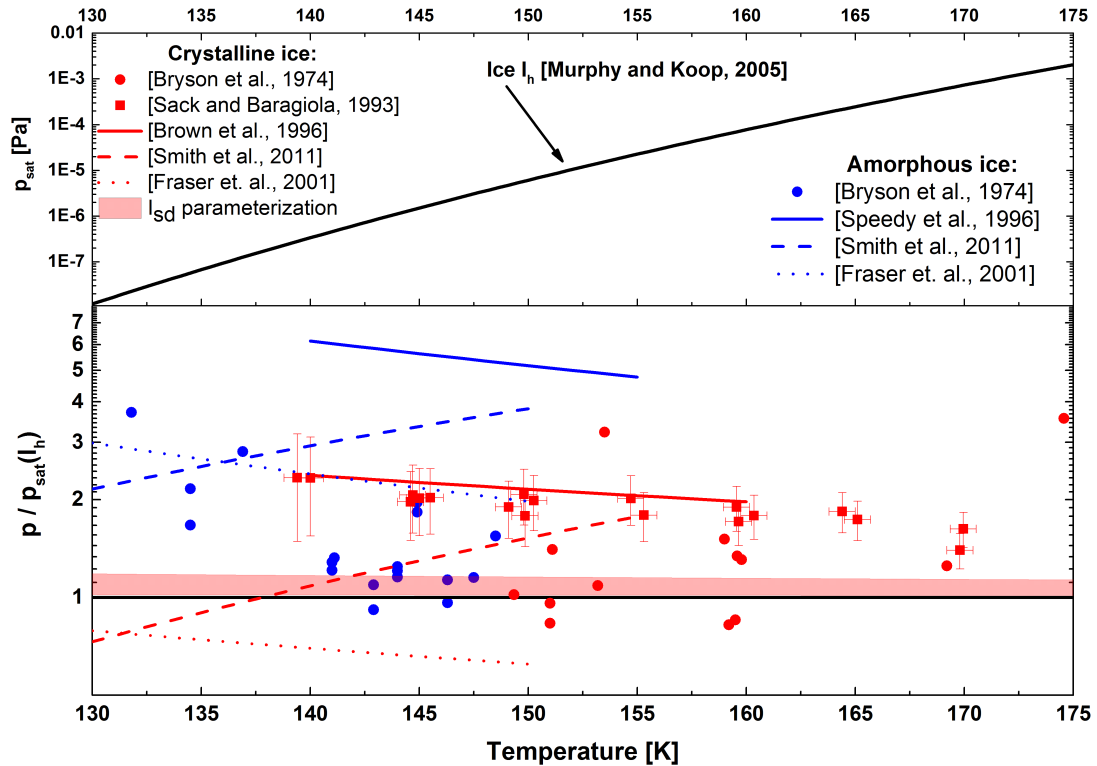


Figure 2.6.: H₂O vapor pressure measurements between 130 and 175 K. The upper panel shows the vapor pressure of hexagonal ice I_h as parameterized by [Murphy and Koop \[2005\]](#). The lower panel shows vapor pressure measurements for metastable crystalline ice (red data points and curves) and ASW (blue data points and curves) normalized to the hexagonal ice phase.

ized the desorption rate between 140 and 155 K. The parameterization is shown by the blue curve. After crystallization at about 155 K, desorption rates were identical to the measurements of [Brown et al. \[1996\]](#). The uncertainty of their parameterization covers a factor of about 2.5 and they argue to have an absolute temperature uncertainty of 2 K, which increases the uncertainty of the vapor pressure to a factor of about 5. However, the authors argue that the measured relative desorption rate difference and thus vapor pressure ratio between ASW and their crystalline ice sample is accurate. When comparing their parameterization for crystalline ice to the high precision data of [Sack and Baragiola \[1993\]](#), it is concluded that the mean value of their parameterization of the vapor pressure can be considered reliable within the 35 % uncertainty evaluated for the latter. The same group increased the sensitivity of the quadrupole mass spectrometer by moving it closer to the sample surface and extended the measurements down to 130 K [[Smith et al., 2011](#)]. The results for crystalline ice and ASW are reproduced by the red dashed and blue dashed curves. The data indicates an increasing normalized

vapor pressure with increasing temperature which is thermodynamically impossible. In addition, the desorption rates below 155 K are significantly lower compared to their previous results. The updated arrangements in support of lower temperature measurements apparently degraded the absolute accuracy of the experiments. This highlights the challenging task of absolute vapor pressure measurements at temperature below 160 K. However, the relative difference between ASW and the crystalline ice of both studies are in agreement.

Bryson et al. [1974] deposited ASW at 100 K and measured the desorption rate with a quartz crystal microbalance. They present two data sets. One below 150 K (blue dots) and one above 150 K (red dots). They assign the data below 150 K to ASW and above 150 K to crystalline ice. However, no significant difference in the vapor pressure between both data sets is apparent. They do not describe the annealing procedure post ice deposition. Therefore, it is difficult to evaluate whether their ice sample below 150 K might already be crystallized. Although they believe their data to be accurate within 3%, the normalized vapor pressures scatter (independent of temperature) within a factor of 4. This again highlights the challenging task of absolute vapor pressure measurements in that temperature range.

Fraser et al. [2001] deposited thin ASW samples (<100 layers) at 10 K. They measured the sublimation rate of ASW and crystalline ice up to 150 K utilizing a QMS. Their parameterization for ASW and crystalline ice is shown as normalized vapor pressure by the blue and red dotted curves, respectively. Their parameterization for metastable crystalline ice is significantly lower compared to the stable ice I_h , which contradicts that ice I_h is the most stable form of ice. The lower sublimation rates might be caused by an influence of the substrate material for low coverages. However, they found no evidence for the sublimation rate depending on the sample thickness. Hence, it is likely that their data for crystalline and amorphous ice is contaminated with a temperature dependent systematic offset to lower values.

Figure 2.6 and the discussion above indicates that the saturation vapor pressure of ice phases which form at conditions of the mesopause are not well constrained. Measurements of metastable ice samples below about 170 K are a very challenging task and difficult to compare. The discrepancies in the results for ASW samples from different studies may be explained by partly crystallized ASW samples. Another explanation is the high measurement uncertainties up to a factor of 5 covering the whole range of reported data. For the crystalline data, Sack and Baragiola [1993] measured sublimation rates of ice crystallized from ASW with a precision high enough to see a significantly elevated vapor pressure with respect to the parameterization for ice I_{sd} . In addition, they end up with the same crystalline ice sample independent of the deposition conditions of their ASW sample. Because of that, their data is considered reliable for ice crystallized from ASW. Furthermore, it is concluded that only one ice polymorph forms during crystallization below about 170 K. Since the vapor pressure parameterization of Brown et al. [1996] for ice crystallized from ASW agrees well with the results of Sack and Baragiola [1993], their data for crystalline and amorphous ice is assumed

to be reliable, as well.

To sum up, it can be concluded that using the saturation vapor pressure of hexagonal ice I_h to describe PMC formation might be inaccurate. Vapor pressure measurements of samples attributed to ASW and crystalline ice deviate significantly from the vapor pressure of ice I_h . In order to get a more conclusive picture about the vapor phase which gets deposited during PMC formation and its saturation vapor pressure, additional high precision measurements at mesopause conditions are strongly needed. Such measurements were undertaken in the course of this study. They are presented and discussed in Chapter 6.

3. Mesospheric CO₂ clouds on Mars

3.1. Climatology of mesospheric CO₂ clouds

Mars is the fourth planet from the sun and exhibits very harsh conditions. Surface pressures are only about 7 mbar with mean temperatures of about 210 K. The atmosphere consists mainly of CO₂ ($\approx 95\%$), N₂ ($\approx 3\%$) and Ar ($\approx 2\%$). Due to the small share of O₂ ($\approx 0.1\%$), no stratosphere has evolved in the Martian atmosphere and temperatures decrease with altitude up to the beginning of the thermosphere at about 120 km. The mesosphere is located between about 50 km and 120 km altitude.

Very surprisingly, the Mars rover of the Pathfinder mission observed a cloud layer very similar to PMCs about one hour prior to sunrise in 1997 [Smith et al., 1997]. An image of these clouds, which the Mars rover recorded, is shown in the right insert in Figure 3.1. The blue shimmering indicates small particles and the altitude has been

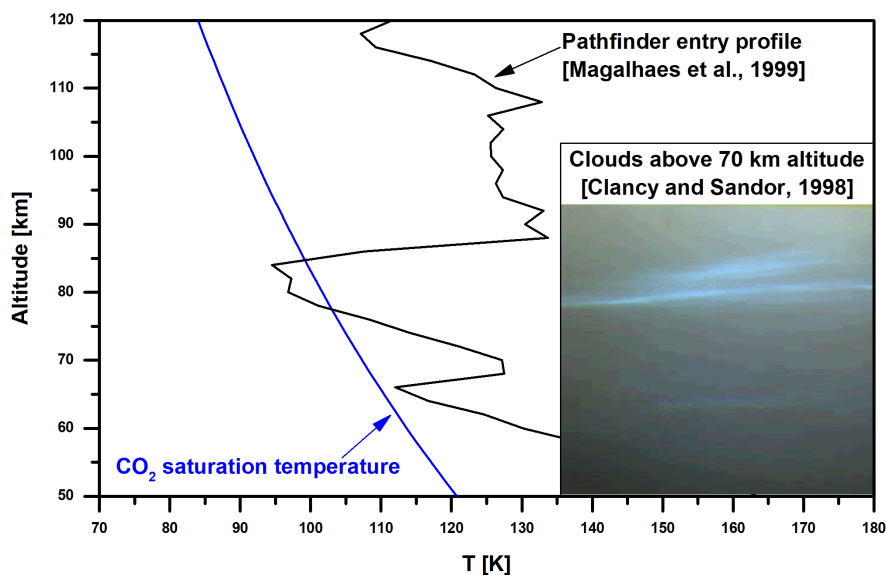


Figure 3.1.: Temperature profile recorded by Pathfinder during its descent through the Martian mesosphere (black curve) [Magalhaes et al., 1999]. For comparison, the saturation temperature of CO₂ is shown (blue curve) indicating supersaturated conditions at about 80 km of height. At about the same height, a mesospheric cloud was observed by the Mars rover of Pathfinder, which is shown in the lower right insert [Clancy and Sandor, 1998].

estimated to be above 70 km [Clancy and Sandor, 1998]. Figure 3.1 shows the temperature profile measured by Pathfinder during its descent through the Martian mesosphere (black curve). The strong temperature fluctuations are caused by thermal tides and gravity waves. At about 80 km altitude, temperatures fall below the CO₂ saturation temperature (blue curve). Therefore, these clouds have been suspected to consist of CO₂ [Clancy and Sandor, 1998]. The first conclusive proof of the Martian mesospheric clouds consisting of CO₂ was provided by the imaging spectrometer OMEGA on board of Mars Express [Montmessin et al., 2007].

After the Pathfinder discovery, CO₂ ice clouds have been observed in the Martian mesosphere ever since [e.g. Montmessin et al., 2006, 2007; Clancy et al., 2007; Määttänen et al., 2010; Vincendon et al., 2011; Stevens et al., 2017]. The clouds were mainly spotted during pre- and post-aphelion season (solar longitude $L_s \approx 0^\circ$ - 150°) which feature the coldest temperatures in the mesosphere. The clouds have been observed either during day time at tropical latitudes at altitudes between 60 km and 85 km [Montmessin et al., 2007], or at night at subtropical latitudes at altitudes between 80 km and 100 km [Montmessin et al., 2006]. Ice particle radii during day exceed 1 μm and are about one order of magnitude larger than at night [Montmessin et al., 2006, 2007].

CO₂ clouds are the dominant type of clouds in the mesosphere of Mars, but also H₂O clouds have been spotted [Vincendon et al., 2011]. This is in agreement with H₂O vapor pressure measurements showing supersaturated conditions in the mesosphere during southern spring [Maltagliati et al., 2013]. However, almost no CO₂ ice clouds have been observed during that time of the year. Additionally, no supersaturated H₂O concentrations were detected above 50 km altitude during the season of CO₂ cloud occurrence.

In the last decade great progress has been made in modeling mesospheric CO₂ clouds and the general climatology of cloud formation is widely accepted. At tropical latitudes, thermal tides and gravity waves are comparably strong [Creasey et al., 2006]. They propagate through the mesosphere and cause cold pockets with temperatures well below the CO₂ frost point temperature thereby inducing the formation of CO₂ clouds [Gonzalez-Galindo et al., 2011; Spiga et al., 2012; Listowski et al., 2014]. However, as on Earth, the initial ice particle formation process is still highly uncertain and different processes have been discussed in the literature. These processes are (1) homogeneous nucleation, (2) ion-induced nucleation, and (3) heterogeneous nucleation. Homogeneous nucleation of CO₂ in the mesosphere would require temperatures about 50 K below frost point temperature [Määttänen et al., 2010], which have not been observed. Furthermore, ion-induced nucleation is not very likely as CO₂ is a nonpolar molecule and interacts only weakly and on very short distances with the electric charge of an ion. Consequently, heterogeneous nucleation is expected to be the major ice particle formation process [Listowski et al., 2014]. Here, the nature of the CO₂-ice nuclei is still unclear. Additionally, the CO₂ nucleation ability of the potential nuclei is highly uncertain due to a lack of CO₂ nucleation experiments on realistic particle materials and at realistic Martian mesospheric temperatures (70 K to 120 K). The next two sections discuss the potential condensation nuclei in the mesosphere of Mars and

the current scientific consensus of predicting onset conditions for CO₂ cloud formation.

3.2. Condensation nuclei

Heterogeneous nucleation is expected to be the major CO₂ ice particle formation process in the mesosphere of Mars with the nature of the nuclei still under discussion. Three different candidates have been discussed in literature.

(1) Martian Dust Particles (MDPs) which have been lifted up to the mesosphere might serve as nuclei for CO₂ ice clouds. During day, CO₂ clouds are located at altitudes between 60 and 85 km. A detached dust maximum at comparable altitudes between 45 and 65 km supports the scenario of MDPs as nuclei [Guzewich et al., 2013]. Additionally, Heavens et al. [2015] observed detached dust layers up to a height of 75 km near great elevations on Mars (Olympus Mons and Tharsis Montes). During night, however, the dust maximum is located between 15 and 30 km altitude [McCleese et al., 2010; Heavens et al., 2011a,b; Guzewich et al., 2013; Heavens et al., 2014], which challenges the importance of MDPs as nuclei for the highly elevated (80 to 100 km) night time CO₂ clouds.

(2) Besides MDPs, Meteoric Smoke Particles (MSPs) have been proposed to serve as nuclei. On Mars, the peak meteoric ablation altitude is between 60 and 100 km [Adolfsson et al., 1996; Whalley and Plane, 2010; Crismani et al., 2017] which matches the altitude of CO₂ cloud observations. Indeed, Listowski et al. [2014] needed to introduce MSPs as ice nuclei in addition to upward propagated MDPs to reproduce realistic mesospheric cloud patterns in their model.

(3) Recently, Plane et al. [2018] proposed an additional type of a potential condensation nucleus. Metal carbonates (FeCO₃ and MgCO₃) produced from the ablation of meteoric material in the CO₂ rich environment of the Martian mesosphere are expected to form clusters with six H₂O molecules. These clusters can coagulate and build-up dirty ice particles which may serve as condensation nuclei. In their model, the concentration of these ice particles is large enough to explain typical CO₂ ice cloud opacities.

3.3. Onset conditions for cloud formation

The formation process of CO₂ ice clouds in the Martian mesosphere is typically modeled using the surface diffusion approach of Classical Nucleation Theory (CNT). This approach is introduced in detail in Chapter 4. The main parameters which describe nucleation in CNT are two material properties, the desorption energy ΔF_{des} and the contact parameter m . The scientific community typically uses $\Delta F_{\text{des}} = 3.25 \times 10^{-20}$ J/molec and $m = 0.95$ irrespectively of the condensation nucleus [e.g. Colaprete et al., 2003; Määttänen et al., 2005; Listowski et al., 2014]. In the following this theory is used to derive conditions in the mesosphere of Mars at which CO₂ ice clouds are expected to form.

First, a representative CO₂ concentration profile in the Martian mesosphere has to be estimated. An exponential fit was performed to the variation of density with altitude measured during the entry process of Pathfinder [Magalhaes et al., 1999]. Here, I assume an atmospheric CO₂ content of 95 %. The corresponding saturation temperature with altitude is shown by the blue curve in Figure 3.2. For a representative particle

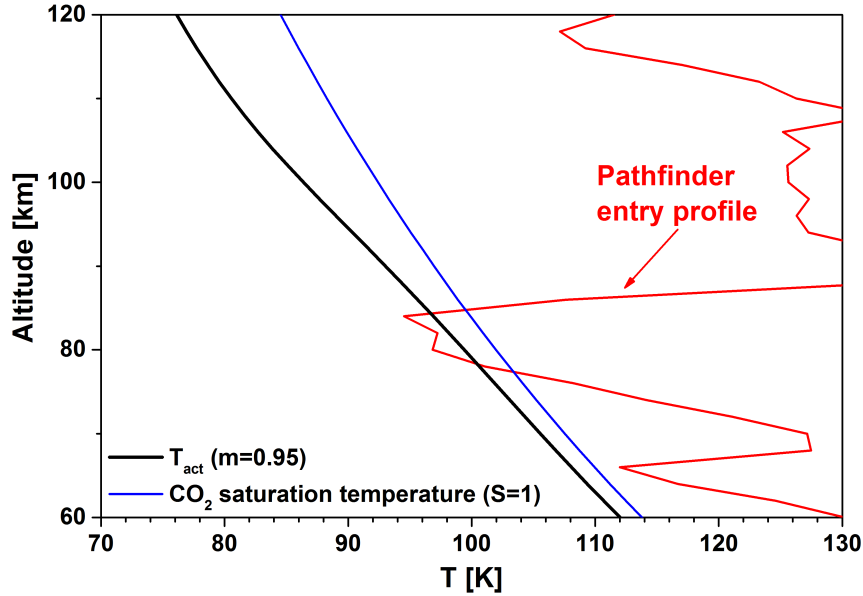


Figure 3.2.: Activation temperature T_{act} for CO₂ ice particle formation as a function of altitude. The black curve shows CNT calculations representing the current scientific consensus of activation temperatures. For comparison, the saturation temperature (blue curve) and the temperature profile measured during the entry process of Pathfinder (red curve) are shown [Magalhaes et al., 1999].

size as a function of altitude, I recall the mean particle size as a function of altitude from Listowski et al. [2014]. Mean particle radii are about 130 nm at 60 km altitude, 20 nm at 80 km altitude and 4 nm at 100 km altitude. CNT can be used with the particle size distribution and the CO₂ concentration profile to calculate the temperature, at which nucleation is activated on the particles. This temperature is from now on called activation temperature T_{act} . The result is shown by the black curve, which represents the current scientific consensus on activation temperatures as a function of altitude. Activation temperatures are 112 K at 60 km altitude and fall to 76 K at 120 km altitude. These temperatures are 2 to 8 K below the saturation temperature. Such temperatures below saturation temperature are frequently observed in the Martian mesosphere during the season of CO₂ cloud occurrence. The red curve in Figure 3.2 shows the temperature profile measured by Pathfinder while descending through the mesosphere [Magalhaes et al., 1999], which represents a rather typical temperature profile with temperatures below the saturation temperature [Forget et al., 2009].

According to this temperature profile and the CNT calculations, CO₂ clouds would form. This stands in contrast to observations. No clouds were observed during most of the nights when temperatures fell below the saturation temperature [Forget et al., 2009]. There are several explanations for the rare event of CO₂ cloud observations at nighttime. (i) There are not enough nuclei present, (ii) a sufficient number of nuclei is present but the CO₂ ice particles cannot grow to detectable sizes due to a short exposure time to supersaturated conditions and (iii) the nucleation ability of the particles is lower than in the reference case represented by the black curve in Figure 3.2.

The contact parameter of $m = 0.95$ is based on nucleation experiments using a H₂O ice covered surface [Glandorf et al., 2002]. The contact parameter m might be different for MSPs and MDPs. In addition, the temperatures in the laboratory experiment of Glandorf et al. [2002] are not representative for the Martian mesosphere since they are 20 to 50 K above saturation temperatures of CO₂. A temperature dependency of m is observed for H₂O ice and might be present for CO₂ as well. laboratory experiments on the CO₂ nucleation process on realistic nuclei materials and mesospheric temperatures are needed to constrain the contact parameter for conditions relevant to the Martian mesosphere. Such experiments are presented in Chapter 8. They serve to infer the desorption energy ΔF_{des} and the contact parameter m . The experimentally determined parameters are used to calculate activation temperatures T_{act} in the Martian mesosphere. These activation temperatures are then compared to the reference case presented in Figure 3.2 (black curve).

4. Microphysics of ice cloud formation

This chapter deals with the microphysical description of the formation and growth of H₂O and CO₂ ice particles at conditions relevant to the mesosphere of Earth and Mars. The main obstacle in forming ice particles in the atmosphere is the increasing saturation vapor pressure above a curved surface with decreasing radius of the ice particle. This effect is called Kelvin effect. It causes that high supersaturations are needed to form ice particles in the atmosphere solely out of the gas phase, which is a process termed homogeneous nucleation. Although homogeneous nucleation is not subject of the present study, it is introduced here since it provides the thermodynamic and kinetic basics for heterogeneous nucleation. Heterogeneous nucleation describes the ice particle formation process on preexisting particles, so called nuclei. After introducing the heterogeneous nucleation process, I discuss the effect of a particle charge on the nucleation process and finally present the ice particle growth model. Some parts of this chapter (Kelvin effect, influence of charge and the ice particle growth model) are adopted from my Master's thesis [Nachbar, 2014]. All material properties and parameters which are not explicitly discussed in the text of this chapter are summarized in Appendix B.

4.1. The Kelvin effect

If the pressure of a system stays constant, a thermodynamical process runs spontaneously when the Gibbs free energy G is minimized. Therefore, a process from one state into another runs spontaneously provided that $\Delta G < 0$ is fulfilled. Let us now assume, that a spherical cluster of molecules with radius r has formed at temperature T out of the gas phase. The change of the Gibbs free energy ΔG is the energy which is needed for the transformation process from the vapor phase to the cluster (either liquid or solid). This energy is called the free energy of forming a cluster and can be resolved into a negative volume term and a positive surface area term

$$\Delta G = - \underbrace{\frac{4\pi r^3 \rho}{3m_{\text{molec}}} \cdot k \cdot T \cdot \ln S}_{\text{volume term}} + \underbrace{4\pi r^2 \sigma}_{\text{surface area term}} . \quad (4.1.1)$$

The derivation of Equation 4.1.1 can be found in many textbooks dealing with nucleation theory, e.g. Roedel and Wagner [2011] or Pruppacher and Klett [2010]. The present concentration of molecules in the gas phase is described by the saturation $S = p_{\text{molec}}/p_{\text{sat}}$. Here, p_{molec} describes the pressure of the vapor species

and p_{sat} the saturation vapor pressure over a flat surface of the cluster material. $k=1.38065 \times 10^{-23}$ J/K is the Boltzman constant, m_{molec} the mass of one molecule, ρ the density and σ the surface tension of the cluster phase. The volume term on the right side of Equation 4.1.1 represents a negative term due to the attraction between single molecules in the cluster. The surface area term represents the free energy of surface formation. The influence of the volume term (negative) increases with particle size relative to the surface area term (positive). Figure 4.1 shows ΔG as a function of the ice cluster radius calculated exemplarily for hexagonal ice I_h . Here, a typical

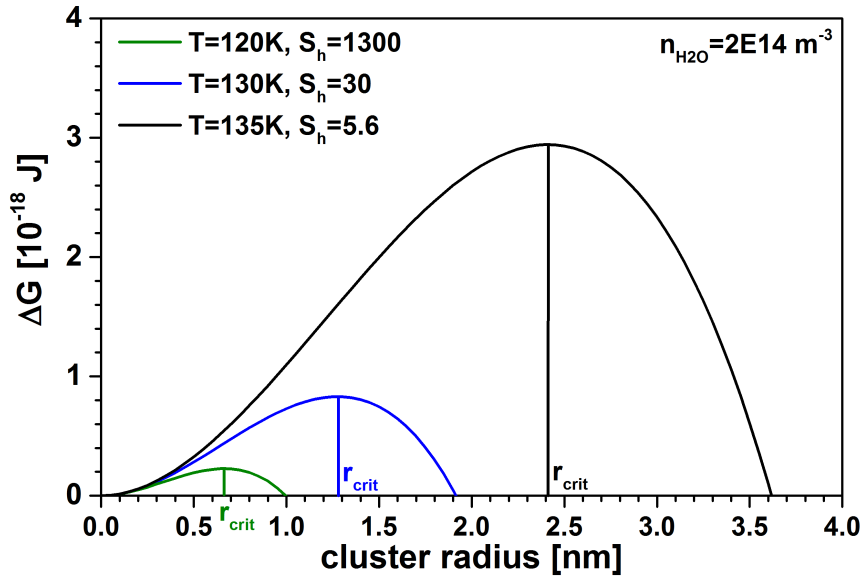


Figure 4.1.: Free energy of forming a cluster of hexagonal ice ΔG for typical polar summer mesopause temperatures of 120 K (green line), 130 K (blue line) and 135 K (black line) and a typical H_2O concentration of $2 \times 10^{14} \text{ m}^{-3}$ (2 ppm at about 87 km of height).

summer mesopause water vapor concentration of $n_{\text{H}_2\text{O}} = 2 \times 10^{14} \text{ m}^{-3}$ corresponding to about 2 ppm at a height of 87 km was assumed [Seele and Hartogh, 1999]. Three ΔG curves are shown for temperatures of 120 K (green line), 130 K (blue line) and 135 K (black line). For all three temperatures, ΔG has an unstable maximum at a certain critical radius r_{crit} . If an ice particle smaller than r_{crit} forms, it is energetically favorable to reduce its size and therefore it would sublime. In contrast, an ice particle larger than r_{crit} reduces its energy by growing due to accretion of additional water molecules from the surrounding vapor. If the particle has exactly the size of r_{crit} it is in an unstable equilibrium as long as the conditions do not change. Fluctuations in temperature and H_2O concentration then trigger sublimation or growth of the ice particle. The energy ΔG^* needed to form a critical cluster with radius r_{crit} is called Kelvin barrier. Solving Equation 4.1.1 for $\left. \frac{dG}{dr} \right|_{r_{\text{crit}}} = 0$ yields in the critical radius and the equilibrium saturation value S_{eq} that is needed for a particle of size r to be in

equilibrium.

$$r_{\text{crit}} = \frac{2m_{\text{molec}}\sigma}{kT\rho \ln S} \quad (4.1.2)$$

$$S_{\text{eq}} = \exp\left(\frac{2m_{\text{molec}}\sigma}{kT\rho r}\right) \quad (4.1.3)$$

The equilibrium saturation over a curved surface S_{eq} is called Kelvin effect and is shown in Figure 4.2 as a function of particle radius at 130 K assuming hexagonal ice I_h . The Kelvin effect is significantly enhanced with respect to $S=1$ for nanometer sized

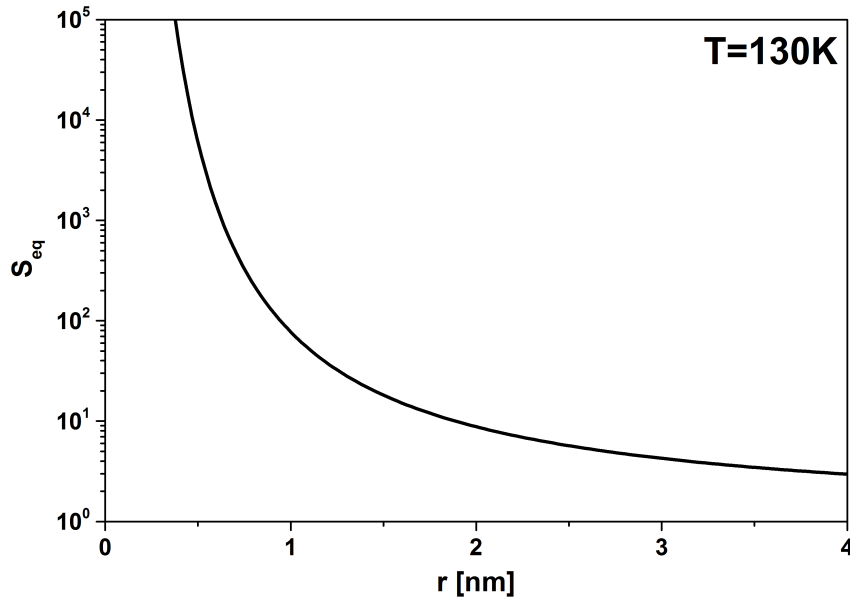


Figure 4.2.: Equilibrium saturation over a curved surface (Kelvin effect) as function of the particle radius at 130 K assuming hexagonal ice I_h .

particles and increases with decreasing particle radius. This can be easily described from a microphysical point of few Saturation ($S=1$) describes the state at which the deposition flux of molecules from the gas phase equals the temperature dependent sublimation flux over a planar surface of a solid or liquid phase. For a strongly curved surface, the outer most molecules have on average less binding partners compared to a flat surface and thus are less efficiently bound and more easily released to the gas phase. Therefore, the sublimation flux and thus the equilibrium saturation over a curved surface S_{eq} is higher than compared to a planar surface.

Evaluating Equation 4.1.1 at r_{crit} gives the energy needed to form an ice particle of critical size (Kelvin barrier) at a given temperature and water vapor concentration

$$\Delta G^* = \frac{4\pi r_{\text{crit}}^2 \sigma}{3}. \quad (4.1.4)$$

4.2. Homogeneous nucleation

Classical homogeneous nucleation theory describes the process of forming a supercritical cluster, i.e. a cluster larger than the critical size (Equation 4.1.2) from the gas phase. Since this work does not deal with homogeneous nucleation, it is only briefly introduced here and the interested reader is referred to Pruppacher and Klett [2010]. In general, the concentration of clusters containing i molecules (c_i) in the gas phase may be calculated from a Boltzmann distribution with $c_i = c_1 \cdot \exp[\Delta G_i / (kT)]$. ΔG_i is the energy of forming a cluster consisting of i molecules and $c_1 = n_{\text{molec}} = p / (kT)$ is the concentration of monomers, i.e. the concentrations of the molecules in the gas phase. The concentration of critical clusters c_{crit} is thus described by

$$c_{\text{crit}} = n_{\text{molec}} \cdot \exp[\Delta G_{\text{hom}}^* / (kT)], \quad (4.2.1)$$

with ΔG_{hom}^* described by Equation 4.1.4. If a monomer is added to such a critical cluster, the cluster gets supercritical and grows further in time. Such a process is called nucleation. Accordingly, the homogeneous nucleation rate J_{hom} can be calculated by multiplying c_{crit} with the flux of gas phase molecules approaching a critical cluster β_{hom} which is

$$\beta_{\text{hom}} = A_{\text{crit}} \cdot \frac{n_{\text{molec}} \cdot v_{\text{th}}}{4}. \quad (4.2.2)$$

A_{crit} is the surface area of a spherical cluster with radius r_{crit} . The mean thermal velocity of the molecules in the gas phase is calculated with $v_{\text{th}} = \sqrt{8kT / (\pi m_{\text{molec}})}$. However, the equilibrium concentration of critical clusters according to the Boltzmann distribution does not describe the steady state concentration of critical clusters in a system where critical clusters are constantly removed due to nucleation. Hence, the nucleation rate is smaller than in the simple approach introduced above, which is considered by the so called Zeldovic factor

$$Z_{\text{hom}} = \sqrt{\Delta G_{\text{hom}}^* / (3\pi kT_N n_{\text{crit}}^2)}. \quad (4.2.3)$$

$n_{\text{crit}} = 4\pi r_{\text{crit}}^3 \rho / 3m_{\text{molec}}$ is the concentration of molecules in a critical cluster.

The heat of condensation released during embryo growth might significantly offset the temperature of the embryo with respect to the ambient temperature. The potential heating of the embryo reduces the nucleation rate. This is usually considered by multiplying the nucleation rate with the so called isothermal coefficient $f_{\delta T}$ ($0 < f_{\delta T} < 1$) which depends on the background pressure and the growth rate of the cluster. Considering these correction factors, the homogeneous nucleation rate is described by

$$J_{\text{hom}} = f_{\delta T} \cdot Z_{\text{hom}} \cdot \beta_{\text{hom}} \cdot c_{\text{crit}}. \quad (4.2.4)$$

The free energy of forming a critical cluster ΔG_{hom}^* is a function of saturation S and temperature T . The dependency of ΔG_{hom}^* on S is depicted in Figure 4.1. For a constant H₂O concentration of $2 \times 10^{14} \text{ m}^{-3}$, the saturation S increases with decreasing temperature (5.6 at 135 K, 30 at 130 K and 1300 at 120 K). Such a temperature

drop from 135 K to 120 K can be caused by a strong gravity wave passing through the mesopause region. As a consequence, the critical cluster size r_{crit} and ΔG_{hom}^* decrease as temperatures fall. This leads to a higher steady state concentration of critical clusters and thus higher homogeneous nucleation rates with decreasing temperature. In the terrestrial mesopause, homogeneous nucleation of H_2O might be activated during very strong cooling rates [Murray and Jensen, 2010]. In the case of CO_2 in the mesosphere of Mars, however, temperatures about 50 K below frost point would be needed to create enough critical clusters to form clouds [Määttä et al., 2010]. Such cold temperatures correspond to saturations in excess of 100 000 which have never been observed.

Even under conditions on Earth allowing for the activation of homogeneous nucleation, that process still is in competition with the so called heterogeneous nucleation process. Heterogeneous nucleation describes the ice formation process on preexisting particles. The saturation needed for critical cluster formation on a nucleus depends on the size and the material of the nucleus, but is typically far below the saturation needed for homogeneous cluster formation.

4.3. Heterogeneous nucleation

Heterogeneous nucleation describes the ice formation process on preexisting particles, so called nuclei. In this work, the surface diffusion approach of classical nucleation theory is used and is from now on called CNT. Figure 4.3 illustrates the main physical mechanisms involved in heterogeneous nucleation on a spherical nucleus (shown in green). A nucleus floating in the atmosphere is subject to collisions with gas molecules,

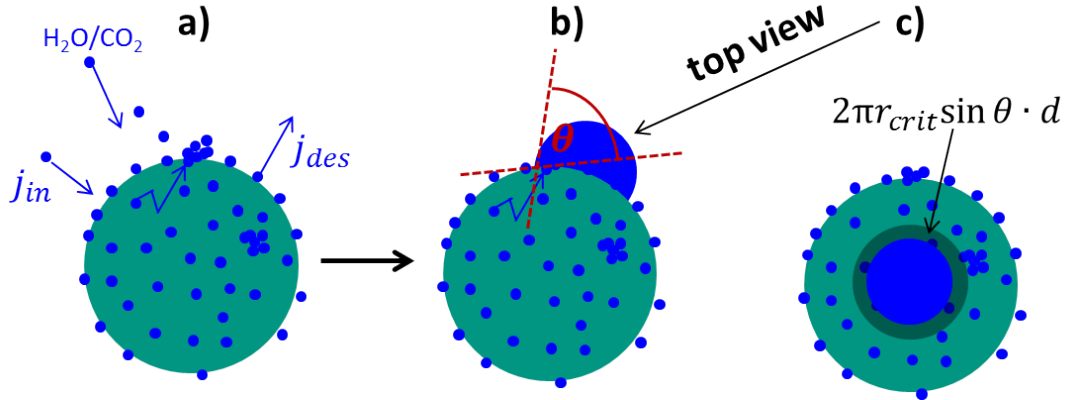


Figure 4.3.: Illustration of the main physical mechanisms involved in heterogeneous nucleation induced by surface diffusion. The nucleus is represented in green and the molecules in blue. See text for more details.

in our case CO_2 or H_2O (shown in blue). These molecules adsorb on the nucleus for a

certain amount of time, which leads to the build-up of a surface concentration of adsorbed molecules $c_{1,s}$ (panel a). These adsorbed molecules may diffuse onto the surface of the nucleus, encounter other molecules and form clusters. The clusters might eventually reach the critical size and get stable as indicated in panel b). The steady state concentration of critical clusters on the nucleus surface is calculated in analogy to homogeneous nucleation by multiplying the surface concentration of adsorbed molecules $c_{1,s}$ with $\exp(-\Delta G_{\text{het}}^*/(kT_N))$. Here, ΔG_{het}^* is the free energy of forming a critical cluster on the nucleus surface. Multiplying the concentration of critical clusters with the surface area of the nucleus A_N , the diffusional flux of molecules on the nucleus surface to a critical cluster β_{het} , and the heterogeneous Zeldovic factor Z_{het} yields the nucleation rate per particle

$$J_{\text{het}} = A_N \cdot Z_{\text{het}} \cdot \beta_{\text{het}} \cdot c_{1,s} \cdot \exp\left(\frac{-\Delta G_{\text{het}}^*}{kT_N}\right). \quad (4.3.1)$$

The following introduces how to calculate the surface concentration of adsorbed molecules $c_{1,s}$, the free energy of forming a critical cluster ΔG_{het}^* , the diffusional flux of molecules to the critical cluster β_{het} and the heterogeneous Zeldovic factor Z_{het} .

The surface concentration of adsorbed molecules

The collision rate of molecules with the nucleus is described in analogy to Equation 4.2.2 by

$$j_{\text{in}} = A_N \cdot \frac{n_{\text{molec}} \cdot v_{\text{th}}}{4} = A_N \cdot S \cdot \frac{p_s(T_{\text{env}}) \cdot v_{\text{th}}}{4kT_{\text{env}}}. \quad (4.3.2)$$

$A_N = 4\pi r_N^2$ is the surface area of the nucleus and $p_s(T_{\text{env}})$ the saturation vapor pressure for the gas temperature T_{env} of the species under consideration. Molecules which collide with a nucleus adhere on it for a certain amount of time. The time the molecules are adsorbed on the nucleus surface depends on the desorption energy ΔF_{des} , the energy a molecule needs to detach from the nucleus surface. The flux of desorbing molecules from the particle surface is expressed by

$$j_{\text{des}} = A_N \cdot c_{1,s} \cdot \nu \cdot \exp\left(-\frac{\Delta F_{\text{des}}}{kT_N}\right). \quad (4.3.3)$$

Here, ν is the vibration frequency of a molecule on the nucleus surface and T_N the temperature of the nucleus. Note that the nucleus temperature might be increased with respect to the ambient temperature due to absorption of solar irradiation at a low pressure environment. The desorption flux is proportional to the surface concentration of adsorbed molecules $c_{1,s}$. Equalizing the incoming (Equation 4.3.2) and desorbing molecule flux (Equation 4.3.3) yields in the equilibrium concentration of adsorbed monomers $c_{1,s}$ at temperature T_{env} and gas phase molecule concentration n_{molec}

$$c_{1,s} = \frac{n_{\text{molec}} \cdot \sqrt{kT_{\text{env}}}}{\nu \sqrt{2\pi m_{\text{molec}}}} \cdot \exp\left(\frac{\Delta F_{\text{des}}}{kT_N}\right). \quad (4.3.4)$$

The free energy of forming a critical cluster

As illustrated in panel b) of Figure 4.3, the surface of the nucleus reduces the amount of molecules needed to form a cluster of critical curvature as well as the cluster surface area exposed to air. The former changes the volume term and the latter the surface area term in Equation 2.4.1. As a result, ΔG_{het}^* is reduced with respect to homogeneous nucleation:

$$\Delta G_{\text{het}}^* = f \cdot \Delta G_{\text{hom}}^*. \quad (4.3.5)$$

The reduction of the free energy to form a critical cluster is described by the geometrical reduction factor f which has been determined by means of geometrical considerations for a planar surface to

$$f(m) = \frac{(2+m) \cdot (1-m)^2}{4}. \quad (4.3.6)$$

The contact parameter m is a measure for the match of the particle surface properties to the one of an ice surface and is described by Young's relation

$$m = \cos \theta = \frac{\sigma_{\text{N}} - \sigma_{\text{N-ice}}}{\sigma_{\text{ice}}}, \quad (4.3.7)$$

where σ_{N} describes the free surface energy of the nucleus with respect to air, $\sigma_{\text{N-ice}}$ the nucleus/ice interface surface energy and σ_{ice} the ice surface energy with respect to air. A geometrical interpretation of m is given by $m = \cos \theta$ with θ representing the contact angle between the nucleus and the ice embryo as indicated in Figure 4.3. The contact parameter m has a range of -1 to 1. If m equals 1, $\Delta G_{\text{het}}^* = 0$ and there is a perfect match between the surface properties of the nucleus and the embryo. Such an embryo is called completely wettable. This implies that a molecule adsorbing on the nucleus surface experiences the same binding energy as on a cluster of molecules of the same size. Thus, if m equals 1 CNT is not needed to describe the nucleation process and growth is activated for a nucleus larger than the critical radius (Equation 4.1.2). If m is smaller than 1, $\Delta G_{\text{het}}^* > 0$ and CNT is needed to describe the nucleation process.

For nucleation on small particles, the geometrical correction factor $f(m)$ has to be modified in order to take the curvature of the substrate into account. According to Fletcher [1958], the geometrical correction factor for a nucleus of radius r_{N} is:

$$f(m, x) = 0.5 \cdot \left[1 + \left(\frac{1 - mx}{\phi} \right)^3 + x^3 (2 - 3k + k^3) + 3mx^2 (k - 1) \right], \quad (4.3.8)$$

with

$$k = \frac{x - m}{\phi} \quad (4.3.9)$$

$$\phi = \sqrt{1 - 2mx + x^2} \quad (4.3.10)$$

$$x = \frac{r_{\text{N}}}{r_{\text{crit}}} \quad (4.3.11)$$

In the limit of large particles, Equation 4.3.8 reduces to the expression for a flat surface (Equation 4.3.6).

The diffusional flux of molecules to the critical cluster

The diffusional flux of molecules to a critical cluster β_{het} is calculated by multiplying the amount of molecules which are located close enough to the cluster to join the germ with one diffusion step and the diffusion frequency ($\nu \cdot \exp(-\Delta F_{\text{sd}} / (kT_{\text{N}}))$). The estimation of the amount of molecules which are able to join the germ is illustrated by the grey shaded area in Figure 4.3 (panel c). The length of the interface line between critical cluster and nucleus ($2\pi r_{\text{crit}} \sin \theta$) times the mean jumping distance of a molecule during one diffusion step d gives the area around a critical cluster from which molecules can reach the critical cluster within one diffusion step. Multiplication with the surface concentration $c_{1,s}$ results in

$$\beta_{\text{het}} = c_{1,s} \cdot 2\pi r_{\text{crit}} d \sin \theta \cdot \nu \cdot \exp(-\Delta F_{\text{sd}} / (kT_{\text{N}})). \quad (4.3.12)$$

The energy of surface diffusion ΔF_{sd} is typically assumed to be $\Delta F_{\text{des}} / 10$.

The heterogeneous Zeldovic factor

The Zeldovic factor for heterogeneous nucleation on a planar surface can be expressed as function of the Zeldovic factor for homogeneous nucleation (Equation 4.2.3)

$$Z_{\text{het}} = \frac{Z_{\text{hom}}}{\sqrt{f}}, \quad (4.3.13)$$

with f given by Equation 4.3.6. In case of a curved surface, this modifies to [Vehkamaeki et al., 2007]

$$Z_{\text{het, c}} = Z_{\text{hom}} \cdot \sqrt{\frac{4}{2 + \frac{(1-mx) \cdot [2-4mx - (m^2-3) \cdot x^2]}{(1-2mx+x^2)^{\frac{3}{2}}}}}. \quad (4.3.14)$$

For large particles, Equation 4.3.14 converges Equation 4.3.13.

The non-isothermal coefficient

The non-isothermal coefficient is excluded in the equation for the heterogeneous nucleation rate (Equation 4.3.1). This is because the influence of the heat of condensation during embryo growth on the nucleation rate can be neglected in the experiments with MICE-TRAPS as well as in condensation calculations relevant for the atmospheres of Earth and Mars. In the laboratory experiments performed in this work, a binary gas mixture of Helium and CO₂ or H₂O is present at a ratio of 100:1 and higher. This ensures isothermal conditions as discussed in my Master's Thesis [Nachbar, 2014] or Duft et al. [2015]. The same thermal conditions apply for the terrestrial mesopause as efficient heat dissipation is provided by oxygen and nitrogen molecules of the ambient

air. The efficiency of heat dissipation from the embryo is greatly reduced if the main constituent of the atmosphere nucleates. This is the case for CO₂ (95 % of the atmosphere) for the Martian atmosphere. Määttänen et al. [2007], however, argued that $f_{\delta T}$ can be assumed to be 1 in the Martian atmosphere due to a good embryo-nucleus contact.

Nucleation via direct deposition from the gas phase

Many studies describe the nucleation process not as discussed in this chapter by diffusion of surface molecules to a critical cluster, but via direct deposition of molecules from the gas phase [e.g. Trainer et al., 2009; Iraci et al., 2010; Phebus et al., 2011]. In these studies, the surface concentration of molecules $c_{1,s}$ which is needed to describe the critical cluster concentration is typically assumed to be one monolayer. The flow of molecules from the gas phase to a critical cluster is then described by Equation 4.2.2 with A_{crit} being substituted by the contact parameter dependent surface area of a critical cluster exposed to the gas phase. I consider these simplifications as not suitable since surface diffusion of molecules to a critical cluster is always larger than via direct deposition from the gas phase by a factor of $\exp[(\Delta F_{\text{des}} - \Delta F_{\text{sd}}) / (kT)]$ [Pruppacher and Klett, 2010]. For H₂O nucleation at conditions of the terrestrial mesopause and a typically assumed desorption energy of $\Delta F_{\text{des}} = 2.9 \times 10^{-20}$ J/molec, the difference in nucleation rates between both approaches is about 6 orders of magnitude.

Conceptual issues and limitations of CNT

Critical cluster sizes at typical mesopause conditions are in the order of 1 nm. Considering heterogeneous nucleation, this corresponds to less than 100 molecules forming a critical cluster on the nucleus surface. In classical nucleation theory, bulk properties like the surface tension and the density of ice are used to describe the properties of a critical cluster and might not be valid for such small clusters.

Using a single desorption energy to describe the adsorption process is only a very rough estimate. For instance, it was shown in the case of water adsorption on iron oxide and silica that the binding energy of the adsorbent molecules can be strongly coverage dependent [Navrotsky et al., 2008; Sneh et al., 1996]. The constant desorption energy used in nucleation theory might therefore be regarded as a mean desorption energy representing the whole landscape of desorption energies on a surface with typical coverages close to nucleation threshold. Additionally, adsorbed water might dissociate to a hydroxyl radical (OH) [Kendelewicz et al., 2013], which is eventually bound to the surface and hence not available for the nucleation process.

Sensitivity of the nucleation rate on ΔF_{des} , m and T

Predicting conditions at which ice formation is activated in the terrestrial mesopause or the Martian mesosphere is subject to very large uncertainties. This is since the most important parameters which describe the nucleation process in CNT are only poorly

known. These parameters are the desorption energy ΔF_{des} and the contact parameter m . Both parameters are material properties and depend on the particle material. The dependency of calculated nucleation rates on the desorption energy and the contact parameter is shown in Figure 4.4 for H_2O and typical conditions of the polar mesopause ($T=130\text{ K}$ and $n_{\text{H}_2\text{O}} = 2 \times 10^{14}\text{ m}^{-3}$). The reference case (black line) was calculated

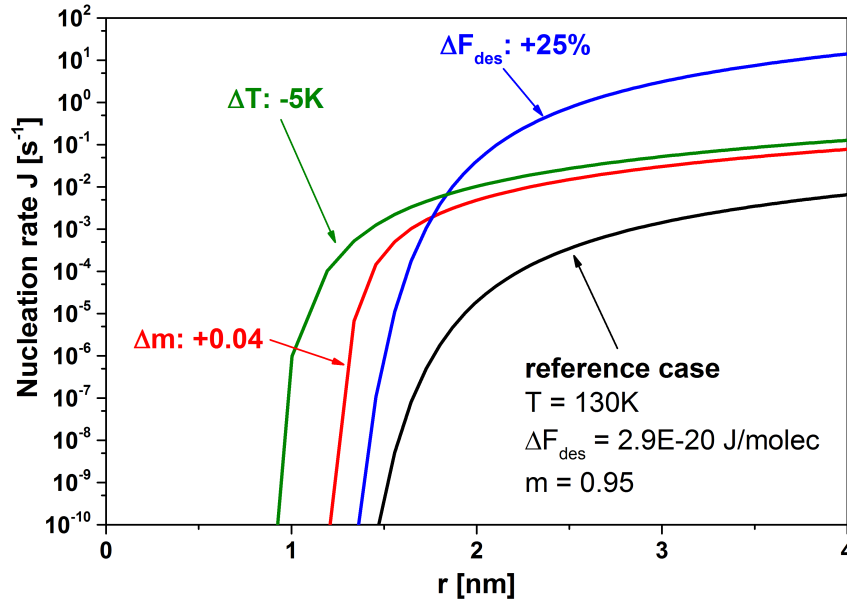


Figure 4.4.: Sensitivity of the size dependent nucleation rate per particle on contact parameter m , desorption energy ΔF_{des} , and temperature T .

using a contact parameter of 0.95 and a desorption energy of $2.9 \times 10^{-20}\text{ J/molec}$ [e.g. Rapp and Thomas, 2006; Asmus et al., 2014; Määttänen et al., 2005; Bardeen et al., 2010]. Changing the desorption energy by only 25% varies the nucleation rate by several orders of magnitude, especially for typical MSP radii below 1.5 nm (blue line). The red line in Figure 4.4 illustrates the sensitivity of the nucleation rate on the contact parameter m . Changing m by about 5% has comparable effects on the nucleation rate as changing the desorption energy by 25%. The nucleation rate is to both changes as sensitive as a change in the temperature by about 5 K as indicated by the green line. Hence, the temperature needed to activate ice particle formation is strongly affected by the choice for the desorption energy and the contact parameter.

4.4. Influence of charge

In summer the background gas in the terrestrial mesopause is partially ionized due to the strong solar UV radiation. Consequently, the mesopause is a highly dynamical environment for meteoric smoke particles. The distribution of charge states of MSPs

in such a plasma depends on many factors including collision rates with neutral and ionized gas molecules, electron capture and electron recombination rates. Recent model studies estimated that on average most of the MSPs in the summer mesopause are in neutral charge state, while about 10% carry a single negative charge [Plane et al., 2014, 2015]. The charge of these particles is expected to reduce the free energy of cluster formation ΔG^* due to charge-dipole interactions which causes ice formation on smaller particles compared to neutral particles. Until present, this effect is not considered in any PMC models, but was proposed to represent a potential key role in understanding PMC observations [Gumbel and Megner, 2009; Megner and Gumbel, 2009]. The following discusses the possible effects of the elementary charge of MSPs on the nucleation process of ice particles. We start with the simple case of completely wettable nuclei ($m=1$) and then discuss incompletely wettable nuclei ($m<1$).

Completely wettable nuclei

Let us first consider the influence of a charge on the vapor pressure above a pure liquid or solid particle consisting of H_2O or CO_2 . In the first most simple case, we assume that the charge is located in the center of the spherical particle. Note that this case is equivalent to a completely wettable nucleus (contact parameter $m = 1$) with the charge located in the center of the nucleus. The electric field of the charge sitting in the center of the particle interacts with the molecules in a dielectric medium. Consequently, the electric field decreases more rapid with distance as compared to vacuum. This effect results in a decrease of the Gibbs free energy. It is here referred to as "dielectric effect" which can be considered by adding a Coulomb term to ΔG_{hom} in Equation 4.1.1 [e.g. Castleman and Tang, 1972; Gumbel and Megner, 2009; Keesee, 1989]

$$\Delta G_{q, \epsilon_r} = \Delta G_{\text{hom}} + \frac{q^2}{8\pi\epsilon_0} \left(1 - \frac{1}{\epsilon_r}\right) \cdot \left(\frac{1}{r} - \frac{1}{r_I}\right). \quad (4.4.1)$$

Here, r_I is the radius of the nucleus, q is the charge of the ion, $\epsilon_0=8.854 \times 10^{-12}$ C/Vm the vacuum permittivity and ϵ_r the relative permittivity of the cluster material. Solving this equation for $\Delta G_{q, \epsilon_r}^*$ (as described in Section 4.1) results in a reduced equilibrium saturation over a charged cluster $S_{\text{eq}}^{q, \epsilon_r}$

$$S_{\text{eq}}^{q, \epsilon_r} = \exp \left(\frac{2m_{\text{molec}}\sigma}{kT\rho r} - \underbrace{\frac{m_{\text{molec}} q^2 \left(1 - \frac{1}{\epsilon_r}\right)}{32\pi^2\epsilon_0 kT\rho r^4}}_{\text{dielectric term}} \right). \quad (4.4.2)$$

The dielectric effect describes the reduced saturation above a charged particle due to the interaction of the molecules of the particle with the charge. However, the electric field of the charge also interacts with gas phase molecules which, according to Lapshin et al. [2002], might cause an additional reduction of the equilibrium saturation. In a gas without an electric field, the permanent dipole moment of molecules is randomly

oriented. In the Coulomb field $E = q / (4\pi\epsilon_0 r^2)$ of the ion core, however, they are exposed to a torque. On average the dipole of the molecules orients to some extent along the electric field vector which introduces a mean force in charge direction due to the inhomogeneous electric field. This causes a mean attraction of polar gas molecules to a charged nucleus which increases the gas phase concentration of these molecules right above the cluster surface. Hence, the equilibrium saturation is reduced as follows

$$S_{\text{eq}}^{\text{q}, \epsilon_r + \mu} = S_{\text{eq}}^{\text{q}, \epsilon_r} \cdot \underbrace{\exp\left(-\frac{\bar{\mu} E}{kT}\right)}_{\text{dipole term}}. \quad (4.4.3)$$

Here, $\bar{\mu}$ represents the mean dipole moment with respect to the orientation of the molecule in the electric field. Assuming that the orientation of the dipole moment in the electric field is distributed according to a Boltzmann distribution yields

$$\bar{\mu} = \mu \cdot L\left(\frac{\mu E}{kT}\right), \quad (4.4.4)$$

with the Langevin function

$$L\left(\frac{\mu E}{kT}\right) \approx \frac{\mu E}{3kT}. \quad (4.4.5)$$

A detailed derivation of the dipole effect on the equilibrium saturation can be found in [Lapshin et al. \[2002\]](#). In analogy to the dipole effect, molecules can be polarized in the electric field causing an additional reduction of the saturation vapor pressure. The induced dipole moment is described by the polarizability p of the molecule and can be calculated by $\mu_{\text{ind}} = p \cdot E$. Combining all charge effects yields

$$S_{\text{eq}}^{\text{q}, \epsilon_r + \mu + p} = \exp\left(\frac{2m_{\text{molec}}\sigma}{kT\rho r} - \underbrace{\frac{m_{\text{molec}} q^2 \left(1 - \frac{1}{\epsilon_r}\right)}{32\pi^2 \epsilon_0 kT \rho r^4}}_{\text{dielectric term}} - \underbrace{\frac{\mu^2 E^2}{3k^2 T^2}}_{\text{dipole term}} - \underbrace{\frac{pE^2}{kT}}_{\text{pol. term}}\right). \quad (4.4.6)$$

All these charge effects have a negative contribution to the exponent in Equation 4.4.6 and therefore reduce the equilibrium saturation S_{eq} .

The size dependent influence of the different charge effects on S_{eq} at typical mesospheric conditions is illustrated in Figure 4.5. The upper and lower panel show S_{eq} for water ice particles at 130 K assuming hexagonal ice I_h and CO_2 ice particles at 70 K, respectively. For water ice particles in the shown size range, the polarizability and the dielectric effect are weak compared to the effect of the permanent dipole moment. The influence of all effects increases with decreasing particle radius. Considering all charge effects, they significantly reduce equilibrium saturations for particle radii below 3 nm. The horizontal black dashed line in the upper panel represents a typical H_2O number density of $2 \times 10^{14} \text{ m}^{-3}$ ($S_h \approx 30$). For such conditions and assuming MSPs to be perfect nuclei, neutral particles larger than approximately 1.2 nm in radius would

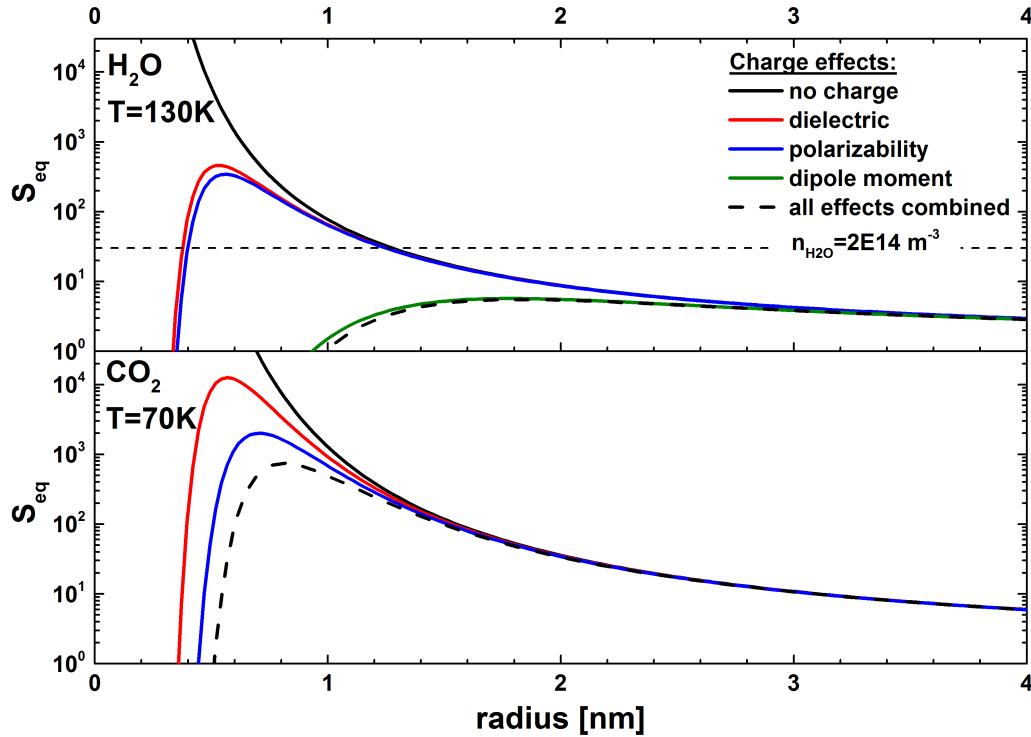


Figure 4.5.: Influence of charge on the equilibrium saturation over the curved surface of a completely wettable particle (Kelvin effect). Calculations are shown considering no charge effects (black line), the dielectric effect (red line), the polarizability effect (blue line), the permanent dipole moment effect (green line) and all charge effects combined (black dashed line). The upper panel shows calculations for H₂O at 130 K and the lower panel shows calculations for CO₂ at 70 K.

grow further in time. Smaller particles, however, are not able to trigger ice particle formation. The picture changes, if the particles carry one elementary charge. Then, $S_h \approx 30$ (a number density of $2 \times 10^{14} \text{ m}^{-3}$) is larger than the equilibrium saturation for all particle sizes. Thus, all charged MSPs independent of their size would activate ice particle growth at typical mesopause conditions. In consequence the charged MSP population is expected to play a major role in observed ice particle concentrations on the order of $1 \times 10^3 \text{ cm}^{-3}$ [Gumbel and Megner, 2009; Megner and Gumbel, 2009]. The lower panel of Figure 4.5 shows the Kelvin effect for CO₂ at 70 K corresponding to extreme cold temperatures of the Martian mesosphere. Color codes of the lines are identical to the upper panel, but no curve is included for the permanent dipole effect since CO₂ is a non-polar molecule. In general, charge effects for CO₂ are weaker as compared to H₂O and only become significant for radii smaller than 1.6 nm.

Incompletely wettable nuclei

The description of charge effects as discussed above is only valid in the case of a completely wettable nucleus (contact parameter $m = 1$) with the charge located in the center of the nucleus. If the nucleus is not completely wettable, nucleation theory must be used to describe the ice particle formation process. Then, the nucleus is not covered by a homogeneous layer of H_2O molecules, but clusters form on the nucleus surface and the charge effect on these clusters needs to be determined. To this end, Equation 4.1.1 can still be used when interpreting r as the radius of the ice cluster on the nucleus. In addition, all charge effects discussed above should be added with the correct distance of the ice cluster from the center of the nucleus, which yields

$$\Delta G_q = \Delta G(r_{\text{cluster}}) + \Delta G_q(r_N + r_{\text{cluster}}) . \quad (4.4.7)$$

Here, $\Delta G_q(r_N + r_{\text{cluster}})$ describes the reduction of the free energy of forming an ice cluster of the size r_{cluster} sitting on a nucleus due to a charge located in the center of the nucleus. If the charge is not located in the center of the nucleus, ΔG_q has to be calculated using the distance between the charge and the cluster r_q instead of the radius of the nucleus r_N . Equation 4.4.7 has to be solved for $r_{\text{cluster, crit}}$ in order to calculate the Kelvin barrier including charge effects ΔG_q^* . Then, ΔG_q^* can be used to calculate the heterogeneous Kelvin barrier for a charged nucleus (Equation 4.3.5) and the nucleation rate (Equation 4.3.1). Problematic is that the reduction of the the Kelvin barrier for heterogeneous nucleation described by f is a purely geometrical consideration which does not consider charge effects. If an ice cluster nucleates heterogeneously on a charged nucleus, a reduction of $r_{\text{cluster, crit}}$ also leads to an increase of the charge effects since the ice cluster is, on average, located nearer to the charge. This effect is not considered by f . In addition, [Keesee \[1989\]](#) pointed out that stable but sub-critical ice clusters (which do not increase in size due to accretion of single water molecules) form on a nucleus due to charge-dipole interactions. The probability that such small clusters form on a charged nucleus is larger than the probability of forming a critical ice cluster. Therefore, the probability leading to stable sub-critical clusters in combination with the probability at which these clusters could combine to an ice embryo larger than the critical cluster has to be considered. To the best of the author's knowledge no comprehensive nucleation theory considering charge effects on incompletely wettable particles exists so far. Since charge effects in heterogeneous nucleation on incompletely wettable particles turn out to be unimportant for the data analysis in this work, attempts to describe these charge effects are not discussed further.

4.5. Ice particle growth

In general, the mass growth rate dm/dt of H_2O or CO_2 ice particles can be expressed as the difference between the vapor deposition rate (k_{dep}) on the particle surface and

the sublimation rate (k_{sub}) from the particle surface

$$\frac{dm}{dt} = [k_{dep} - k_{sub}] \cdot m_{molec}, \quad (4.5.1)$$

with the molecular mass m_{molec} . The deposition rate depends on the sticking coefficient, which is defined as the probability that a molecule is adsorbed when hitting a surface. For all experimental conditions employed in this work ($T < 160$ K for H_2O and $T < 90$ K for CO_2), a sticking coefficient of unity for water molecules on water ice [Batista et al., 2005; Brown et al., 1996; Gibson et al., 2011; Kong et al., 2014] and for CO_2 molecules on CO_2 ice [Heald and Brown, 1968; Weida et al., 1996] is valid. Under this condition, a simple growth model can be used which compares the flux density of incoming (j_{in}) and outgoing molecules (j_{out})

$$\frac{dm}{dt} = [A_c(t) \cdot j_{in} - A_p(t) \cdot j_{out}(r_p)] \cdot m_{molec}. \quad (4.5.2)$$

$A_p = 4\pi r_p^2$ is the particle surface area assuming spherical particles, $A_c = 4\pi (r_p + r_{molec})^2$ is the effective surface area describing the collision of a molecule with the particle and r_p is the time dependent particle radius. The hard sphere collision radius of a molecule r_{molec} may not be neglected here due to the small size of the particles investigated in this work ($1 \text{ nm} < r_p < 6 \text{ nm}$). The flux density j_{out} emitted from the particle is given by the equilibrium saturation S_{eq} over the curved particle surface (Kelvin effect, Equation 4.1.3) multiplied with the sublimation rate over a planar surface which depends on the saturation vapor pressure $p_{sat}(T)$:

$$j_{out} = S_{eq}(r_p, T_p) \cdot \frac{p_{sat}(T_p) \cdot v_{th,p}}{4kT_p}. \quad (4.5.3)$$

$v_{th,p}$ is the mean thermal velocity of molecules at particle temperature T_p . If charge effects shall be considered, the charge dependent Kelvin effect according to Equation 4.4.6 has to be used.

All experiments presented in this study were performed in the free molecular regime and the mean free path of molecules in the gas phase was much larger than the particle size (high Knudsen numbers). The same applies to the terrestrial mesopause. For example, the mean free path length at a typical mesopause altitude of 85 km is on the order of 1 cm, which is much larger than the nanometer sized PMC particles. The incoming flux density of molecules j_{in} is thus not limited by diffusion of molecules through a viscous medium and is described by

$$j_{in} = \frac{n_{molec} \cdot v_{th}}{4} = S \cdot \frac{p_{sat}(T) \cdot v_{th}}{4kT}. \quad (4.5.4)$$

The molecule concentration in the gas phase n_{molec} is described by the saturation $S = p_{molec}/p_{sat}$ of the molecules with respect to the temperature dependent saturation vapor pressure p_{sat} of the investigated species at gas phase temperature T .

In growth regime, the particle surface area as well as the size dependent equilibrium saturation S_{eq} change with time and therefore Equation 4.5.2. has to be numerically solved. The radius of the particle r_p can be calculated for each time step according to

$$r_p(t) = \left(\frac{3V(t)}{4\pi} \right)^{\frac{1}{3}}, \quad (4.5.5)$$

$$V(t) = V_0 + V_{\text{ice}} = \frac{m_0}{\rho_0} + \frac{(m(t) - m_0)}{\rho_{\text{ice}}}. \quad (4.5.6)$$

m_0 is the initial mass of the nanoparticle with density ρ_0 and ρ_{ice} is the density of the deposited ice.

5. Experimental setup

5.1. The MICE-TRAPS apparatus

The main goal of this study is to investigate the H₂O and CO₂ ice nucleation and growth behavior of meteoric smoke particles (MSP). To this end, I used the MICE-TRAPS setup. The Molecular flow Ice CELL (MICE) within the Trapped Reactive Atmospheric Particle Spectrometer (TRAPS) is a unique device which allows us to study the interaction of charged nanoparticles with a supersaturated vapor. With this setup, conditions similar to the terrestrial mesopause and the mesosphere of Mars become accessible in the laboratory. The experimental setup consists of three main parts: The nanoparticle production unit, TRAPS and MICE (which is an integral part of TRAPS). All three parts have already been described elsewhere [Meinen et al., 2010; Meinen, 2010; Duft et al., 2015; Nachbar et al., 2018b]. The following recalls the main features of these parts for the reader to follow the operating principle used in this work.

5.1.1. The particle source

A non-thermal low pressure microwave-plasma reactor was utilized to generate MSP analogues. This method does not intend to simulate realistic conditions at which MSPs form, but it is able to generate nanoparticles in the same size range and with the same major elements (Fe, Si, Mg, O) as expected for MSPs. Figure 5.1 shows a schematic representation of the nanoparticle source. Organometallic precursors are stored in three individual reservoirs which can be separated from the precursor mixer line via valves. The temperature of each reservoir is individually controlled by a heated/cooled water bath. The number of precursor molecules which is added to a 3 slpm helium flow in the precursor mixer is solely dependent on the vapor pressure of the individual precursor materials. The precursor mixer is heated to 95 °C with heater bands in order to prevent recondensation and recrystallization of precursor molecules on the walls. The mixture of precursor molecules and helium is guided through a narrowing into a quartz glass tube (2.2 cm inner diameter and 40 cm length). The tube is positioned in a microwave resonator operated at 2.45 GHz with a power of 350 W. The 3 slpm gas flow corresponds to a 60 ms residence time of the precursor molecules in the microwave resonator zone. During this time, the microwave radiation induces a plasma by decomposition and further ionization of the precursor molecules. The insert below the resonator sketch in Figure 5.1 shows a photograph of a plasma created in the particle source. A 0.1 slpm flow of oxygen is added before the discharge zone, but downstream

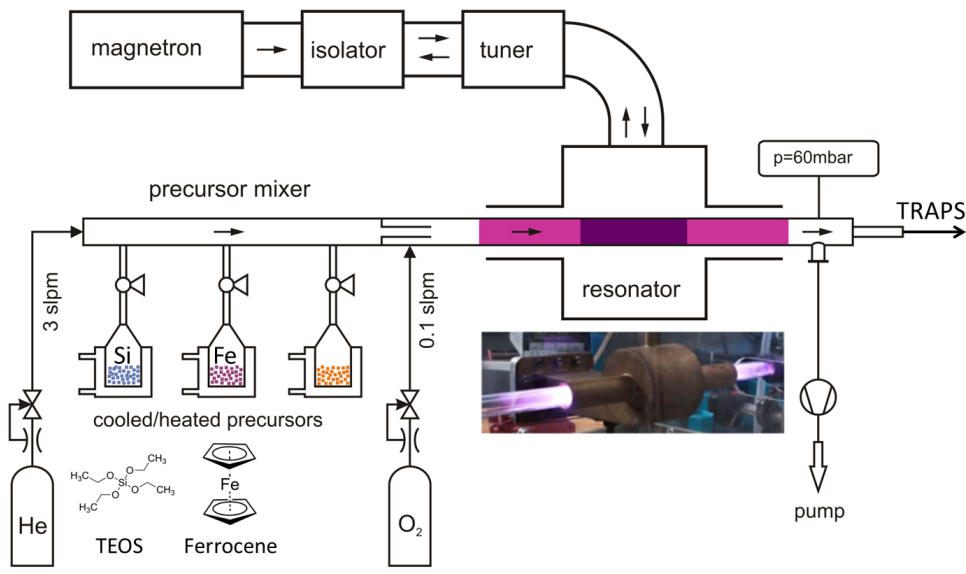


Figure 5.1.: Representation of the nanoparticle source. Adapted from Nachbar et al. [2018b]

of the narrowing to prohibit oxidation of the precursors prior to entering the plasma discharge zone. The decomposed and ionized precursor atoms are oxidized and form nanoparticles with radii between 1 and 4 nm which are either neutral or singly charged (positively and negatively). A pump behind the discharge zone controls the operating pressure at 60 mbar. Less than 20% of the particle laden gas flow is transferred to the vacuum chamber TRAPS, which is introduced in the next section.

In this work, only iron and silicon containing particles were produced since no adequate magnesium precursor could be found. Tetraethyl orthosilicate (TEOS, $\text{Si}(\text{OC}_2\text{H}_5)_4$, Sigma Aldrich) was used as a silicon precursor and ferrocene ($\text{Fe}(\text{C}_5\text{H}_5)_2$, Sigma Aldrich) was used as an iron precursor.

The nucleation ability of particles depends on the particle material. Thus, experiments with particles composed of any kind of potential MSP materials are of desire. The knowledge of the exact composition of the MSP analogues produced with the microwave plasma source is therefore of great importance. I conducted experiments to characterize the particles produced with the microwave plasma resonator, which are presented in Appendix A. In brief, the iron to silicon content of the particles can be controlled solely by adjusting the temperature of the precursor reservoirs. The organic parts of the precursors are sufficiently oxidized to CO_2 and H_2O and no significant amount of carbon is included in the particle material. Iron oxide particles are composed of maghemite (Fe_2O_3 , $\rho = 5.2 \text{ gcm}^{-3}$) and silicon oxide particles are composed of silica (SiO_2 , $\rho = 2.3 \text{ gcm}^{-3}$). Mixed iron silicates are composed of $\text{Fe}_x\text{Si}_{1-x}\text{O}_3$

($0 < x < 1$). Note that particles produced in similar experimental arrangements have shown to be compact and spherical with a high degree of crystallinity [Nadeem et al., 2012; Giesen et al., 2005; Janzen et al., 2002].

5.1.2. The TRAPS apparatus

An overview of the Tapped Reactive Atmospheric Particle Spectrometer (TRAPS) is presented in Figure 5.2. The singly charged MSP analogues produced in the parti-

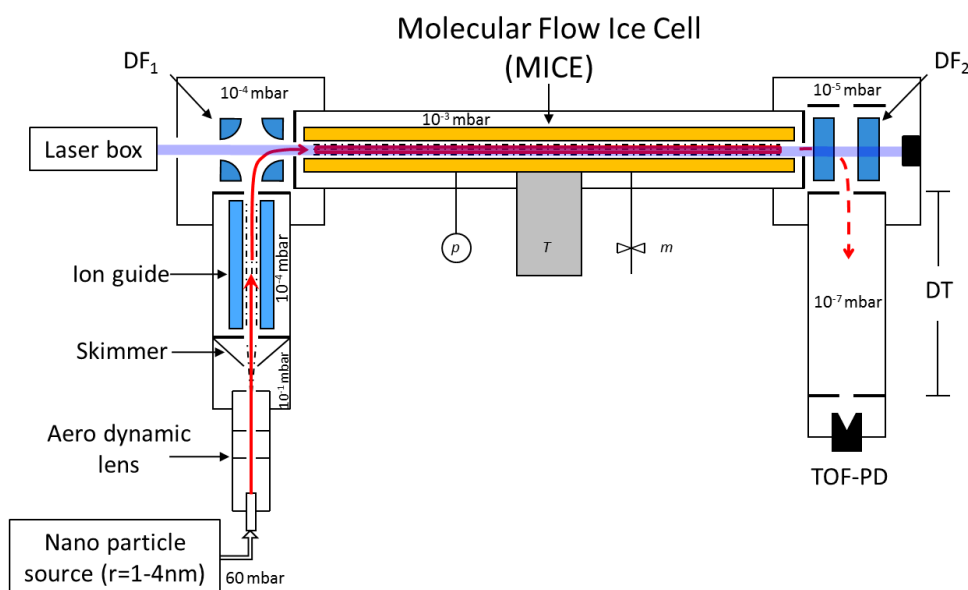


Figure 5.2.: Schematic representation of the Trapped Reactive Atmospheric Particle Spectrometer (TRAPS) including the Molecular flow Ice Cell (MICE).

cle source at 60 mbar are transferred to the vacuum setup TRAPS to a pressure of 5×10^{-1} mbar with an AeroDynamic Lens (ADL). The ADL is designed to transfer particles smaller than 10 nm in radius. It consists of orifices placed at well defined distances. The orifices cause series of contractions and expansions of the gas flow achieving a good transfer efficiency and focusing to less than 3 mm beam width [Meinen et al., 2010; Meinen, 2010]. A skimmer is placed right behind the ADL, which separates the particle transfer unit from the main vacuum chamber and produces another pressure jump to 10^{-4} mbar. Vacuum conditions in the main chamber are guaranteed by two turbo-molecular pumps (1150 ls^{-1} , Oerlikon Turbovac 1000C) supported by a combination of rotary vane and roots pumps. An octopole ion guide (typically operated at 66 kHz and 450 V) is used to guide the charged particle population. Further downstream, a quadrupole deflector (DF₁) deflects particles of a certain polarity and well defined kinetic energy by 90°. Since all particles are accelerated by the ADL to the same velocity [Nachbar, 2014], the separation by kinetic energy corresponds to a sep-

aration by mass and thus particle size.

The size selected particles are levitated in the modified quadrupole ion trap MICE. MICE is typically filled with about 1×10^8 particles for a time period between 1 s and 3 s, which are then stored for up to several hours. During the residence time in MICE, the particles are exposed to H_2O or CO_2 concentrations corresponding to supersaturated conditions. The particle temperature is controlled via thermalization with helium gas which is adjusted in MICE to pressures between 1×10^{-3} mbar and 5×10^{-3} mbar with a leak vent connected to a helium flask. The operation mode of MICE is discussed in detail in the next section. Depending on the conditions in MICE, H_2O or CO_2 adsorption and/or nucleation followed by particle growth can be investigated by analyzing the mass of the particles as a function of residence time in MICE. Small fractions of the particle population levitated in MICE are extracted at periodic residence times and their mass distribution is analyzed with a Time-Of-Flight mass spectrometer (TOF). The TOF is composed of a modified quadrupole deflector (DF_2) used to horizontally decelerate the particles and accelerate them in the vertical plane ($E_{\text{kin}} = 300$ eV), a drift tube (DT) and a particle detector (TOF-PD). The particle mass distribution recorded by the TOF can be fitted reasonably well using a Gaussian curve. The particle mass data is analyzed using the maximum of the recorded mass distribution as the most frequent particle mass (modal value) with the standard deviation (5 % to 7 %) of the Gaussian fit as a 1σ uncertainty interval. At present, the TOF is able to detect only positively charged particles. Note that in Figure 5.2 the TOF is rotated by 90° from the vertical to the horizontal plane. The procedure of guiding, deflecting and trapping particles as well as the operation mode of the TOF is introduced in more detail in my Master's thesis [Nachbar, 2014].

Recently, the TRAPS setup has been extended with a laser box. In brief, the beam profiles of three diode lasers ($\lambda = 405$ nm, $\lambda = 488$ nm and $\lambda = 660$ nm) is expanded by an optical system and enters the vacuum chamber through a quartz glass window. The beam is horizontally directed through the center of MICE pointing onto a beam dump. The particles trapped in MICE are exposed to the laser beam of variable intensity which serves as a simulation of solar irradiation. This setup allows to study the heating of the particles in a low pressure environment representative for the terrestrial mesopause, which is currently ongoing research.

5.1.3. The MICE ion trap

MICE is a combination of a linear ion trap and supersaturation cell operating in the molecular regime. This new and unique type of a supersaturation cell was designed, built and characterized as part of my Master's Thesis [Nachbar, 2014]. The experimental setup and operation mode was introduced to the scientific community in a peer-reviewed publication [Duft et al., 2015]. The operation mode of MICE is discussed in the necessary scientific detail in this section.

An overview of MICE

MICE is a modified 50 cm long linear quadrupole ion trap. A radial cross section of MICE is depicted in panel (a) of Figure 5.3. Panel (b) shows an illustration of MICE excluding the cooling tube (1). The four gold covered copper quadrupole electrodes

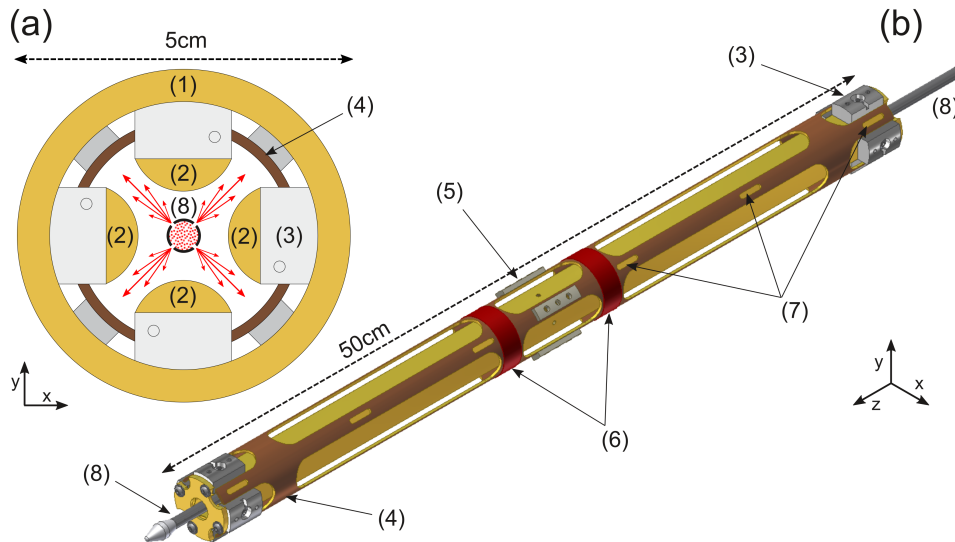


Figure 5.3.: Illustration of MICE. Panel (a) shows the radial cross section of MICE. Panel (b) shows MICE excluding the cooling tube. The labeled parts are: (1) cooling tube, (2) quadrupole electrodes, (3) SHAPALTM spacers, (4) sample surfaces, (5) PEEKTM spacers, (6) Kapton heating foils, (7) temperature sensors, (8) vapor applicator. Figure from [Duft et al. \[2015\]](#).

(2), to which the rf-potentials (100 V - 1000 V at 30 kHz - 100 kHz) are applied, are mounted to the cooling tube (1) with SHAPALTM spacers (3). SHAPAL is an electric insulator with a high thermal conductivity assuring that the electrodes adjust to the same temperature as the cooling tube. The cooling tube is mounted on a helium closed cycle cryostat and its temperature is controlled via resistive heating and temperature recording with two calibrated pt-100 sensors placed at the outer ends of the cooling tube. An additional gold covered copper tube (4) with openings for the quadrupole electrodes is mounted to the cooling tube with PEEKTM spacers (5). PEEK is an electric insulator with a low thermal conductivity. Kapton heating foils (6) are used to heat the additional surfaces, which are called sample surface and which fill the gaps between the quadrupole electrodes. This way, the sample surfaces are heated to an offset temperature with respect to the quadrupole electrodes. The temperature is monitored at six locations (7) along the trap with calibrated pt-100 sensors. At the beginning of each experimental day the vapor applicator (8) is inserted into MICE to deposit CO₂ or H₂O on the electrodes and the sample surfaces. The vapor applicator consists of a stainless steel tube with holes of $d = 100 \mu\text{m}$ at a distance of every

5 mm which all point to the sample surfaces. The tube is connected to a CO₂ flask or an evacuated water reservoir providing gas phase CO₂ or H₂O molecules. This installation results in a deposition rate of 1 nms⁻¹ to 10 nms⁻¹. Vapor deposition is usually conducted for about 10 minutes assuring an ice layer of about one micrometer.

The operation mode of MICE

Figure 5.4 shows a simplified radial cross section of MICE including the ion trap electrodes (1) and the sample surfaces (2). The charged nanoparticles (3) are trapped

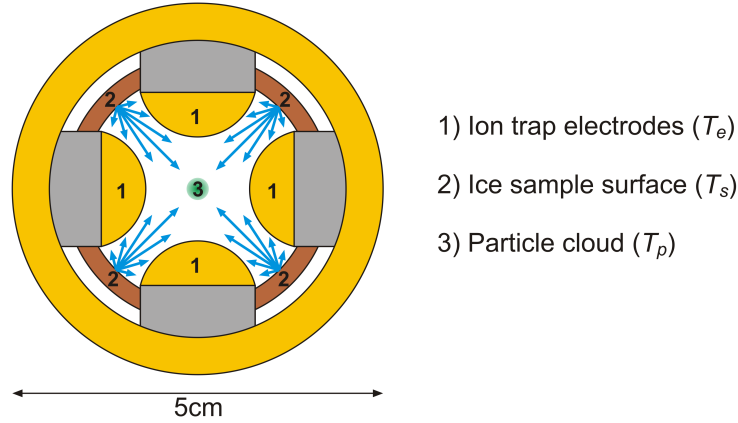


Figure 5.4.: Radial cross section of MICE. Figure from Nachbar et al. [2018a].

in the center between the four quadrupole ion trap electrodes. The H₂O or CO₂ ice covered electrodes and sample surfaces completely surround the levitated particles. Sublimation from these surfaces provides the molecule flux onto the levitated nanoparticles. The ion trap electrodes are held at temperature T_e and the sample surfaces are heated to an offset temperature T_s . The helium pressure in MICE is low enough to ensure a molecular flow of water molecules excluding collisions with helium molecules. The flux density of molecules to the particles is made up of the flux density emitted from the electrodes j_e and the sample surfaces j_s :

$$j_{in} = j_s + j_e = F_s \cdot \frac{p_{sat,s}(T_s) \cdot v_{th,s}}{4kT_s} + (1 - F_s) \cdot \frac{p_{sat,e}(T_e) \cdot v_{th,e}}{4kT_e}. \quad (5.1.1)$$

F_s is the solid angle weighting factor of the sample surfaces as seen from the particle location. Majima et al. [2012] have shown an excellent match of measured particle cloud radii in linear ion traps with theoretical calculations. Using their calculations yields that the particles in MICE are confined within a maximum radius of 1 mm. Assuming the particles to be located within less than 1.5 mm from the radial center of MICE, numerical calculations based on the geometry of MICE yield in $F_s = 0.274 \pm 0.008$. Equation 5.1.1 can be used for the incoming molecule flux in Equation 4.5.2 to describe the particle growth rate as discussed in Chapter 4.5. Note, that the sample surfaces

are always warmer than the electrode surfaces. Consequently, the major number of gas phase molecules in MICE are emitted from the sample surfaces and not from the electrode surfaces as indicated by the blue arrows in Figure 5.4.

The particle temperature T_p equilibrates because of helium atoms colliding with the particle. The particle temperature equilibrates to the mean temperature of the electrode and sample surfaces weighted with the solid angle weighting factor according to

$$T_p = F_s \cdot T_s + (1 - F_s) \cdot T_e. \quad (5.1.2)$$

The saturation at the particle location can be expressed by the ratio of the incoming flux density j_{in} and the sublimation flux density over a planar surface j_{T_p} at particle temperature T_p with

$$S_p = \frac{j_{in}}{j_{T_p}} = \frac{j_{in} \cdot 4kT_p}{p_{sat, p}(T_p) \cdot v_{th, p}}. \quad (5.1.3)$$

Since the saturation vapor pressure is strongly non-linear with temperature, very high supersaturations ($S=1-100\,000$) can theoretically be achieved in MICE.

MICE has shown to trap particles efficiently without detectable particle loss over several hours. The temperature profiles of the surfaces along MICE are highly homogeneous ensuring only small variations of the particle temperature and water vapor concentration in MICE. For all accessible conditions in MICE, no significant influence of the sublimation energy of CO_2 and H_2O during growth conditions are present. Helium operating pressures between 1×10^{-3} mbar and 5×10^{-3} mbar ensure the molecular flow regime of H_2O or CO_2 molecules such that Equation 5.1.1 is valid.

5.2. Relative vapor pressure measurements using an ionization gauge*

MICE-TRAPS is able to measure the saturation vapor pressure of H_2O ice on the sample surfaces between 130 and 160 K. An additional setup was built in order to extend the saturation vapor pressure measurements to temperatures above 160 K. The setup was used to measure the relative vapor pressure difference between ice deposited at temperatures relevant for the terrestrial mesopause and hexagonal ice. The setup and the specific measurement procedure applied in this work are presented in the following.

Experimental setup

A schematic representation of the experimental setup is depicted in Figure 5.5. The setup consists of two interconnected vacuum chambers with a base residual gas pressure below 5×10^{-9} mbar. Upper and lower chamber can be evacuated via independent

*Based on [Nachbar et al., 2018a]

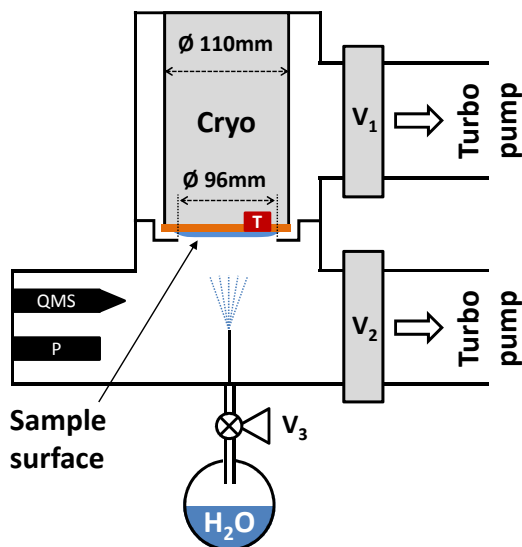


Figure 5.5.: Experimental setup used for the relative saturation vapor pressure measurements between 166 and 190 K. A hot-cathode ionization gauge (P) is employed in a vacuum chamber which is evacuated via valves V_1 and V_2 by two turbo molecular pumps. Simultaneous quadrupole mass spectrometer (QMS) measurements ensure that no other trace gases than H_2O bias the pressure readout. See text for details. Figure from Nachbar et al. [2018a].

valves V_1 and V_2 by two turbo molecular pumps (Leybold Turbovac 350i, $2901s^{-1}$ and Agilent Varian V 300HT, $2501s^{-1}$). A closed cycle Helium cryostat (Advanced Research Systems, DE110 with GMX-20B) is mounted in the upper chamber with the cold sample surface pointing towards the lower chamber. The sample surface is a flat and polished copper disc with a diameter of 110 mm and a Pt-100 temperature sensor attached to the side of the disc. A stepped separator ring is mounted between both chambers with an inner opening of 96 mm and 2 mm distance between ring and cryostat. The ring serves as a barrier for water molecules from the lower to the upper chamber during the experiment. Water vapor is provided from a flask containing NanopureTM water. Prior deposition, the liquid is subject to several freeze-pump-thaw cycles to remove dissolved gases. The water reservoir is connected to the vacuum chamber via the fine dosing valve V_3 and a thin tube such that after opening the valve a deposition rate of about 8 nm s^{-1} on the probe is obtained.

Measurement procedure

Two methods were conducted for depositing water vapor onto the sample surface:

- H_2O was deposited from the vapor phase at temperatures relevant for the terrestrial mesopause, either at 100 or at 150 K resulting in a roughly $15 \mu\text{m}$ thick

ice film. Both chambers were evacuated during deposition.

- To create hexagonal ice, the fine dosing valve was opened to full extend with V_1 and V_2 closed and while cooling the sample surface at a rate of 2 K min^{-1} starting from 277 K. At about 269 K condensation of liquid water droplets could be observed by eye through a glass window mounted on the lower chamber. Sudden freezing of the water droplets was observed at about 260 K. At this temperature only hexagonal ice I_h forms. Valve V_3 (to the water reservoir) was closed immediately after crystallization and the probe temperature was further decreased with about 3 K min^{-1} down to 150 K with V_1 and V_2 being opened at about 210 K.

After ice deposition, the measurement procedure was identical for both deposition methods. The cooling was turned off at 150 K resulting in a slow sample warm-up ($\approx 0.5 \text{ K min}^{-1}$). During warm-up, V_2 was closed to reduce water vapor loss by pumping. The vapor pressure of the deposited ice phase was measured as function of the sample temperature with a hot cathode ionization gauge (P; Oerlikon Leybold Ionivac ITR 90). The ITR 90 is a combined instrument comprised of a Pirani sensor for higher pressures and a Bayard Alpert hot cathode ionization sensor for lower pressures. Below a pressure of 5.5×10^{-3} mbar, below which all measurements presented in this work were performed, only the hot cathode ionization sensor is active. The sensor has a characteristic curve calibrated for N_2 and the pressure measured by the device can be obtained via RS232 interface. The recorded vapor pressure data thus deviate from the vapor pressure above the sample surface by the H_2O calibration curve of the sensor. In addition, in free molecular flow the partial pressure measured in the warm part of the chamber near the gauge (T_w) differs from the partial pressure above the cold ice sample surface (T_c) by a factor $\sqrt{T_c/T_w}$. Simultaneous residual gas measurements with a Quadrupole Mass Spectrometer (QMS; Pfeiffer Prisma Plus QMA-200) ensured that no significant amount of trace gases other than H_2O bias the recorded total pressure readout. However, the data recorded by the QMS were not used to evaluate the water vapor partial pressure as the QMS signal on m/q ratio 18 saturated at a temperature of about 170 K.

During pressure measurements, the temperature of the sample disc was measured with a Pt-100 temperature sensor attached to the side of the disc. A calibration run with 6 additional Si-diode temperature sensors distributed on the sample disk was performed. It was found that during warm-up the sample surface temperature is homogeneous within 0.2 K and the absolute uncertainty of the temperature measurement is less than 0.5 K.

Absolute vapor pressure measurements with the accuracy required to distinguish between different ice phases are difficult to achieve with this setup. However, relative vapor pressure measurements can be obtained when directly comparing the vapor pressure measured for low temperature deposited ices with the results obtained for the

hexagonal ice sample. In this way, many uncertainties and systematic errors occurring in absolute vapor pressure measurements are avoided.

6. H₂O vapor pressure measurements*

This chapter reports on H₂O vapor pressure measurements of ice samples deposited from the gas phase at conditions relevant for cloud formation in the terrestrial mesopause. For this purpose two independent and complementary experimental setups were used. The vapor pressure over ASW and crystalline ice was measured between 130 and 160 K using ice growth rates on MSP analogues levitated in MICE as a sensitive probe. In order to extend the range to temperatures around 190 K an independent more conventional experiment was assembled. This setup was used to measure the relative vapor pressure of water ice samples with respect to hexagonal ice I_h during temperature ramping between 166 and 190 K. The two methods are introduced in Section 6.1. Section 6.2 presents the results of the H₂O saturation vapor pressure measurements of both experimental setups between 130 and 190 K. The vapor pressure data show a significantly increased vapor pressure of crystalline ice and ASW below 160 K relative to hexagonal ice I_h. Section 6.3 compares these results to previously published vapor pressure measurements. It is shown that the elevated vapor pressure of crystalline ice formed below 160 K can be attributed to the influence of nano-grains which form during the crystallization process of ASW. The consequences of this finding on the vapor pressure of ASW are discussed. Additionally, new parameterizations for the vapor pressure of ASW and nano-grained crystalline ice are presented. Section 6.4 summarizes the main findings of this chapter and responds to the first question formulated in the introduction:

What is the predominant ice phase involved in PMC formation?

6.1. Methods

6.1.1. Measurements using MICE-TRAPS

At the beginning of each experiment, H₂O ice was deposited at temperature between 90 and 160 K on the electrodes and sample surfaces in MICE as discussed in the previous chapter. After deposition, the ice-covered electrodes and additional surfaces were set to the desired temperatures. Subsequently, silica or maghemite particles were trapped in MICE and exposed to the flow of water molecules originating from the temperature controlled surfaces in MICE. The particle growth was monitored as function of time by periodically extracting small fractions of the trapped particle population from MICE and directly measuring the particle mass using the TOF mass spectrometer. The

* In part based on [Nachbar et al., 2018a]

growth rate (Equation 4.5.2) is the difference between incoming flux impinging on the particles and outgoing flux and can be used as a sensitive probe for the sublimation rates and thus the vapor pressures over the ice covered sample surfaces in MICE and the ice phase deposited on the particles.

Vapor pressure measurements of the ice phase on the sample surfaces ($S > 1000$)

The vapor pressure above the ice phase on the sample surfaces in MICE was determined by applying a saturation in excess of $S=1000$. These high saturations exceed by far the critical saturation for ice nucleation. Consequently, the particles nucleate ice and grow. The growth rate of the ice particles (Equation 4.5.2) is described by the difference between the incoming H₂O flux density onto the particles j_{in} and the outgoing flux density j_{out} . For $S > 1000$, sublimation from the particle surface can be neglected. The ice particle growth at such conditions depends solely on j_{in} , which is given by the sublimation from the electrodes j_e and the sample surfaces j_s in MICE (Equation 5.1.1). The high supersaturations were achieved by setting a temperature difference of 20 K or more between the sample surfaces and the cold electrodes. The high temperature difference between the cold electrodes and the warm sample surfaces has the beneficial effect that sublimation from the cold electrodes (j_e) is at least 10^3 times less than from the warmer sample surfaces j_s and can be neglected. Accordingly, the sublimation rate of H₂O molecules from the warm sample surfaces held at T_s determines the ice particle growth rate. The ice on these surfaces constitutes the sample of interest, which for each measurement was kept at a constant temperature between 130 and 160 K. The upper panel of Figure 6.1 shows the measured particle mass as a function of trapping time in MICE for three typical measurements with sample-surface temperatures of 147.4 K, 149.7 K (particle material: Fe₂O₃) and 154.8 K (particle material: SiO₂). The results in terms of particle radii (Equation 4.5.5) are shown in the lower panel of Figure 6.1. The saturation pressure over the sample surfaces $p_{sat,s}$ was numerically fitted to the data. Here, Equation 5.1.1 was used for j_{in} in Equation 4.5.2, where j_{out} and j_e were neglected based on the arguments provided above. The results of the fitting procedure are represented by the green, blue and red curves. For comparison, the results of model runs assuming the vapor pressure of hexagonal ice are shown by the dashed lines. Accordingly, the vapor pressure of the sample ice phase is significantly higher than expected for hexagonal ice.

Vapor pressure measurements of the ice phase on the particles ($S < 60$).

Once the H₂O vapor pressure above the ice phase deposited on the surfaces in MICE is determined, the H₂O flux density impinging on the particles j_{in} is known for a set of electrode and sample surface temperatures (Equation 5.1.1). At a saturation below $S=60$, the outgoing flux density j_{out} (Equation 4.5.3) is lower than the incoming flux density but still contributes significantly to the growth rate of the ice particles. At such low saturations, the saturation vapor pressure above the ice phase deposited on

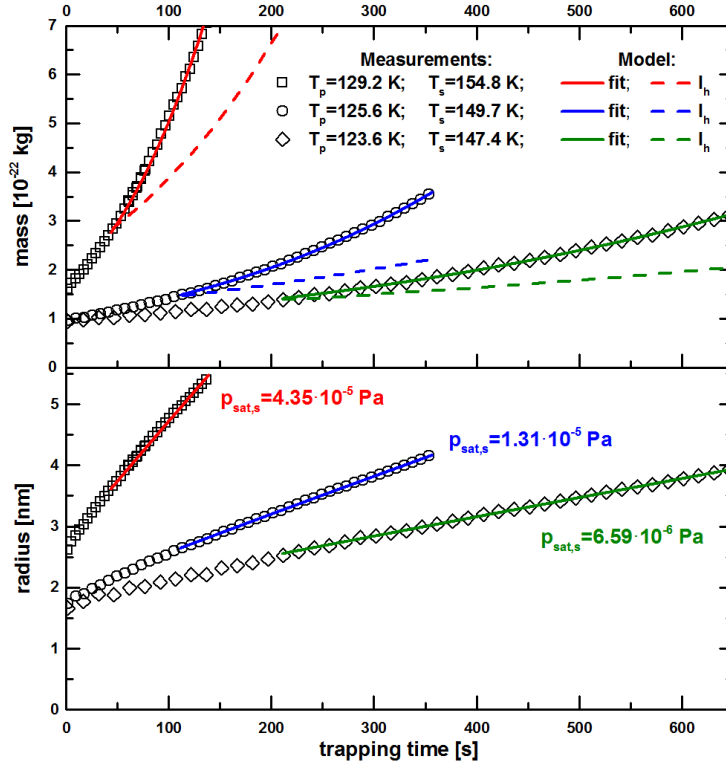


Figure 6.1.: Particle mass (upper panel) and radius (lower panel) as a function of trapping time in MICE for three typical measurements with sample surface temperatures T_s of 147.4 K (open diamonds), 149.7 K (open circles) and 154.8 K (open squares). The particle temperatures T_p are between 123 and 130 K assuming saturations above 1000. The green, blue and red curves show the results of numerically fitting $p_{\text{sat},s}$ to the data. The dashed colored lines show expected growth curves when assuming hexagonal ice I_h . Figure from Nachbar et al. [2018a].

the surface of the particles can be evaluated by numerically fitting Equation 4.5.2 to the ice growth data. Figure 6.2 shows the measured particle mass as a function of trapping time in MICE for two measurements on silica particles with particle temperatures of 139 K (blue open triangles) and 147 K (black open squares). The saturations with respect to ice I_h are 33 and 20. The green dashed curves show the results of model runs assuming deposition of ice I_h on the particles. The measured growth rate of the particles significantly deviates from the model runs assuming ice I_h . Since the particles grow slower compared to the model runs assuming ice I_h and since the incoming H_2O flux is known, the outgoing flux must be higher than for ice I_h . A possible explanation for this behavior is that ASW is growing on the particles and not ice I_h .

The surface tension is an important parameter describing the equilibrium saturation S_{eq} over the curved surface of the ice particle and thus the outgoing H_2O flux. No measurements of the surface tension of ASW are available to date. However, mea-

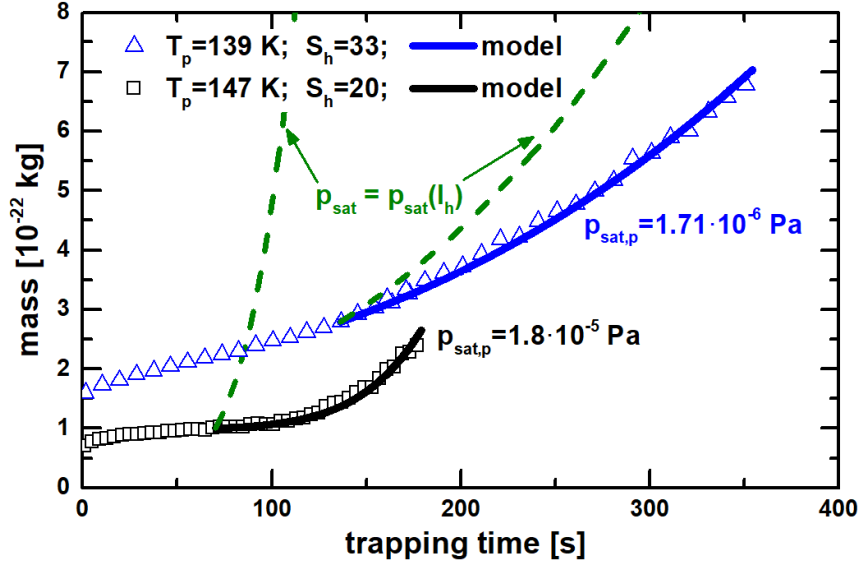


Figure 6.2.: Particle mass as a function of trapping time in MICE at low supersaturations for two exemplary measurements on silica particles with particle temperatures T_p of 139 K (open blue triangles, $S_h = 33$) and 147 K (open black squares, $S_h = 20$). The green dashed curves show the model runs assuming ice I_h on the particles. The blue and black curves show results of numerically fitting $p_{\text{sat},p}$ to the data assuming the surface tension of ASW.

measurements of supercooled liquid water (SLW) exist down to -26°C . By making the assumption that SLW is either the same phase as ASW, or that at least their properties are very similar, permits to extrapolate the surface tension of SLW to colder temperatures. Recent high quality measurements of the surface tension of SLW have shown that the surface tension increases linearly with decreasing temperature down to -26°C [Vins et al., 2015, 2017]. In this work a linear fit to the data of Vins et al. [2015] was used to describe the surface tension of ASW considering an uncertainty of 10%. Additional justification of that choice is provided later in the discussion of this chapter. The parameterization for the surface tension of ASW is given in Table B.1. Using the surface tension of ASW, the saturation vapor pressure of the ice phase deposited on the particles was fitted to the data. The fitted growth curves are shown by the blue and black curves.

Discussion of uncertainties

The densities of ASW and hexagonal ice are very similar for particle temperatures under investigation so that the nature of the deposited phase does not enter in the calculation of the particle size [Brown et al., 1996; Loerting et al., 2011]. Fit uncertainties of $p_{\text{sat},s}$ and $p_{\text{sat},p}$ were typically on the order of 1%. The data were only evaluated after the particles gained at least 3 monolayers for $p_{\text{sat},s}$ and 2 monolayers for $p_{\text{sat},p}$ to

avoid a possible influence of the particle material on the sublimation rate. The results are indeed independent of the type and initial radius (1.6 nm – 3 nm) of the particles under investigation. In addition, the single elementary charge of the particles has no significant influence on the growth curves for the ice particle sizes analyzed (2.5 nm - 6 nm). Using one fit parameter only ($p_{\text{sat},s}$ or $p_{\text{sat},p}$), the implemented growth model very well represents the particle growth data for all temperatures.

Here, only spherical nuclei and ice particles were considered. However, light scattering models showed better agreement to Polar Mesospheric Cloud (PMC) data retrieved by satellite and LIDAR remote sensing instruments when analyzed under the assumption of aspherical ice particle shapes [Eremenko et al., 2005; Hervig et al., 2012; Kiliani et al., 2015; Hervig and Gordley, 2010]. As assumed above and evidenced in the discussion below, water is deposited as ASW onto the ice particles (below $T_p = 150$ K), which makes aspherical particle growth unlikely. In addition, the growth model fit assuming a constant aspect ratio is in very good agreement with the measured data excluding a need of an increasing aspect ratio. Based on the finding that metal oxide nanoparticles produced in similar arrangements were shown to be compact and spherical [Giesen et al., 2005; Janzen et al., 2002; Nadeem et al., 2012], the maximum relative uncertainty in $p_{\text{sat},s}$ and $p_{\text{sat},p}$ due to asphericity of the ice particles is estimated to 5%. The main uncertainty in $p_{\text{sat},s}$ is due to the uncertainty in T_s (0.2 K - 0.4 K). The main uncertainty in $p_{\text{sat},p}$ is due to the uncertainty in T_p (≈ 0.25 K), σ (10%) and the gas phase molecule concentration n_{molec} /incoming flux j_{in} (approximately 10%).

Verification of the method using CO₂

CO₂ is known to be present in only one crystalline state at temperatures above 50 K [Souda, 2006]. In addition, the vapor pressure of crystalline CO₂ ice is well constrained. Thus, vapor pressure measurements of CO₂ ice with MICE-TRAPS serve as a verification of the experimental method. In the case of CO₂, ice growth on the particles was activated for $S > 1000$ so that measurements at low saturations were not feasible. However, measurements at high saturations determining the vapor pressure of the CO₂ ice phase on the sample surfaces were possible.

At the beginning of each experiment, CO₂ ice was deposited at 90 K on the surfaces in MICE. After ice deposition was completed, the electrodes and the sample surfaces in MICE were set to the desired temperatures. Isothermal CO₂ saturation vapor pressure measurements of the ice phase deposited on the sample surfaces in MICE were performed. The saturation in all experiments was larger than $S = 5000$. The measurements were performed in the temperature range between 80 and 86 K. The results are shown by the black squares in Figure 6.3 together with data from the literature. Meyers and Van Dusen [1933] used vapor pressure measurements above 90 K from different studies and parameterized the vapor pressure as a function of temperature T in Kelvin:

$$p_{\text{sat}}(T) = 101300 \cdot 10^{6.92804 - [1347 - 1.167(T^2 - 35450)]^3 \cdot 10^{-12}} \cdot T^{-1} \quad [\text{Pa}]. \quad (6.1.1)$$

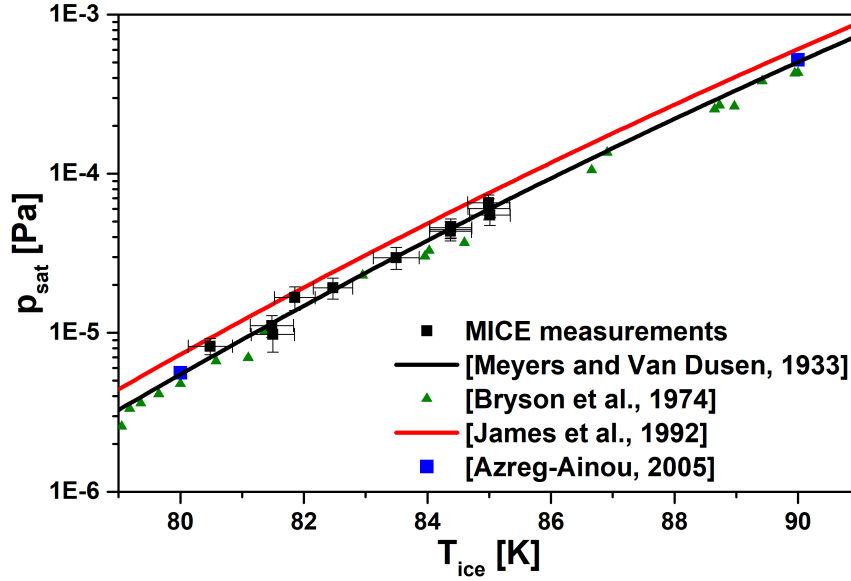


Figure 6.3.: Measured CO₂ saturation vapor pressure as a function of temperature (black squares). For comparison, the measurements by Bryson et al. [1974], the model results from Azreg-Ainou [2005] as well as the parameterizations from James et al. [1992] and Meyers and Van Dusen [1933] are shown.

This parameterization is shown by the black curve in Figure 6.3. It is a good match to the measurements of this work. Bryson et al. [1974] measured the temperature dependent desorption rate of CO₂ with a quartz crystal microbalance. The results are presented by the green triangles. Azreg-Ainou [2005] used heat capacity data above 12.5 K in a numerical thermodynamic model to evaluate for the vapor pressure of CO₂ ice. Unfortunately, Azreg-Ainou [2005] only presents the results of the numerical model in 5 K steps without a simple analytical expression for the vapor pressure. The model results are shown by the blue squares and are in excellent agreement with the parameterization of Meyers and Van Dusen [1933]. A parameterization for the CO₂ vapor pressure proposed by James et al. [1992] is presented by the red curve.

The good match between the MICE-TRAPS data and literature data serves as a proof of the excellent functioning of the experimental technique and data analysis method of the MICE-TRAPS experiments.

The Martian atmospheric science community mostly uses two parameterizations for the vapor pressure of CO₂, (1) either the parameterization of Meyers and Van Dusen [1933] ([e.g. Stevens et al., 2017]) or (2) the parameterization of James et al. [1992] ([e.g. Listowski et al., 2013, 2014]). Both parameterizations are a good match above 120 K and agree with the model of Azreg-Ainou [2005]. Below 120 K, however, the parameterization of James et al. [1992] exhibits higher vapor pressures compared to the MICE-TRAPS measurements and other literature data. At these temperatures, the parameterization of Meyers and Van Dusen (Equation 6.1.1) should be used.

6.1.2. Relative measurements with an ionization gauge

In order to extend the saturation vapor pressure measurements of H_2O to temperatures above 160 K, an additional experimental setup was used with which the relative vapor pressure difference of metastable crystalline ice and ice I_h was measured. The setup is introduced in detail in Chapter 5.2. In this setup, crystalline ice was produced with the same procedure as with the MICE-TRAPS setup, either via deposition of ASW at 100 K followed by crystallization during warm-up or by direct deposition at 150 K. As a reference sample, hexagonal ice was produced by condensation of liquid water on the target at about 270 K and subsequent freezing of the liquid water at about 260 K. Following ice formation, the sample temperature was set to 150 K at which point cooling was turned off resulting in a slow warm-up ($\approx 0.5 \text{ K min}^{-1}$). The vapor pressure in the chamber was recorded as function of the sample temperature using a hot-cathode ionization gauge. The measured H_2O vapor pressures are shown in Figure 6.4. In total seven measurements were performed, four times after deposition at 100

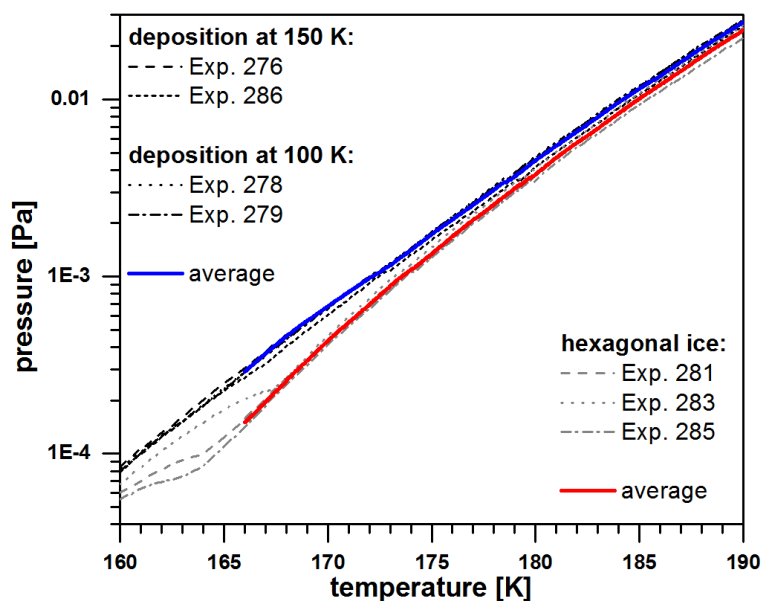


Figure 6.4.: Vapor pressure between 160 and 190 K after deposition at 100 and 150 K (black lines, 4 runs) and after crystallization of hexagonal ice from liquid water at 260 K (gray lines, 3 runs). The solid blue and red lines represent calculated mean vapor pressures for deposition at 100 K / 150 K and hexagonal ice, respectively. Figure from Nachbar et al. [2018a].

or 150 K (black lines) and three times after deposition of hexagonal ice (gray lines). All four measurements of water ice deposited at 150 or 100 K are in agreement, i.e. crystalline ice deposited at 150 K exhibits the same vapor pressure as ice crystallized after deposition of ASW at 100 K. This indicates that at these temperatures all four samples consist of the same ice polymorph (independent of deposition temperature).

For hexagonal ice all curves fall onto each other above 168 K. Below 168 K, the three measurements of hexagonal ice deviate, which can be explained by the following reasoning. During cool-down residual water desorbs from the inner walls of the vacuum chamber and deposits onto the hexagonal ice film. Thus, a layer of the same ice that is created when depositing water directly at 150 K forms. After some time of pumping and sample temperature increase, the residual water source is depleted and the layer on top of the hexagonal ice film begins to evaporate. Eventually, the over-layer completely evaporates and exposes the hexagonal ice below. The transition from the over-layer to the next layer of hexagonal ice is nicely seen for all three experiments. Therefore, the analysis of the data is restricted to temperatures above 166 K. Above 190 K all ice was evaporated rapidly which limits the data to temperatures between 166 and 190 K. Absolute vapor pressure measurements with the accuracy required to distinguish between different ice phases at such low temperatures are difficult to achieve with this setup. However, the vapor pressure of ices deposited below 160 K can directly be compared with the experiments for hexagonal ice, the latter being based on the accuracy of the well-established parameterization by [Murphy and Koop \[2005\]](#). In this way, many uncertainties and systematic errors occurring in absolute vapor pressure measurements are avoided.

The mean and standard deviation were calculated for all runs of low temperature vapor deposited ice between 166 and 190 K (blue curve). For hexagonal ice, the experiments 281 and 285 were used between 166 and 169 K and all three runs above 169 K (red curve). The recorded vapor pressures were highly reproducible and the ratio of the vapor pressures of the two ice phases was determined with an accuracy of 10 %.

6.2. Results

MICE experiments for $S > 1000$

Isothermal saturation vapor pressure measurements of the ice phase deposited on the sample surfaces in MICE were performed in the temperature range between 130 and 160 K for saturations above $S=1000$. The results are shown in Figure 6.5 relative to the saturation vapor pressure of hexagonal ice $p_{\text{sat}}^{\text{h}}$ (Equation 2.4.4 [[Murphy and Koop, 2005](#)]). The parameterization of [Murphy and Koop \[2005\]](#) is expected to be accurate within 1% for all investigated temperatures. At the beginning of each MICE-TRAPS experiment, water ice films were deposited on the surfaces in MICE either at 95, 140 or 160 K. After ice deposition was completed, the electrodes and sample surfaces in MICE were set to the desired temperatures and isothermal measurements were carried out (see Section 6.1.1). The results are presented in Figure 6.5. Temperature error bars are of the same size as the data points ($\Delta T = 0.2 \text{ K} - 0.4 \text{ K}$). The filled blue diamonds show the results of a series of six measurements performed using a single ASW film deposited at 95 K with the arrow indicating the chronology. The series started at 133.4 K with the freshly deposited film followed by a repeated sequence of setting the desired sample temperature, 20 minutes of thermalization, and the measurement of

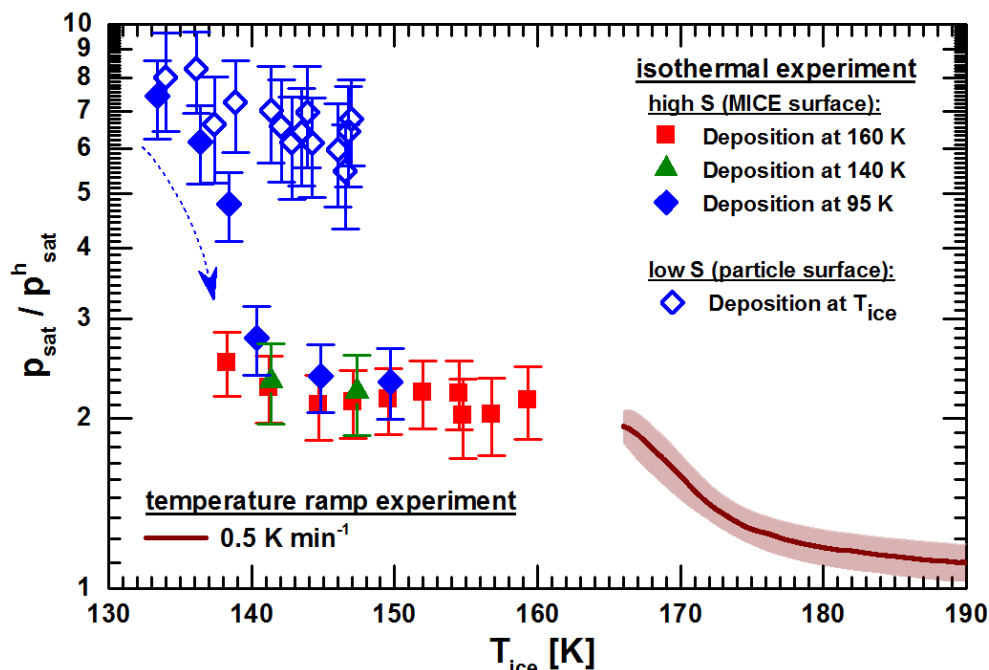


Figure 6.5.: Measured relative saturation vapor pressure of low temperature deposited ices with respect to ice I_h as a function of temperature. Green triangles and red squares denote isothermal vapor pressure measurements at high saturations of ice samples deposited at 140 and 160 K, respectively. Filled blue diamonds represent a series of subsequent isothermal measurements using a single ice film deposited at 95 K with the arrow indicating the chronology. Open blue diamonds show the isothermal vapor pressure measurements of the ice phase deposited on the particles obtained at low saturations. The brown line is the combined experimental result for the non-isothermal relative vapor pressure measurements of all ices deposited below 150 K (the shaded area indicates the uncertainty).

particle growth at a constant temperature. For this set of measurements, the relative vapor pressure strongly decreases between 133 and 140 K (the first 4 data points). The vapor pressure levels off to the saturation vapor pressure obtained for the samples deposited at 140 and 160 K (green triangles and red squares, respectively). This behavior is typical for a thermally activated crystallization process. Crystallization constants τ (the time to achieve a 63% crystallization) of amorphous ice samples reported in the literature vary by several orders of magnitude [e.g. Dowell and Rinfret, 1960; Sack and Baragiola, 1993; Smith et al., 1996, 2011; Mitchell et al., 2017]. Mitchell et al. [2017] have shown that the discrepancy in the reported crystallization constants is likely to be caused by ice samples of different porosity. Higher porosities result in smaller crystallization constants (higher crystallization rates). From the vapor pressure data the crystallization constant is estimated to about 25 minutes at 140 K, which is in agreement with measurements of a probably non-porous ASW sample reported by Smith et al. [2011]. Using the parameterization for the temperature dependent crystallization

rate from [Smith et al. \[2011\]](#), the fraction of amorphous ice can be estimated to be larger than 90 % during the first measurement.

Above 140 K, the saturation vapor pressure is independent of the deposition temperature, suggesting that ice deposited between 140 and 160 K forms the same ice polymorph as those crystallized from ASW. Between 130 and 160 K the vapor pressure of this ice polymorph is enhanced by a factor between 2 and 3 with respect to hexagonal ice I_h.

MICE experiments for $S < 60$

Isothermal saturation vapor pressure measurements of the ice phase deposited on the particle surfaces were performed in the temperature range between 134 and 150 K for $S < 60$. To perform these measurements, the saturation vapor pressure of the ice phase on the surfaces in MICE had to be known in order to describe the water molecule flow onto the particles (Equation 5.1.1). Here, the parameterization for crystalline ice was used as inferred from the measurements at high saturations (next section, Equation 6.3.2). The resulting saturation vapor pressure of the ice phase deposited on the particles is shown in Figure 6.5 (open blue diamonds). The indicated temperature T_{ice} applies for the temperature at ice deposition and the measurements. The results show a vapor pressure of the ice phase deposited on the particles which is significantly higher than the vapor pressure of the crystalline samples on the sample surfaces in MICE.

As shown in the previous paragraph, the first measurement at 133 K of the series for high saturation after deposition of ASW is an almost completely amorphous sample. For this ice, the measured vapor pressure does not assume anything regarding the surface tension of ASW and agrees with the results of the vapor pressure measurements above the ice phase deposited on the particles. Consequently, the ice phase deposited on the particles is indeed ASW and the parameterization used for the surface tension of ASW is valid within the estimated uncertainty limits.

Crystallization of ASW is not observed in these measurements. This is since fresh layers of ASW are deposited on the particles during growth. In addition, the duration for a complete measurement run was well below the crystallization constant at the respective temperatures. The results show that between 130 and 150 K the vapor pressure of ASW is increased by a factor between 5 and 10 with respect to hexagonal ice I_h.

Temperature ramping experiments with an ionization gauge

Measurements using the hot ionization gauge setup were performed with a temperature ramp of 0.5 K min^{-1} between 166 and 190 K. As reported above for the MICE experiment, ice crystallized from ASW after deposition at 100 K and ice deposited at 150 K do not show any significant difference in the vapor pressure. The average of the relative vapor pressures obtained for all runs performed with the hot ionization gauge

setup is shown in Figure 6.5 (brown line with the shaded area indicating one standard deviation). Above 180 K, the vapor pressure of this ice is only slightly above that of hexagonal ice I_h . At lower temperatures the measured normalized vapor pressure of the crystalline ice phase increases and connects well to the vapor pressure measured with the MICE-TRAPS setup at 160 K.

6.3. Discussion

6.3.1. Comparison to literature data

Chapter 2.4 reviews and partially re-analyzes the limited number of available literature data on vapor pressure and desorption rate measurements of ASW and metastable crystalline ice below 175 K. The available data shows large discrepancies. Figure 6.6 shows the most reliable literature data normalized to hexagonal ice I_h . Additionally, the

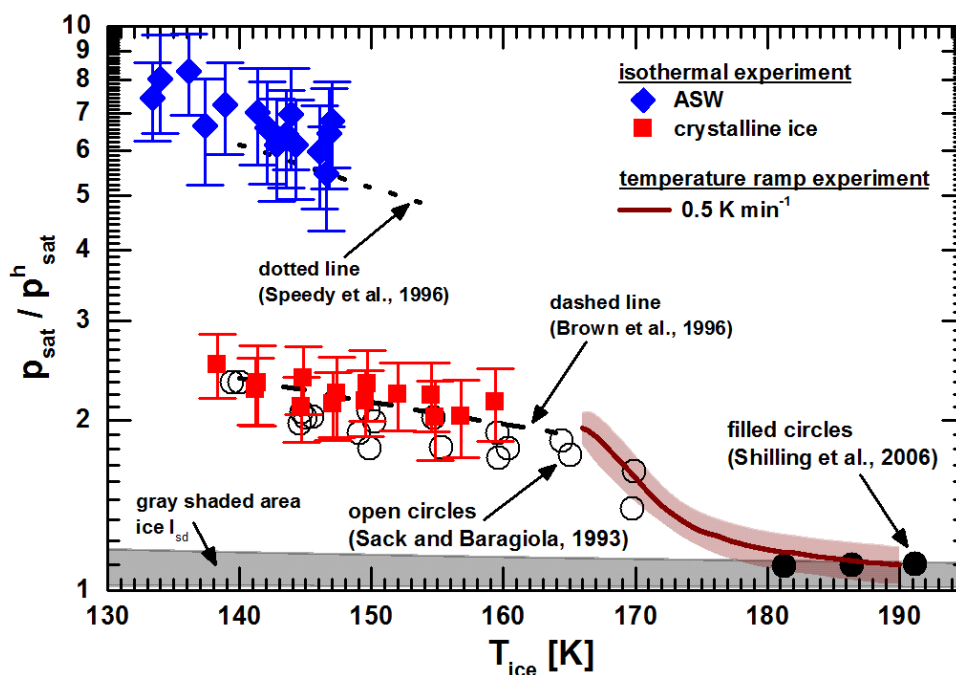


Figure 6.6.: Measured relative saturation vapor pressure of low temperature deposited ices with respect to ice I_h as a function of temperature. Blue diamonds denote the combined MICE-TRAPS results for ASW and red squares for crystalline ice. The brown line is the result for crystalline ice obtained with the temperature ramp experiment (including a shaded interval of uncertainty). For comparison, selected data for ASW and crystalline ice from the literature are shown. The gray shaded area represents a parameterization for ice I_{sd} .

results of the vapor pressure measurements of the present thesis are shown. The results for ASW deposited on the particle surfaces including the almost completely amorphous

ice sample on the sample surfaces in MICE are shown by the blue diamonds. They are in good agreement with the results for ASW from Speedy et al. [1996] (black dotted curve).

All ice samples after crystallization from ASW and after deposition at 140 and 160 K obtained at high saturations with MICE-TRAPS are shown by the red squares. The temperature ramp experiments are shown by the brown line with the shaded area indicating the uncertainty. All measurements agree well with the data from literature for crystalline ice reported by Sack and Baragiola [1993] (black circles), Brown et al. [1996] (black dashed curve) and Shilling et al. [2006] (filled black dots).

Stacking disorder ice I_{sd} is assumed to be the prevailing crystalline ice polymorph below 190 K. The gray shaded area shows a parameterization for ice I_{sd} based on a free energy difference $\Delta G_{sd \rightarrow h}$ with respect to ice I_h between 20 Jmol⁻¹ and 180 Jmol⁻¹ [e.g. Handa et al., 1986; Mayer and Hallbrucker, 1987; Mc Millan and Los, 1965; Sugisaki et al., 1968]. The data from Shilling et al. [2006] and the data of this work above 180 K are in agreement with this parameterization for stacking disordered ice I_{sd}. Below 175 K, however, the relative vapor pressure data for crystalline ice from this work and the literature are significantly higher than the parameterization for ice I_{sd}. The following shows that the observed elevated vapor pressure of crystalline ice below 175 K can be attributed to nano-scale grains formed during the crystallization process of ASW.

6.3.2. The effect of nano-crystals on the vapor pressure

It is well-known that the crystallization process of ASW below 166 K forms nano-crystalline ice [Arnold et al., 1968; Backus and Bonn, 2004; Dowell and Rinfret, 1960; Jenniskens and Blake, 1996; Kondo et al., 2007; Kuhs et al., 1987; Kumai, 1968]. The formation of nano-crystals occurs by nucleation of ice embryos followed by isotropic 3-dimensional diffusional growth within the remaining ASW matrix until all amorphous water is transformed to crystalline ice. At low temperatures, the interplay of ice nucleation and ice growth leads to nanoscale crystals [e.g. Backus and Bonn, 2004; Kondo et al., 2007]. A nano-crystal exhibits a large surface energy to volume energy ratio resulting in an increased vapor pressure above its surface. This vapor pressure increase is described by the Kelvin equation (Equation 4.1.3). It describes the vapor pressure increase over a curved surface with respect to a planar surface which at the same time corresponds to the vapor pressure increase over a macroscopic surface composed of spherical nano-grains with diameter d_{grain} . Rearranging Equation 4.1.3 yields in:

$$\ln \left(\frac{p_{\text{sat}}^{\text{nano}}}{p_{\text{sat}}^{\text{cryst}}} \right) = \frac{4 \cdot \nu \cdot \sigma}{k \cdot T \cdot d_{\text{grain}}}. \quad (6.3.1)$$

Here, k is the Boltzmann constant, T is the temperature, ν is the molecular volume, σ is the ice-vapor surface tension, and $p_{\text{sat}}^{\text{cryst}}$ is the bulk saturation vapor pressure of the crystalline ice. The crystalline nano-grains are most likely composed of ice I_{sd} as supported by model studies [Lupi et al., 2017] and x-ray diffraction experiments [Mor-

ishige et al., 2009]. Since the surface tension of hexagonal and cubic ice must be very similar, it was assumed that the surface tension parametrization of hexagonal ice [Hale and Plummer, 1974] applies for ice I_{sd} with an uncertainty of 10%. Using Equation 2.4.2, p_{sat}^{sd} was calculated with a free energy difference of ice I_{sd} to ice I_h of 20 Jmol^{-1} to 180 Jmol^{-1} . The grain diameters needed to explain the observed elevated vapor pressure of crystalline ice found in this work were calculated from Equation 6.3.1 using p_{sat}^{sd} for p_{sat}^{cryst} . Figure 6.7 shows the grain diameters calculated from the MICE-TRAPS vapor pressure data (black squares) and from the the temperature ramp experiment (brown line, with the shaded area indicating the uncertainty). Below 160 K, estimated

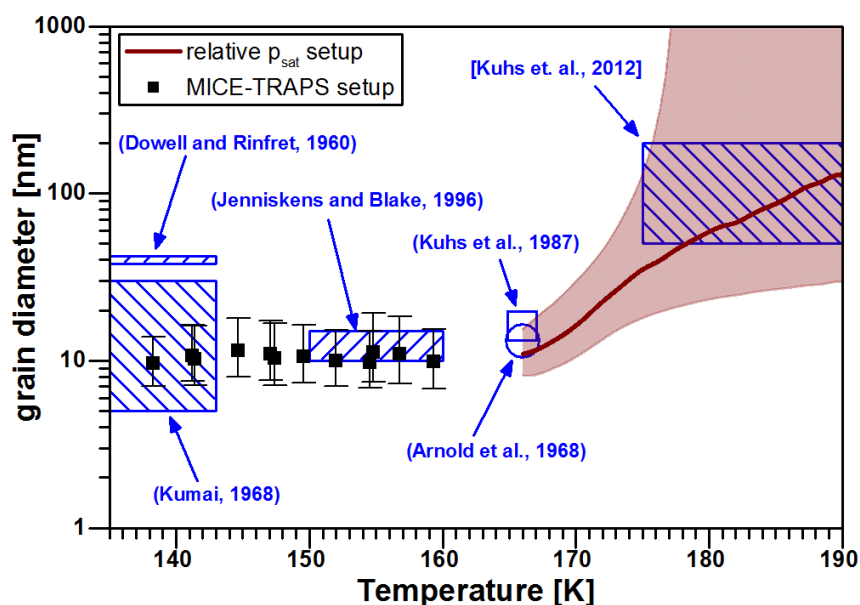


Figure 6.7.: Calculated nano-crystallite diameters as a function of temperature. The black squares represent the results of the MICE-TRAPS measurements and the brown curve with shaded confidence interval the results of the relative vapor pressure measurements. The results are compared to crystal diameters reported in the literature (the circle, the square, and the blue shaded areas). Figure from Nachbar et al. [2018a].

grain size diameters are in the range between 7 and 19 nm. Here, the crystal size does not depend on the formation temperature and remains constant over a typical measurement period of 10 hours. Small grain sizes like this were previously observed after crystallization of vapor-deposited ASW. Using electron diffraction, Jenniskens and Blake [1996] observed crystal diameters of 10 nm to 15 nm between 150 K and 160 K and Kumai [1968] reported diameters of 5 nm to 30 nm at 113 K to 143 K. Dowell and Rinfret [1960] used X-ray diffraction and observed grain sizes of about 40 nm. The crystallization process of deuterated water from the high pressure ice phases II, IV, V and IX was also examined by neutron powder diffraction. Kuhs et al. [1987] observed mean particle diameters of 16 nm and Arnold et al. [1968] reported mean crystal sizes

of 13 nm. The reported crystal grain diameters are indicated in Figure 6.7 by the blue areas, the circle and the square. These measurements (except for [Dowell and Rinfret, 1960]) agree well with the grain diameters inferred in the present study.

The non-isothermal relative vapor pressure measurements suggest that above 165 K, crystal growth is effectively activated by sublimation and re-condensation at the crystal surface or by local water molecule migration across grain boundaries. Crystal growth is then accompanied by a decrease in the $p_{\text{sat}}/p_{\text{sat}}^h$ ratio. This conclusion is supported by a study of Hansen and co-workers who measured the grain sizes of deuterated ice with neutron powder diffraction and small angle neutron scattering as function of temperature [Hansen et al., 2008]. They reported mean crystal diameters between 20 nm and 25 nm. The crystal sizes were stable for hours up to temperatures of about 160 K followed by crystal growth at higher temperatures. At temperatures between 175 and 190 K, Kuhs et al. [2012] observed crystal sizes between 50 and 200 nm using SEM imaging and neutron diffraction. The crystal sizes increased with temperature and match the diameters calculated from the results obtained with the hot ionization gauge setup.

Since H₂O deposition between 140 and 160 K as well as crystallization of ASW deposited at 95 and 100 K lead to the same nano-crystallite sizes, it is very likely that ice deposition up to 160 K proceeds by an initial deposition of ASW followed by rapid crystallization to nano-crystalline ice. The vapor pressure measurements above the ice deposited on the particles up to 150 K confirm this conclusion. Additional support is provided by the work of Chonde et al. [2006]. They deposited ice at 140 K with deposition rates comparable to this work and observed non-porous ASW immediately after deposition.

Stacking disorder in ice I_{sd} is expected to contribute to the free energy difference $\Delta G_{\text{sd} \rightarrow h}$ with less than 10 Jmol⁻¹ [Hondo et al., 1983; Hudait et al., 2016]. The energy contribution of stacking disorder therefore is not high enough to explain the scatter in measured Gibbs free energy differences $\Delta G_{\text{sd} \rightarrow h}$ of 20 Jmol⁻¹ to 180 Jmol⁻¹ of ice I_{sd} at temperatures above 180 K. Defects beyond stacking faults are proposed to explain the observed energy difference of up to 180 Jmol⁻¹ [Hudait et al., 2016]. However, it is unlikely that defects can make up for an energy difference of 1000 Jmol⁻¹ as observed below 160 K in the present study. It is therefore likely, that an increase of defects beyond stacking faults below 180 K is not the major process causing the observed high vapor pressure. In order to calculate crystal diameters, it was assumed that the crystallites are composed of ice I_{sd} and that this ice polymorph is described by a temperature independent Gibbs free energy difference $\Delta G_{\text{sd} \rightarrow h}$ of 20 Jmol⁻¹ to 180 Jmol⁻¹. An increase of defects beyond stacking faults in the ice I_{sd} polymorph with decreasing temperature might still cause a small increase in $\Delta G_{\text{sd} \rightarrow h}$, which would lead to a change in calculated crystallite sizes. However, the vapor pressure measurements below 160 K were used to calculate the Gibbs free energy difference of the nano-crystalline ice with respect to ice I_h. The resulting Gibbs free energy turned out to be a constant value (see Figure 6.8, next section). A significant change of $\Delta G_{\text{sd} \rightarrow h}$ with decreasing temperature would manifest itself as a slope in the $\Delta G_{\text{n} \rightarrow h}(T)$ curve. This is not

observed. This finding together with the agreement of calculated crystal sizes with previously reported values indicates that the increased vapor pressure below about 170 K is of morphological origin and can be explained solely by the well-established formation of nanoscale grains.

It has been reported, that ASW might be deposited in a porous form depending on deposition angle, rate and temperature [Dohnalek et al., 2003; Hill et al., 2016; Kimmel et al., 2001a,b; Kouchi et al., 1994; Mayer and Pletzer, 1986; Mitterdorfer et al., 2014; Raut et al., 2007; Stevenson et al., 1999]. Yet, deposition of ASW at temperatures between 90 and 110 K revealed only small degrees of porosity [Brown et al., 1996; Chonde et al., 2006] or were non-porous [Kimmel et al., 2001b; Stevenson et al., 1999]. Thus, reports of the porosity of ASW deposited at conditions comparable to this studies are inconsistent. Therefore, a small degree of porosity of the ASW samples cannot be excluded. However, since the same crystalline ice forms independent of deposition temperature, it is likely that either all ASW samples are non-porous or that any porosity of the ASW sample deposited at 95 and 100 K has no influence on the ice grain sizes formed during crystallization. The latter is supported by the observation of a strong increase in density of micro-porous ASW at annealing temperatures above 100 K and a complete absence of micro-pores above 140 K [Hill et al., 2016; Kimmel et al., 2001b; Raut et al., 2007].

6.3.3. The vapor pressure over nano-crystalline ice and ASW

The vapor pressure of a metastable ice polymorph can be expressed by a Gibbs free energy difference to the stable hexagonal ice phase (Equation 2.4.2). The normalized vapor pressure data for ASW and nano-crystalline ice I_{sd} displayed in Figure 6.6 was used to calculate ΔG with respect to hexagonal ice. The results are shown in Figure 6.8. The blue diamonds represent the results for ASW and the red squares the results for nano-crystalline ice.

Nano-crystalline ice I_{sd}

Below 160 K the nano-crystalline ice exhibits a strongly enhanced saturation vapor pressure compared to morphologically flat ice I_{sd} . The nanoscale grains are stable for several hours and thus nano-crystalline ice can be regarded as a distinct metastable ice phase. No dependency of $\Delta G_{sd,n \rightarrow h}$ on temperature is apparent from the data. Considering that $\Delta G_{sd,n \rightarrow h} = \Delta H_{sd,n \rightarrow h} - T \Delta S_{sd,n \rightarrow h}$, the vapor pressure above nano-crystalline ice I_{sd} is represented by a constant Gibbs free energy and enthalpy difference of

$$\begin{aligned} \Delta G_{sd,n \rightarrow h} &= \Delta H_{sd,n \rightarrow h} = (982 \pm 182) \text{ Jmol}^{-1}, \\ \Delta S_{sd,n \rightarrow h} &= 0 \text{ Jmol}^{-1} \text{ K}^{-1}. \end{aligned} \quad (6.3.2)$$

The parameterization is shown by the red dashed line in Figure 6.8 with the shaded area representing the uncertainty.

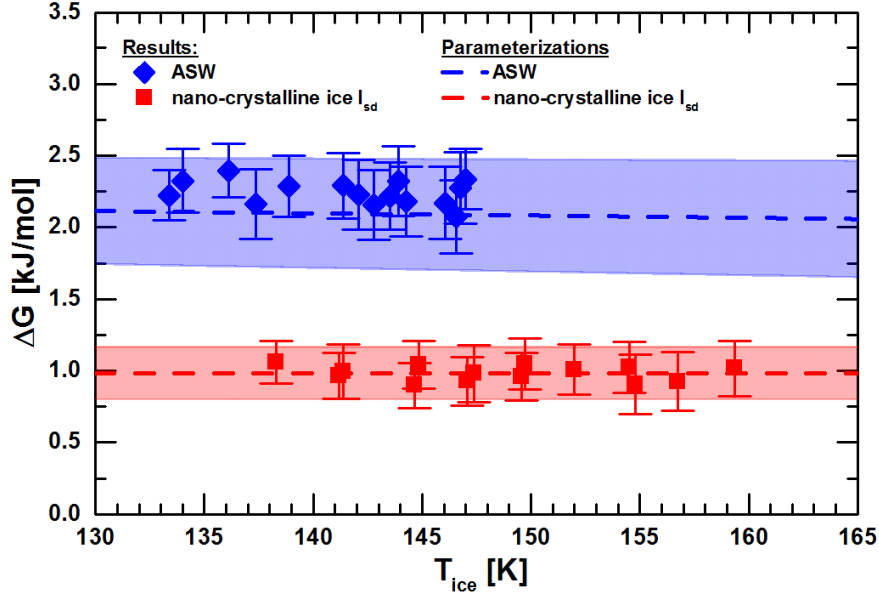


Figure 6.8.: Calculated Gibbs free energy difference ΔG with respect to ice I_h as a function of temperature using the measured vapor pressure difference displayed in Figure 6.6 for ASW (blue diamonds) and nano-crystalline ice I_{sd} (red squares). The blue and red dashed lines represent parameterizations of the ice phases according to Equations 6.3.2 and 6.3.5 including a shaded interval of uncertainty.

Amorphous solid water

A linear fit to the Gibbs free energy difference $\Delta G_{a \rightarrow h}$ of ASW with respect to ice I_h determines $\Delta H_{a \rightarrow h}$ and $\Delta S_{a \rightarrow h}$. However, due to the limited number of $\Delta G_{a \rightarrow h}$ data in a restricted temperature range of 14 K, the fit results in large uncertainties:

$$\begin{aligned} \Delta H_{a \rightarrow h} &= (2960 \pm 660) \text{ Jmol}^{-1} \\ \Delta S_{a \rightarrow h} &= (5 \pm 4.7) \text{ Jmol}^{-1}\text{K}^{-1}. \end{aligned} \quad (6.3.3)$$

Combining the data of this work with the work of [Smith et al. \[2011\]](#) allows to constrain $\Delta H_{a \rightarrow h}$ and $\Delta S_{a \rightarrow h}$ with a higher precision than obtained with the linear fit. [Smith et al. \[2011\]](#) deposited ASW at 85 K and measured the desorption rate of ASW during temperature ramping. The ice sample crystallized at 155 K at which point the temperature was reduced and the same temperature ramp was conducted to measure the desorption rate of the crystalline sample. Their data exhibit a high absolute uncertainty due to a nominally large temperature uncertainty (2 K). However, the relative difference between the amorphous and crystalline ice sample is more accurate. They determined the Gibbs free energy difference between both ice phases between 130 and 150 K and constrained $\Delta G_{a \rightarrow c}$ (150 K) to $(1100 \pm 50) \text{ Jmol}^{-1}$ and $\Delta S_{a \rightarrow c}$ (150 K) to $(1.6 \pm 1) \text{ Jmol}^{-1}\text{K}^{-1}$. Consequently, $\Delta H_{a \rightarrow c}$ (150 K) = $(1340 \pm 158) \text{ Jmol}^{-1}$. Considering that ASW crystallizes to nano-grained ice I_{sd} at 155 K, their crystalline data

reflect nano-crystalline ice I_{sd} and not morphologically flat crystalline ice. Hence, the enthalpy and entropy difference at 150 K between ASW and hexagonal ice I_h is the sum of the steps from ASW to nano-crystalline ice and from nano-crystalline ice to hexagonal ice, i.e.

$$\begin{aligned}\Delta H_{a \rightarrow h}(150 \text{ K}) &= \underbrace{\Delta H_{a \rightarrow sd,n}}_{\text{[Smith et al., 2011]}} + \underbrace{\Delta H_{sd,n \rightarrow h}}_{\text{this work}} = (2322 \pm 241) \text{ Jmol}^{-1} \quad (6.3.4) \\ \Delta S_{a \rightarrow h}(150 \text{ K}) &= \underbrace{\Delta S_{a \rightarrow sd,n}}_{\text{[Smith et al., 2011]}} + \underbrace{\Delta S_{sd,n \rightarrow h}}_{\text{this work}} = (1.6 \pm 1) \text{ Jmol}^{-1}\text{K}^{-1}.\end{aligned}$$

The calculated enthalpy and entropy differences agree with the linear fit results for the ASW data presented above. However, the uncertainty range is lower than for the ASW fit results. The values for the enthalpy and entropy difference are applicable over a wide temperature range. $d\Delta H_{a \rightarrow h}/dT$ is the heat capacity difference between ASW and ice I_h and measurements by [Sugisaki et al. \[1968\]](#) and [Chonde et al. \[2006\]](#) found no difference in the heat capacity of ASW and ice I_h between 60 and 200 K. Hence, $\Delta H_{a \rightarrow h}$ and $\Delta S_{a \rightarrow h}$ are constants in that temperature range and $\Delta G_{a \rightarrow h}$ is described by

$$\begin{aligned}\Delta G_{a \rightarrow h} &= \Delta H_{a \rightarrow h} - T \cdot \Delta S_{a \rightarrow h} \quad (6.3.5) \\ \Delta H_{a \rightarrow h} &= (2322 \pm 241) \text{ Jmol}^{-1} \\ \Delta S_{a \rightarrow h} &= (1.6 \pm 1) \text{ Jmol}^{-1}\text{K}^{-1}.\end{aligned}$$

This parameterization is indicated by the blue dashed line in Figure 6.8 with the shaded area representing the uncertainty. It is in good agreement with the thermodynamical data for ASW.

The saturation vapor pressures of ASW and nano-crystalline ice I_{sd} with respect to ice I_h are parameterized using the determined Gibbs free energy differences in Equation 2.4.2. Figure 6.9 displays the different parameterizations normalized to hexagonal ice I_h at temperatures relevant to the terrestrial mesopause. The shaded areas represent the uncertainties. The experimental results for nano-crystalline ice I_{sd} and ASW obtained with the MICE-TRAPS setup are shown by the red squares and blue diamonds, respectively. For comparison, Figure 6.9 shows the parameterization for macro-crystalline stacking disordered ice I_{sd} by the gray shaded area. At conditions of the summer mesopause, the vapor pressure of ASW is four to twenty times increased with respect to hexagonal ice I_h . The vapor pressure of nano-crystalline ice I_{sd} is two to four times increased with respect to hexagonal ice I_h . The vapor pressure parameterization for supercooled liquid water from [Murphy and Koop \[2005\]](#) is shown by the black dotted line. Here, the vapor pressure of supercooled water at 150 K is described with a Gibbs free energy difference to hexagonal ice of 1100 Jmol^{-1} based on the results from [\[Speedy et al., 1996; Brown et al., 1996; Smith et al., 2011\]](#). However, at that time, the nano-crystalline nature of ice I_{sd} when crystallized from ASW at temperatures below 160 K was not yet established. As a result, the parameterization of

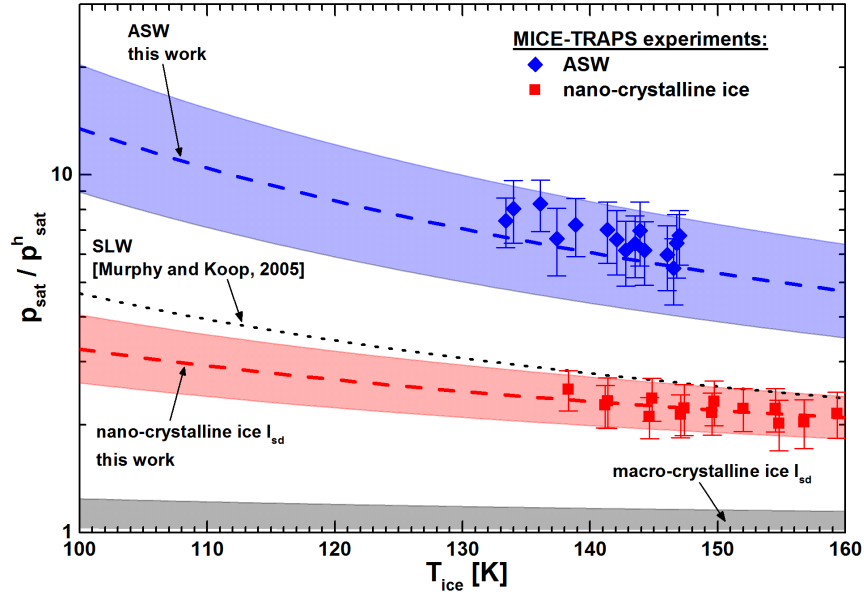


Figure 6.9.: The saturation vapor pressure of low temperature deposited ices with respect to ice I_h at temperatures relevant to the summer mesopause. The parameterizations obtained in this work for ASW and nano-crystalline ice I_{sd} are shown by the blue and red dashed lines, respectively. The shaded areas represent the uncertainties. The blue diamonds and red squares show the experimental results for ASW and nano-crystalline ice. For comparison, parameterizations from literature for macro-crystalline stacking disorder ice I_{sd} (gray shaded area) and supercooled liquid water (SLW, black dotted line) [Murphy and Koop, 2005] are shown.

Murphy and Koop [2005] underestimates the vapor pressure by a factor of 2 at 160 K and a factor of 4 at 100 K. Note that the determined entropy and enthalpy difference of ASW with respect to ice I_h still allows to connect ASW and supercooled water by a single thermodynamic function [e.g. Murphy and Koop, 2005; Johari et al., 1994; Speedy, 1992]. Such a parameterization for the vapor pressure would need to match the parameterization derived in this work between 60 and 200 K and be in agreement with the parameterization of Murphy and Koop [2005] for supercooled water above 235 K.

6.3.4. Comparison to DSC measurements

The proceeding sections establish the two-step nature of the process in which ASW converts to ice I_{sd} by first crystallizing to nano-crystalline ice I_{sd} , followed by slow crystal growth and relaxation to macro-crystalline ice I_{sd} at temperatures above 165 K. This intermediate step in the transformation from ASW to ice I_{sd} explains the much smaller enthalpy differences found in conventional Differential Scanning Calorimetry (DSC) measurements of the crystallization process of ASW ($\Delta H \approx 1280 - 1800 \text{ Jmol}^{-1}$ [Sug-

isaki et al., 1968; Handa et al., 1986; Hallbrucker and Mayer, 1987; Hallbrucker et al., 1989; Ghormley, 1968; Macfarlane and Angell, 1984; Floriano et al., 1989; Johari et al., 1994]):

Typically, conventional DSC measurements are performed with heating rates below 30 K min^{-1} . This results in complete crystallization below 165 K. For such measurements, only the heat associated with the transformation from ASW to nano-crystalline ice I_{sd} is released and visible in the DSC signal. According to this work, the enthalpy difference of ASW with respect to nanocrystalline ice I_{sd} below 165 K corresponds to approximately 1300 J mol^{-1} which is in excellent agreement with the majority of the DSC measurements. Above 165 K, heat should then be released continuously due to crystal growth. However, the enthalpy difference of approximately 800 J mol^{-1} attributed to this process is invisible in conventional DSC measurements for two reasons. (1) Crystal growth in the completely crystalline ice polymorph consisting of nanocrystals requires tens of minutes to hours [Hansen et al., 2008]. At heating rates of 30 K min^{-1} , the temperature range at which crystal growth is active is scanned within one minute which is too fast for significant crystal growth and thus no heat release is visible in the DSC measurements. The heat corresponding to crystal growth should then be released during melting and should be seen in a reduction of the heat of melting. Unfortunately, for such high heating rates, the heat of melting is usually not documented or the samples are not heated above the melting temperature. (2) For slow heating rates of about 1 K min^{-1} or below, the heat of crystal growth is released continuously during half an hour or longer time periods. For such long time periods, the continuous heat release associated to crystal growth does not result in a prominent DSC signal, but rather causes a shift in the measured heat capacity values. Such a small, but continuous heat release then challenges the procedure of drawing baselines to the DSC data for the calculation of the heat release. Here, measurements of hexagonal ice would be necessary for comparison.

I reviewed the available heat capacity data and summarize them in Figure 6.10. The upper panel shows typical raw DSC signals in arbitrary units from Johari et al. [1994] and Chonde et al. [2006] employing different heating rates (1 K min^{-1} , 10 K min^{-1} , 30 K min^{-1} and 10^5 K s^{-1}). The higher the heating rates, the higher the crystallization temperature and the broader the peak width of the DSC measurements. The lower panel shows the heat release determined from the DSC signals (enthalpy difference ΔH) as a function of temperature. The crystallization temperatures correspond to the temperature of maximum heat release and the uncertainty reflects the peak width. The colored data points correspond to the raw DSC signals shown in the upper panel. Black squares correspond to data from [Handa et al., 1986; Hallbrucker and Mayer, 1987; Hallbrucker et al., 1989; Ghormley, 1968; Macfarlane and Angell, 1984; Floriano et al., 1989]. The data show an increasing heat release with increasing heating rate and crystallization temperature. Johari postulated this effect to be due to a difference in the heat capacity of ASW and crystalline ice and thus an enthalpy difference which increases with temperature. Recent heat capacity measurements showed no significant

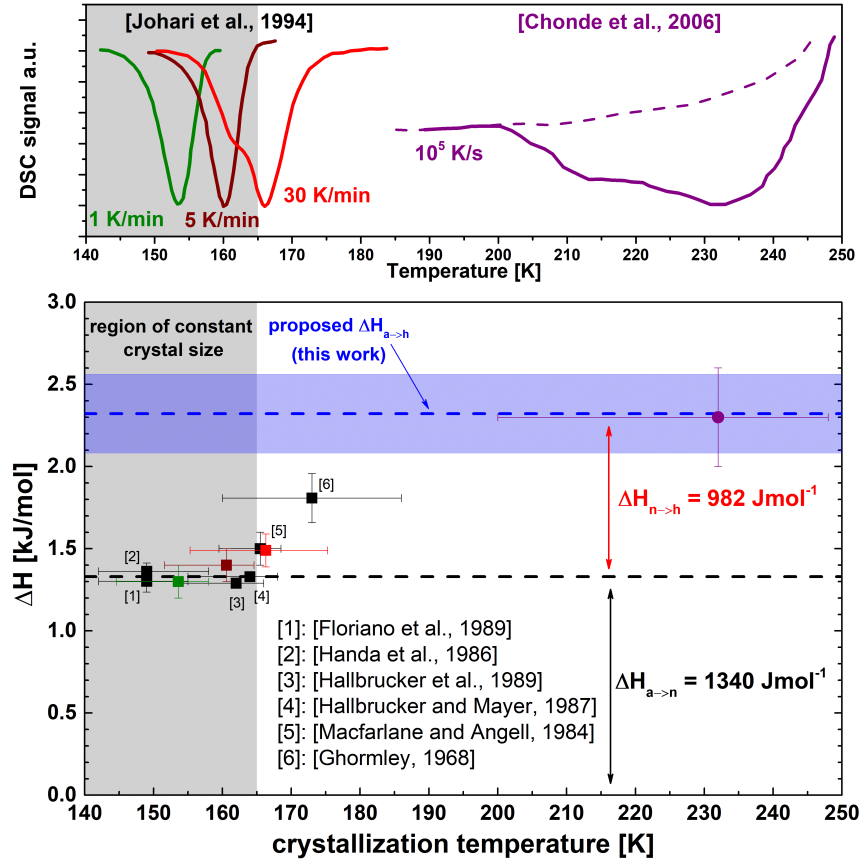


Figure 6.10.: Review of DSC measurements. The upper panel shows raw DSC signals for four different heating rates. The lower panel shows the determined heat release ΔH as a function of temperature at which crystallization took place. The colored data points indicate the belonging to the raw DSC signals in the upper panel.

difference in the heat capacity of ASW and crystalline ice between 150 K and 200 K [Chonde et al., 2006] making this scenario very unlikely.

The formation of constant crystal sizes below 165 K is explained by a temperature independent ratio of nucleation rates and diffusional growth within the remaining ASW matrix until all amorphous water is transformed to crystalline ice. If crystallization within the ASW matrix takes place above 165 K, the ratio of nucleation rate to diffusional growth reduces so that larger crystals form compared to temperatures below that limit. As a consequence, more heat is released during crystallization. This is clearly visible in Figure 6.10. All DSC measurements for which crystallization was completed in the temperature range of constant crystal sizes ($T < 165$ K) show a heat release which is in good agreement with the 1340 Jmol^{-1} expected for the transformation from ASW to nano-crystalline ice I_{sd} (horizontal black dashed line). As soon as parts of the crystallization process exceed 165 K, the heat release increases and all reported

DSC measurements exhibit two distinct peaks instead of only one (compare red and purple curve in the upper panel). Two peaks in the DSC data indicate that heat is released via two distinct processes. These two processes can be attributed to (1) the nucleation and (2) the subsequent growth to larger crystals within the ASW matrix. After crystallization of ASW is complete, growth of the crystals to larger sizes takes place on a time-scale of tens of minutes to hours and thus the energy corresponding to that process is not visible in the DSC data as discussed above.

Ultrafast calorimetry measurements with heating rates on the order of $10^4 - 10^5 \text{ K s}^{-1}$ result in the crystallization of ASW occurring between 200 and 250 K. Using this technique, also two distinct transformations were observed [Chonde et al., 2006; Sepulveda et al., 2012]. This experiment measures the enthalpy difference between ASW and macroscopic hexagonal ice I_h . Indeed, Chonde et al. [2006] report an enthalpy of crystallization of $(2300 \pm 300) \text{ Jmol}^{-1}$ shown by the purple dot in Figure 6.10. It is in very good agreement with the enthalpy difference between ASW and ice I_h determined in this study (horizontal blue dashed line with the shaded area indicating the uncertainty). In addition, the good agreement of ΔH from Chonde et al. [2006] with the result of this work supports the assumption of a constant value of ΔH with temperature up to 200 K.

6.4. Conclusions

H_2O vapor pressure measurements of ice samples deposited from the gas phase at conditions relevant for cloud formation in the terrestrial mesopause were performed. The results show that below 160 K ASW deposits from the vapor phase. Over time, ASW crystallizes to a nano-crystalline form of stacking disordered ice I_{sd} . At temperatures above 165 K, crystal growth is effectively activated resulting in the relaxation to macro-crystalline ice I_{sd} .

At temperatures relevant for the summer mesopause, the vapor pressure of nano-crystalline ice I_{sd} is 2 to 4 times higher compared to stable hexagonal ice. The observed high vapor pressure is quantitatively explained by the high surface energy to volume energy ratio of nano-scale crystals (Kelvin effect). Below 160 K the crystals are stable for hours. Therefore, nano-crystalline ice can be considered as an independent phase in ice cloud processes. The vapor pressure of nano-crystalline ice can be calculated using Equation 2.4.2 and Equation 6.3.2.

At temperatures relevant for the summer mesopause the saturation vapor pressure of ASW is 2 to 4 times higher than previously assumed. This result is explained by the the impact of the transition from ASW to the nano-crystalline form of stacking disordered ice I_{sd} . Although known for some time, this fact had not been considered in the prior analysis of vapor pressure measurements nor in heat capacity measurements which has lead to a significant underestimation of the vapor pressure. The vapor pressure measurements for ASW in this work reconcile well with literature data for the vapor pressure and heat capacity measurements when considering the two step nature

of crystallization. The vapor pressure of ASW can be calculated with Equation 2.4.2 and Equation 6.3.5. These calculations are valid between 60 and 200 K.

The following chapter presents H₂O adsorption and nucleation experiments using MICE-TRAPS. In these experiments, H₂O ice was deposited on the sample surfaces in MICE at 160 K. Hence, the vapor pressure parameterization of nano-crystalline ice must be used to describe the flux of H₂O molecules to the particles levitated in MICE.

The content of this chapter aims to answer the first question formulated in the introduction:

What is the predominant ice phase involved in PMC formation?

At the extreme temperatures of the summer mesopause, ASW deposits from the gas phase. Consequently, the formation of ice particles in the summer mesopause is dominated by the properties of ASW rather than crystalline ice. Over time, ASW crystallizes to nano-crystalline ice I_{sd}, which is stable at mesopause temperatures and for PMC lifetimes. Depending on the thermal history of PMC ice particles, the vapor pressure of ASW or nano-crystalline ice I_{sd} determines the sublimation process.

7. H₂O nucleation experiments

This chapter reports on adsorption and nucleation experiments of H₂O on nanometer-sized silica (SiO₂), iron oxide (Fe₂O₃) and mixed iron silicate (Fe_xSi_{1-x}O₃) particles using MICE-TRAPS. The particles serve as analogues for Meteoric Smoke Particles (MSPs). Particle temperatures are between 128 and 155 K which is representative for the terrestrial mesopause.

The deposition of H₂O molecules on the nanoparticles was used to determine the desorption energy ΔF_{des} for H₂O molecules on the surface of the particles. In addition, the critical saturations S_{cr} (saturation at which ice particle growth sets in) were determined. The experimental method is introduced in Section 7.1. Section 7.2 presents the results for the desorption energy ΔF_{des} and the critical saturations S_{cr} . These results are used in Section 7.3 to develop a model which predicts S_{cr} values for Polar Mesospheric Cloud (PMC) formation. Section 7.4 recalls the main findings of this chapter and aims to answer the second question formulated in the introduction:

What are onset conditions for PMC formation?

7.1. Methods

Singly charged iron oxide and silica particles of variable but well known initial mass were exposed to a controlled H₂O supersaturation at temperatures between 128 and 155 K. In each individual experiment MICE was filled with particles of well known size. The time resolved mass of the trapped particles was then periodically recorded by extracting small samples of the trapped particle population into the TOF mass spectrometer. Figure 7.1 shows growth measurements on silica particles of 2.6 nm initial radius at three different particle temperatures. For this series of measurements, the H₂O concentration is $n_{\text{H}_2\text{O}} = 1.1 \times 10^{16} \text{ m}^{-3}$. The particle temperature and with it the saturation differ between the individual measurements. Note that saturation values are given with respect to hexagonal ice I_h. The dotted lines are for guidance of the eye. Three different growth regimes can be distinguished in Figure 7.1.

(1) Curve a) (147.4 K and $S \approx 8$) corresponds to a situation where the supersaturation is too low to activate ice growth and only adsorption of H₂O molecules on the particle surface is observed. The amount of adsorbed H₂O molecules increases until an equilibrium between adsorbing and desorbing molecules on the surface of the nucleus is reached (Equation 4.3.4). This process is described reasonably well by an empirical

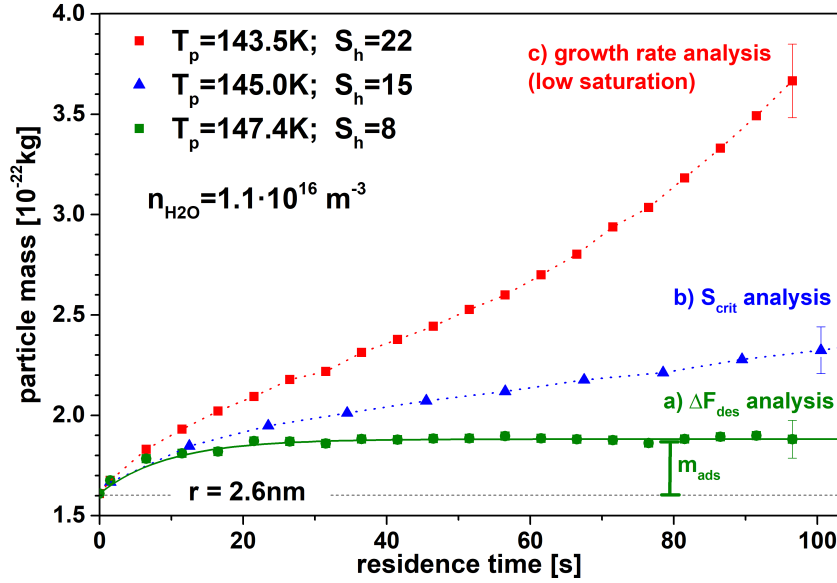


Figure 7.1.: Series of H₂O deposition measurements on 2.6 nm silica particles at constant H₂O concentration. By decreasing temperature, and thus increasing saturation, the deposition regime can be changed from adsorption only (curve a) to growth (curve b and c).

expression of the form

$$m(t) = m_0 + m_{\text{ads}} \cdot \left[1 - \exp\left(-\frac{t_{\text{res}}}{\tau}\right) \right]. \quad (7.1.1)$$

Equation 7.1.1 determines the total mass of adsorbed H₂O molecules in equilibrium (m_{ads}) and therefore the number of adsorbed H₂O molecules on the surface of the particles with initial mass m_0 . The fit of Equation 7.1.1 to curve a) is shown in Figure 7.1 by the green solid line. The fit yields $m_{\text{ads}} = 2.7 \times 10^{-23}$ kg corresponding to about 900 H₂O molecules or 0.9 mono-layers. Corrected R² values of the exponential fits are typically better than 0.99. Dividing the number of adsorbed molecules by the surface area of the particle yields the surface concentration of adsorbed H₂O molecules $c_{1,s}$. Equation 4.3.4 can be solved for the desorption energy

$$\Delta F_{\text{des}} = kT_{\text{N}} \cdot \ln\left(\frac{c_{1,s}\nu\sqrt{2\pi m_{\text{molec}}}}{n_{\text{molec}} \cdot \sqrt{kT_{\text{env}}}}\right). \quad (7.1.2)$$

(2) For a slightly lower temperature (curve b, 145 K and $S \approx 15$) the saturation is high enough to activate unlimited particle growth. By changing saturations in small steps, the transition between adsorption (curve a) and further growth (curve b) is observed. The saturation at which the growth regime is activated is the critical saturation S_{cr} . In this case, the critical saturation is $S_{\text{cr}} = 11.5 \pm 3.5$ at a mean particle temperature

of 146.2 K.

(3) At still lower particle temperature (curve c, 143.5 K and $S \approx 22$), the outgoing H₂O flux is reduced and the particles grow faster. Ice particle growth for such conditions was used to determine the saturation vapor pressure of the ASW phase deposited on the particles. The results of these measurements are presented in Chapter 6.

7.2. Results

7.2.1. Desorption energy

H₂O adsorption at saturations below the critical saturation was investigated on silica particles with radii between 1.5 and 2.8 nm, on iron oxide particles with radii between 1 and 3.1 nm, and on mixed iron silicates with radii between 1.4 and 2.3 nm. The particle temperature was varied between 128 and 155 K. H₂O concentrations varied between 1×10^{14} and $2 \times 10^{16} \text{ m}^{-3}$ corresponding to saturations between 4 and 40 with respect to hexagonal ice. The desorption energy for iron oxide particles was determined from the measured adsorbed mass of water molecules in equilibrium using Equation 7.1.2. The results are shown in Figure 7.2 by the open red triangles as a function of $1/r$. The desorption energies exhibit a pronounced trend with particle

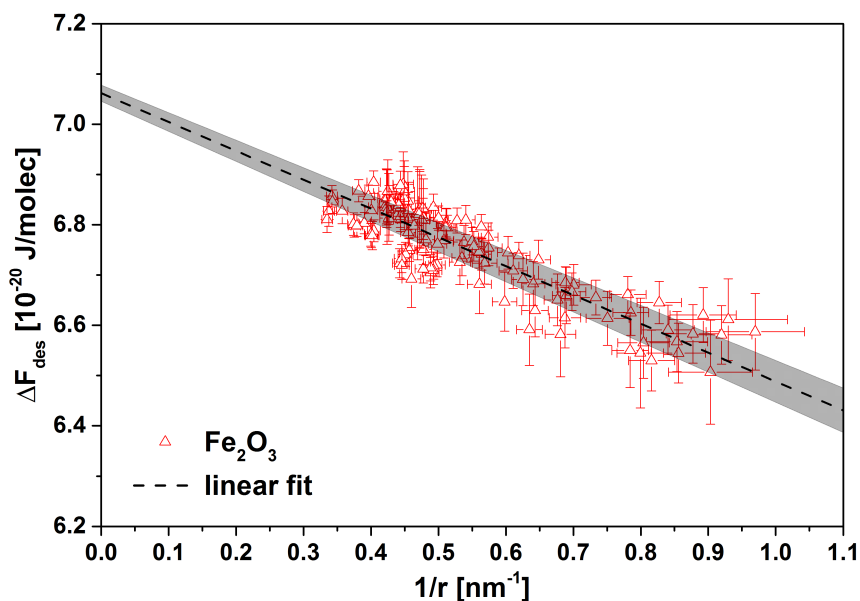


Figure 7.2.: Desorption energy of iron oxide particles as a function of $1/r$ analyzed with Equation 7.1.2. The black dashed line is a linear fit to the data.

radius. This effect can be explained as follows. The desorption energy (Equation 7.1.2) is calculated from the equilibrium concentration of adsorbed molecules (Equation 4.3.4). This equation assumes an equilibrium between the incoming (Equation 4.3.2)

and the outgoing H₂O flux density (Equation 4.3.3). For small particles the curvature causes that the adsorbed molecules are less effectively bound to the surface. Thus, the outgoing flow is increased. This effect may be considered in analogy to the Kelvin effect by multiplying the outgoing flow with a factor

$$S_{\text{eq,des}} = \exp\left(\frac{2m_{\text{molec}}\sigma_{\text{des}}}{kT\rho r}\right). \quad (7.2.1)$$

Here, σ_{des} can be regarded as an effective surface tension which describes the dependency of the binding energy of an adsorbed molecule on the particle size. Multiplying the outgoing flow with $S_{\text{eq,des}}$ yields the equilibrium concentration of adsorbed molecules and the desorption energy for a planar surface $\Delta F_{\text{des,pl}}$

$$c_{1,s} = \frac{n_{\text{molec}} \cdot \sqrt{kT_{\text{env}}}}{S_{\text{eq,des}} \cdot \nu \sqrt{2\pi m_{\text{molec}}}} \cdot \exp\left(\frac{\Delta F_{\text{des,pl}}}{kT_{\text{N}}}\right), \quad (7.2.2)$$

$$\Delta F_{\text{des,pl}} = kT_{\text{N}} \cdot \ln\left(\frac{S_{\text{eq,des}} \cdot c_{1,s} \nu \sqrt{2\pi m_{\text{molec}}}}{n_{\text{molec}} \cdot \sqrt{kT_{\text{env}}}}\right). \quad (7.2.3)$$

Rearranging Equation 7.2.3 results in

$$\Delta F_{\text{des}} = \Delta F_{\text{des,pl}} - \frac{2m_{\text{molec}}\sigma_{\text{des}}}{\rho r}. \quad (7.2.4)$$

ΔF_{des} is the size dependent desorption energy (Figure 7.2) analyzed with Equation 7.1.2. A linear fit to the ΔF_{des} data is shown by the black dashed line. The shaded area indicates the uncertainty. The slope of the linear fit yields $\sigma_{\text{des}} = (0.89 \pm 0.004) \text{ Nm}^{-1}$. The intercept is the desorption energy for the planar surface, which in this case is $\Delta F_{\text{des,pl}} = (7.06 \pm 0.02) \cdot 10^{-20} \text{ J/molec}$. The value for $\Delta F_{\text{des,pl}}$ is very close to the H₂O sublimation energy at these temperatures which is approximately $7 \times 10^{-20} \text{ J/molec}$ [e.g. [Sack and Baragiola, 1993](#)]. Thus, also the effective surface tension should be very close to the surface tension of ASW. Indeed, the surface tension of ASW is 0.92 Nm^{-1} at 155 K and 0.96 Nm^{-1} at 128 K (Table B.1) which is in good agreement with the slope of the fit. Therefore, it is assumed that the surface tension of ASW describes the influence of the particle size on the binding energy sufficiently well.

The data for iron oxide, silica and mixed iron silicate particles with a stoichiometric composition of $\text{Fe}_{0.7}\text{Si}_{0.3}\text{O}_3$ was analyzed with Equation 7.2.3 using the surface tension of ASW. The results are shown in Figure 7.3 as a function of particle temperature. Red triangles represent the data for iron oxide particles, black squares for silica particles and green dots for mixed iron silicates. The results show no influence of the particle temperature on $\Delta F_{\text{des,pl}}$. In addition, no influence of the particle size on $\Delta F_{\text{des,pl}}$ is visible which justifies using the same surface tension for all three materials. The

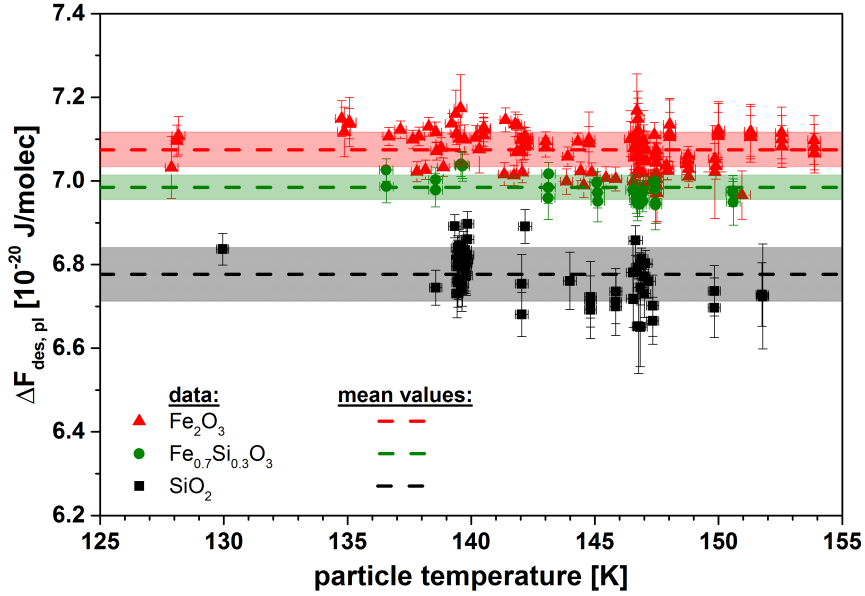


Figure 7.3.: Desorption energy as a function of particle temperature analyzed with Equation 7.2.3 using the surface tension of ASW. Data is shown for iron oxide (red triangles), silica (black squares), and mixed iron silicates (green dots). The horizontal dashed lines indicate the mean values with the shaded areas representing the uncertainty.

desorption energies are

$$\begin{aligned} \text{Fe}_2\text{O}_3 : \quad \Delta F_{\text{des,pl}} &= (7.07 \pm 0.05) \cdot 10^{-20} \text{ J/molec}, & (7.2.5) \\ \text{SiO}_2 : \quad \Delta F_{\text{des,pl}} &= (6.78 \pm 0.06) \cdot 10^{-20} \text{ J/molec}, \\ \text{Fe}_{0.7}\text{Si}_{0.3}\text{O}_3 : \quad \Delta F_{\text{des,pl}} &= (6.98 \pm 0.03) \cdot 10^{-20} \text{ J/molec}. \end{aligned}$$

The H_2O desorption energies for mixed iron silicate particles with different iron contents were also investigated. The iron to silicon ratio was varied by adjusting the temperatures of the silicon and iron precursors as discussed in the experimental section and Appendix A. The results are shown in Figure 7.4 as a function of the atomic $[\text{Fe}]:([\text{Fe}]+[\text{Si}])$ ratio (blue dots). Here, $[\text{Fe}]$ and $[\text{Si}]$ are the atomic contents of iron and silicon. The red triangle, the black square and the green dot show the mean values determined above for iron oxide, silica and $\text{Fe}_{0.7}\text{Si}_{0.3}\text{O}_3$ particles, respectively. The desorption energy exhibits a linear trend as function of the atomic ratio. A fit to the data yields the mean value of $\Delta F_{\text{des,pl}}$ as a function of the atomic ratio

$$\Delta F_{\text{des}} = 6.764 + 0.312 \cdot \frac{[\text{Fe}]}{[\text{Fe}] + [\text{Si}]} [10^{-20} \text{ J/molec}]. \quad (7.2.6)$$

The desorption energies of all investigated materials are close to the sublimation energy of water ice. This compares well to previous H_2O adsorption measurements although

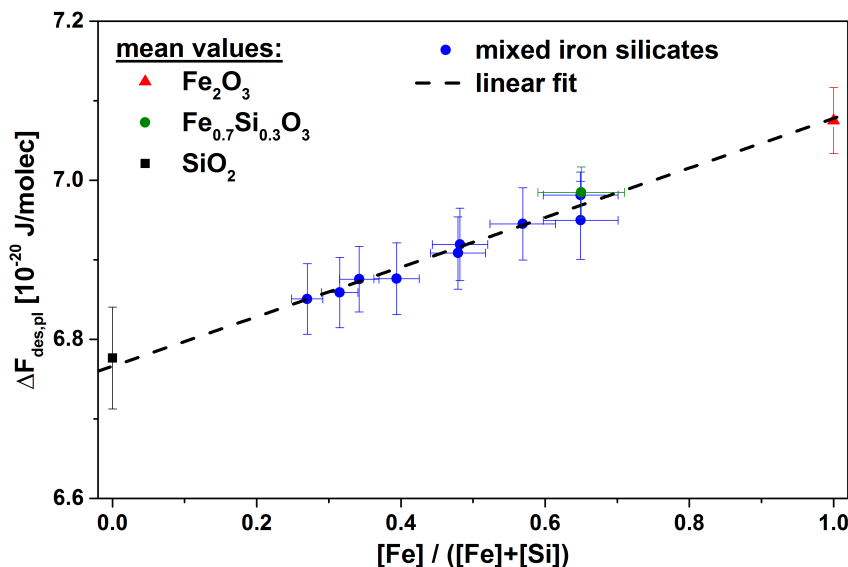


Figure 7.4.: Desorption energy of mixed iron silicates as a function of the atomic [Fe]:([Fe]+[Si]) ratio (blue dots). the red triangle, the black square and the green dot are mean values for iron oxide, silica and Fe_{0.7}Si_{0.3}O₃ particles, respectively. The black dashed line is a linear fit to the data. Reanalyzed data from Nachbar et al. [2018b].

the H₂O desorption energy for the first few molecules on bare silica and iron oxide is about 1.5×10^{-19} J/molec [Navrotsky et al., 2008; Sneh et al., 1996] i.e. higher than the sublimation energy of H₂O ice. For materials with such a high desorption energy, a homogeneous mono-layer of H₂O is adsorbed already at sub-saturated conditions. In general, several layers of the adsorbent may form on such samples [Venables et al., 1984]. The mean desorption energy of all adsorbed molecules then decreases with increasing water coverage and reaches values close to the sublimation energy of H₂O for coverages larger than 0.5 mono-layers [Navrotsky et al., 2008; Sneh et al., 1996]. The mono-layer coverage of all adsorption measurements performed in this work is between 0.5 and 3. The desorption energy therefore has to be regarded as a mean desorption energy of a water molecule at coverages above 0.5 mono-layers.

7.2.2. Critical saturations

Experiments to determine critical saturations S_{cr} were conducted with silica, iron oxide and mixed iron silicate particles. S_{cr} values describe the onset saturation for ice particle growth, i.e. the transition between adsorption and growth regime. While keeping the particle temperature constant, the saturation was increased step by step until growth was observed. The critical saturation is the arithmetic mean value between the highest saturation showing solely adsorption and the lowest saturation exhibiting growth conditions. Critical saturations were determined for particle radii between 1

and 3 nm at 128, 135, 140, and 147 K. The particle temperature in the individual experiments deviates less than 1 K from the mean value.

Figure 7.5 (panel a) shows measured critical saturations with respect to hexagonal ice $S_{cr,h}$ as a function of particle radius at 140 K. $S_{cr,h}$ values increase with decreasing particle radius and are between 10 and 35 for radii between 3 and 1 nm. For a given

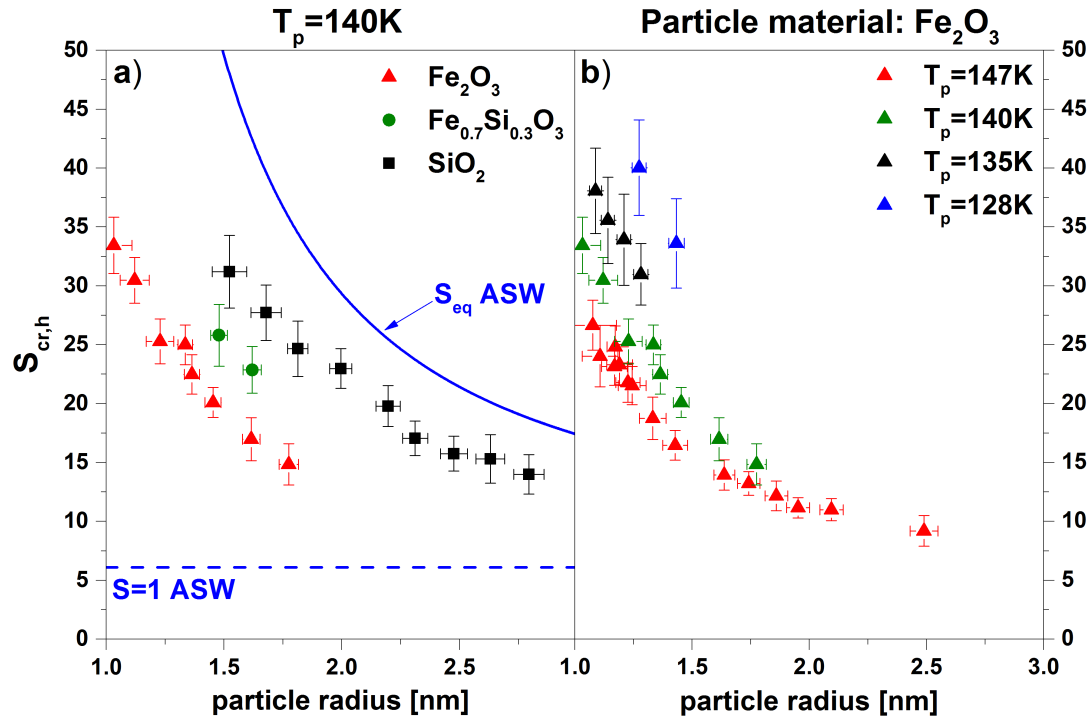


Figure 7.5.: Critical saturations with respect to hexagonal ice $S_{cr,h}$ as a function of the particle radius. Panel a: measured $S_{cr,h}$ values for silica (black squares), mixed iron silicate (green dots), and iron oxide (red triangles) particles at 140 K. The blue dashed line shows the saturation vapor pressure and the blue solid line the Kelvin effect for ASW. Panel b: Measured critical saturations for iron oxide particles at 147, 140, 135, and 128 K (red, green, black, and blue triangles, respectively).

particle radius, critical saturations are highest for silica particles and lowest for iron oxide particles. Values for mixed iron silicates fall in-between the results for iron oxide and silica particles.

In Chapter 6 it is shown that ASW deposits on the particles. $S=1$ of ASW for 140 K is shown by the blue dashed line of Figure 7.2 (panel a). The saturation vapor pressure of ASW is elevated by a factor of 6 with respect to hexagonal ice for these conditions (Equation 6.3.5). The blue solid line shows Kelvin effect calculations according to Equation 4.1.3 using the surface tension of ASW and the saturation vapor pressure of ASW. Surprisingly, growth activates for all particle materials below the Kelvin effect

for ASW. A growth activation model explaining this phenomenon is introduced in the next section.

Panel b) of Figure 7.2 shows critical saturations as a function of particle radius for iron oxide particles at 4 different temperatures, 147, 140, 135, and 128 K (red, green, black, and blue triangles, respectively). Critical saturations increase with decreasing particle temperature.

7.3. Discussion

7.3.1. Activation model

In Chapter 6 it is shown that ASW deposits on the surface of the particles during growth. Very surprisingly, ice particle growth activates for all investigated particle materials below the Kelvin effect for ASW. The following presents a model which describes measured critical saturations on the basis of Kelvin effect calculations.

Let us assume a spherical ice particle made up of ASW. Such a particle is in equilibrium with its environment if the incoming H₂O flux equals the sublimation flux from the particle surface. The incoming and outgoing flux is described in the ice particle growth model in Chapter 4.5 (Equation 4.5.2). In brief, the sublimation flux is proportional to $p_{\text{sat}} \cdot A_{\text{p}} \cdot S_{\text{eq}}$, with the saturation vapor pressure p_{sat} , the particle surface area A_{p} and the equilibrium saturation over the curved surface of the particle S_{eq} (Kelvin effect). The incoming flux is proportional to $p_{\text{sat}} \cdot A_{\text{c}} \cdot S$. Here, A_{c} is the effective collision surface area of the particle including the collision radius of an H₂O molecule and S is the H₂O saturation of the environment. Equalizing the incoming and outgoing flow yields the critical saturation

$$S_{\text{cr}} = S_{\text{eq}}(r_{\text{p}}, T_{\text{p}}) \cdot \left(\frac{r_{\text{p}}}{r_{\text{p}} + r_{\text{molec}}} \right)^2. \quad (7.3.1)$$

According to this simple expression critical saturations are reduced with respect to Kelvin effect calculations because the hard sphere collision radius of a water molecule r_{molec} can not be neglected for nanometer sized particles. This concept of reduced critical saturations is illustrated in Figure 7.6 for a particle temperature of 140 K. Note that the saturation with respect to hexagonal ice S_{h} is shown on the x-axis and the particle radius on the y-axis. The blue dotted line shows the Kelvin effect for ASW and the blue solid line the Kelvin effect corrected with the H₂O collision radius according to Equation 7.3.1. The difference between both curves highlights the influence of the H₂O collision radius on the critical saturation. For a 2 nm particle, $S_{\text{cr,h}}$ is reduced by 20% from 29 to 23. The relative reduction of $S_{\text{cr,h}}$ increases with decreasing particle radius.

Let us now consider a nucleus as studied in this work. Already several mono-layers of H₂O adsorb on the surface of the nucleus at saturations below $S_{\text{cr,h}}$. The mean desorption energy of a H₂O molecule on these particles is close to the H₂O sublimation

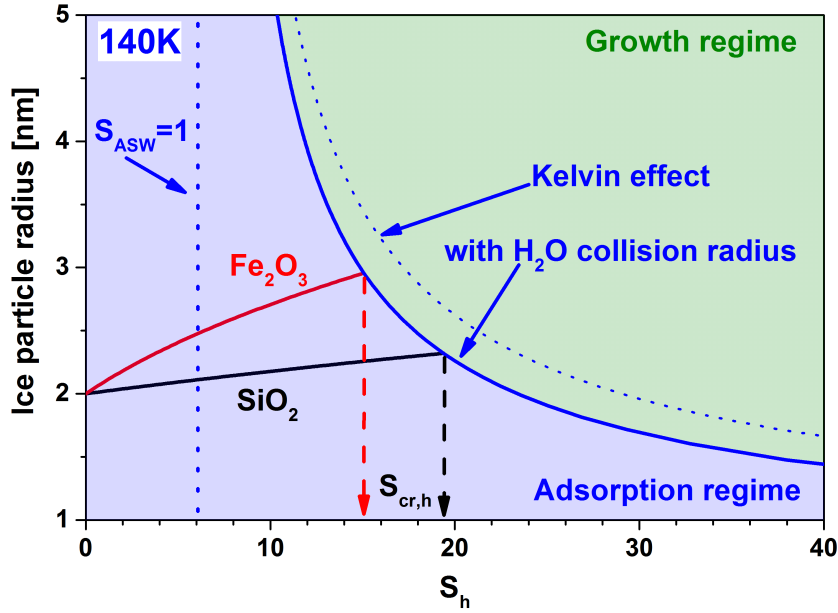


Figure 7.6.: Ice growth activation model: Growth is activated as soon as the particle radius including the amount of adsorbed water molecules is larger than the critical radius according to the Kelvin effect. See text for more details.

energy, i.e. the binding of a H₂O molecule to the nucleus surface is comparable to the binding to an ice particle consisting of ASW. Therefore, the H₂O covered nucleus behaves like an ASW particle. Growth should be activated on the particle for saturations larger than the Kelvin effect calculated for the whole particle size including the number of adsorbed molecules. This activation model is still described by Equation 7.3.1, now using the radius of the particle including the adsorbed water molecules r_{ads} which yields

$$S_{\text{cr}} = S_{\text{eq}}(r_{\text{ads}}, T_p) \cdot \left(\frac{r_{\text{ads}}}{r_{\text{ads}} + r_{\text{molec}}} \right)^2, \text{ with} \quad (7.3.2)$$

$$r_{\text{ads}} = \left(r_p^3 + \frac{3V_{\text{ads}}}{4\pi} \right)^{1/3}, \text{ and}$$

$$V_{\text{ads}} = \frac{4\pi r_p^2 \cdot c_{1,s} \cdot m_{\text{molec}}}{\rho}.$$

m_{molec} is the molecular mass of a water molecule and ρ the density of ASW. The surface concentration of adsorbed molecules $c_{1,s}$ is described by Equation 7.2.2. $c_{1,s}$ and therefore also r_{ads} depend on the water vapor concentration in the environment and

thus on the saturation. Consequently, Equation 7.3.2 has to be solved numerically. The red and black curves in Figure 7.6 plot the calculated particle radii including the number of adsorbed H₂O molecules for an iron oxide and a silica particle. The initial particle radius is 2 nm for both particle materials. The particle size increases with increasing S_h . Growth is activated on the particles as soon as r_{ads} intersects the modified Kelvin effect (solid blue line). Below the critical saturation iron oxide particles adsorb more H₂O molecules than silica particles due to the higher desorption energy. Consequently, iron oxide particles activate growth at lower saturations than silica particles. Critical saturations $S_{cr,h}$ are 15 for iron oxide particles and 19.5 for silica particles with an initial radius of 2 nm. For comparison, Kelvin effect calculations excluding the adsorbed water molecules and the H₂O collision radius result in $S_{cr,h} = 29$.

Figure 7.7 compares the results of the activation model to the measured critical saturations. The results of the activation model at 140 K using the desorption energies from

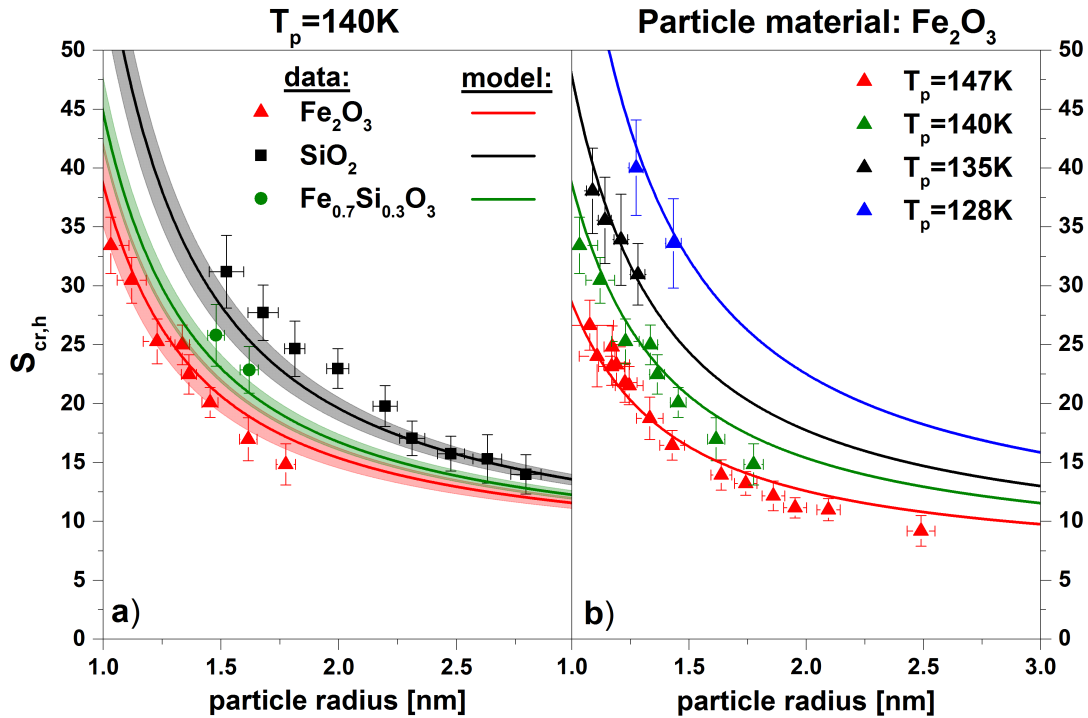


Figure 7.7.: Critical saturations as a function of particle radius. The measurements are compared with the ice activation model (Equation 7.3.2) for various iron silicate compositions (panel a) and for iron oxide at various temperatures (panel b).

7.2.5 are shown in panel a) by the red, green and black lines. The shaded area represents the impact of the uncertainties in desorption energy and particle temperature on the model results. The vapor pressure parameterization for ASW (Equation 6.3.5)

and the surface tension for ASW were used without considering any uncertainty. The activation model is in excellent agreement with the experimental data. Panel b) shows measured critical saturations as a function of particle radius for iron oxide particles at 147, 140, 135, and 128 K (red, green, black, and blue triangles, respectively). The results of the activation model are shown by the red, green, black, and blue lines. The model predicts the measured critical saturations remarkably well.

In summary, no nucleation theory is needed to predict critical saturations S_{cr} . A simple model based on Kelvin effect calculations describes measured critical saturations very well. The model considers the increase of the nucleus size caused by adsorption of H_2O molecules. In addition, it considers the increase of the collision radius of the nucleus by the radius of a H_2O molecule.

7.3.2. Charge effects

The particles studied in this work carry one elementary charge, but no charge effects are needed to explain the observed low critical saturations $S_{cr,h}$ down to particle radii of 1 nm. However, the charge effects introduced in Chapter 4.4 are believed to have a significant influence on critical saturations for particle radii below about 2.5 nm. In brief, three charge effects were proposed. The "dielectric effect" considers charge-dipole interactions reducing the potential energy of a H_2O molecule which is part of the nucleus. The "dipole moment" and the "polarizability" effect on the other hand describe the attraction of gas phase water molecules to the charged nucleus. Accordingly, the collision rate of H_2O molecules with a charged nucleus is higher compared to a neutral nucleus, which causes a reduction of the critical saturation. The activation model introduced above can be modified to consider charge effects. The Kelvin term $S_{eq}(r_{ads}, T_p)$ in Equation 7.3.1 has to be exchanged with the Kelvin effect including charge effects (Equation 4.4.6) using r_{ads} instead of the particle radius r .

The red triangles in Figure 7.8 show the measured critical saturations for iron oxide particles at 140 K as a function of the initial particle radius. The black solid line represents $S_{cr,h}$ calculations using the activation model with the mean desorption energy determined for iron oxide particles, but without charge effects. The blue dashed line shows the results of the activation model considering solely the dielectric effect. The calculations considering this effect are essentially identical to calculations for neutral particles down to particle radii of 1 nm, which are the smallest particles studied in this work. Thus, no conclusions about the applicability of the dielectric effect can be drawn. The influence of the charge increases with decreasing particle radius. Nevertheless, critical saturations are predicted to be reduced by less than 50 % for a particle radius of 0.5 nm. The dielectric effect is supposed to reduce critical saturations to a much higher extend (compare to Figure 4.5). This weaker charge effect in the activation model is explained by the increase of the particle size due to the adsorption of H_2O molecules.

Activation model calculations adding the dipole moment and the polarizability effect are represented by the green dotted line. The results are in striking disagreement to

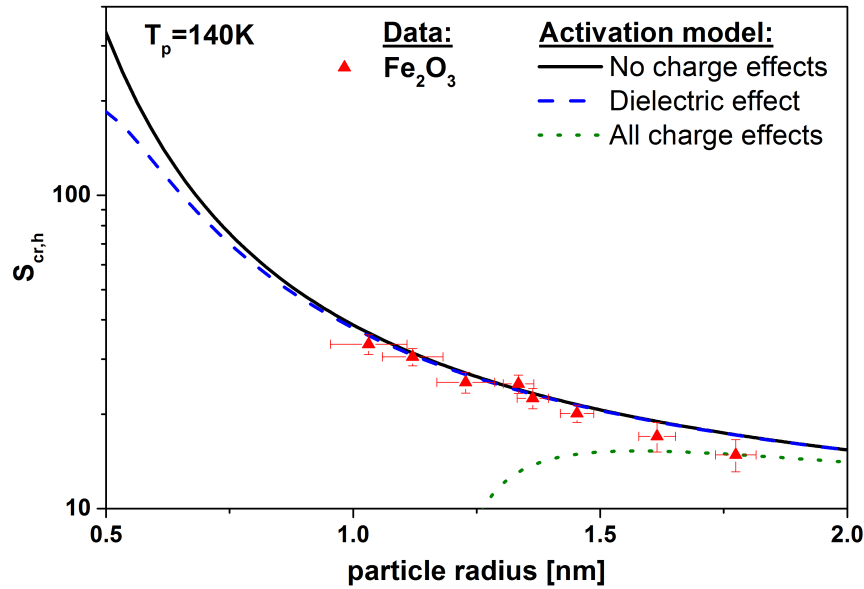


Figure 7.8.: Analysis of charge effects. Red triangles are measured critical saturations $S_{cr,h}$ for iron oxide particles at 140 K. They are compared to calculations using the activation model developed in this work without charge effects (black solid line), including solely the dielectric effect (blue dashed line) and all charge effects (green dotted line).

the data for iron oxide particles. Thus, the dipole moment and the polarizability effect seem to be not applicable and should be neglected. This conclusion is supported by a study of [Zamith et al. \[2013\]](#). They measured the H₂O attachment cross section of protonated and de-protonated water ice clusters. An attraction of water molecules causing an increased H₂O collision rate with the cluster should be seen in their data. However, down to 1 nm in radius, they did not observe a significant difference to measurements conducted with neutral water ice clusters by [Lengyel et al. \[2012\]](#).

7.3.3. Onset conditions for PMC formation

In general, two different approaches are in use by the PMC science community to predict onset conditions of PMC formation. (1) ice particle formation is activated as soon as the saturation exceeds the Kelvin effect [e.g. [Berger and Luebken, 2015](#); [Schmidt et al., 2017](#)], or (2) ice particle formation is described using the surface diffusion approach of Classical Nucleation Theory (CNT) [e.g. [Rapp and Thomas, 2006](#); [Bardeen et al., 2010](#); [Asmus et al., 2014](#)]. The two approaches are introduced in detail in Chapter 4. In both approaches, deposition of hexagonal ice I_h is assumed. The gray shaded area in Figure 7.9 shows the variation of critical saturations $S_{cr,h}$ calculated with these approaches for a typical summer mesopause temperature of 120 K (see Chapter 2.3). This illustration reflects the tremendously large uncertainty of the current scientific

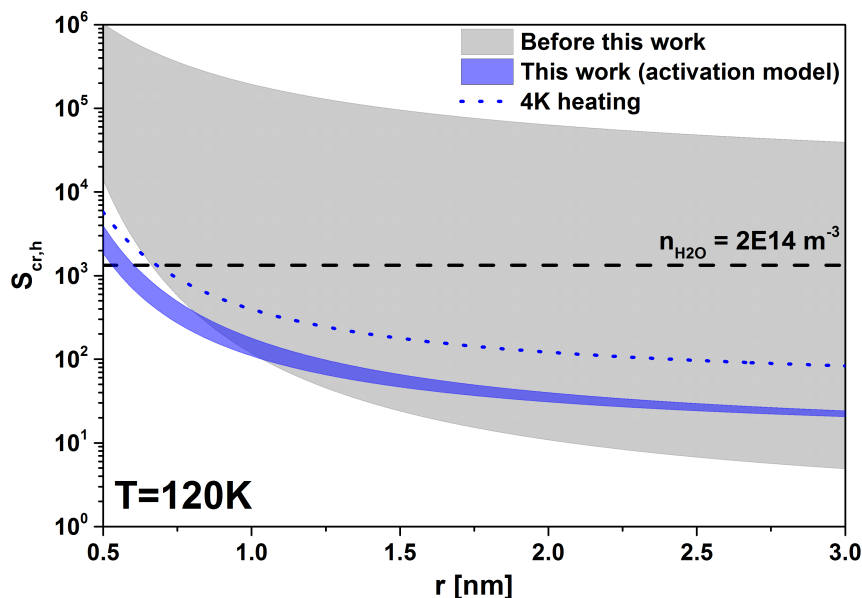


Figure 7.9.: Critical saturations $S_{cr,h}$ as a function of particle radius at a typical summer mesopause temperature of 120 K. The gray shaded area reflects the uncertainty in critical saturations according to the current scientific consensus in predicting onset conditions. The blue shaded area are results from the activation model developed in this work. For comparison, calculations considering a nuclei heating of 4 K and a typical summer mesopause water vapor concentration of $2 \times 10^{14} \text{ m}^{-3}$ are shown by the blue dotted and black dashed line, respectively.

consensus in predicting onset conditions for PMC formation.

The blue shaded area in Figure 7.9 shows critical saturations according the activation model. Here, the desorption energy was varied between the experimental results obtained above for silica and iron oxide particles. These values are a good estimate of the desorption energy for MSPs since they are expected to be composed of hydrophilic materials containing Fe, Si, Mg and O [e.g. Vondrak et al., 2008; Plane et al., 2015; Rapp et al., 2012; Hervig et al., 2012]. The results significantly reduce the uncertainty in predicting critical saturations. The uncertainty is reduced from several orders of magnitude to below a factor of 2. The majority of MSPs available for the formation of PMCs is below 1 nm in radius [Megner et al., 2008b; Gumbel and Megner, 2009]. Critical saturations are for such particle sizes lower than the lower limit according to the current scientific consensus. This effect is caused by the adsorption of H_2O molecules which significantly increases the effective particle size, especially for small particles below $r=1$ nm.

The black dashed line represents a typical H_2O concentration in the summer mesopause ($n_{\text{H}_2\text{O}} = 2 \times 10^{14} \text{ m}^{-3}$). According to the results of this work, particles larger than $r=0.6$ nm serve as nuclei at typical summer mesopause conditions. A MSP concentration of about 1000 cm^{-3} is expected to be present in the summer mesopause with

$r > 0.6$ nm (compare Figure 2.4). PMCs have mean ice particle concentrations in the order of 100 cm^{-3} [e.g. Kiliiani et al., 2015; Bardeen et al., 2010]. Thus, the nucleus concentration available for ice particle growth at typical conditions is sufficient to explain the formation of PMCs. This supports the key role of MSPs in the formation process of PMCs.

Recently, Asmus et al. [2014] proposed that MSPs might heat up with respect to the temperature of the environment by absorption of solar radiation. They proposed that the heating of the particles significantly alters critical saturations. The following estimates the maximum influence of MSP heating on critical saturations. Asmus et al. [2014] found out, that the heating of particles linearly increases with the iron content of the MSP material. For a $r = 1.1$ nm particle they calculated a maximum heating of 8 K assuming FeO particles. In their calculation, they used a thermal accommodation coefficient of 0.5, which probably is an underestimation. MSPs in the mesopause are covered with H₂O molecules and the thermal accommodation coefficient of air on water and silica particles is rather close to one [Fung and Tang, 1988; Ganta et al., 2011]. Considering a value of one, a maximum temperature increase of 4 K is estimated for a $r = 1.1$ nm particle in the summer mesopause. Critical saturations $S_{\text{cr,h}}(120 \text{ K})$ were calculated with the activation model using the desorption energy of iron oxide and assuming a heating of the particle of 4 K. The result is shown by the blue dotted line in Figure 7.9. According to this, critical saturations increase by a factor of about 2.5. These calculations however, are an absolute upper limit of the influence of particle heating on critical saturations for two reasons. First, they represent particles composed of FeO, the material which is expected to heat up the most. Second, the heating of the particles increases with particle size [Asmus et al., 2014]. The maximum heating of the majority of MSPs available for PMC formation ($r < 1$ nm) should therefore be less than 4 K. Consequently, a severe influence of particle heating on onset conditions for PMC formation is not expected to be the case.

7.4. Conclusions

Adsorption and nucleation experiments of H₂O on nanometer-sized silica (SiO₂), iron oxide (Fe₂O₃) and mixed iron silicate (Fe_xSi_{1-x}O₃) particles were performed. The particles serve as analogues for Meteoric Smoke Particles (MSPs). Measurements were conducted at temperatures between 128 and 155 K, which are representative for the terrestrial mesopause. The results of the measurements aim to answer the second question formulated in the introduction:

What are onset conditions for PMC formation?

Although ASW deposits and the saturation vapor pressure for this ice phase is significantly higher than for hexagonal ice, particle growth activates at unexpectedly low critical saturations $S_{\text{cr,h}}$. This observation is explained by considering that MSPs adsorb up to several mono-layers of H₂O before ice growth sets in. These adsorbed H₂O

molecules significantly increase the size of the nucleus. Growth sets in for saturations larger than the Kelvin effect for ASW considering the whole particle radius including the adsorbed H₂O molecules. This activation model is presented in Equation 7.3.2. The number of adsorbed molecules $c_{1,s}$ can be calculated with Equation 7.2.2 and depends on the desorption energy of the nucleus material $\Delta F_{\text{des,pl}}$. Measurements of the number of adsorbed H₂O molecules were used to determine $\Delta F_{\text{des,pl}}$ of the MSP analogues. In this case, $\Delta F_{\text{des,pl}}$ reflects the mean binding energy of H₂O molecules on the surface of the particles for coverages above 0.5 mono-layers. The results for $\Delta F_{\text{des,pl}}$ are in very good agreement with literature data and they are presented in Equation 7.2.5. All investigated materials are hydrophilic and the desorption energies are very close to the sublimation energy of H₂O. A parameterization for the desorption energy of MSPs as function of the iron content is given in Equation 7.2.6.

There is no influence of the particle charge on critical saturations down to particle radii of at least 1 nm. An absence of charge effects in the investigated particle size range is an intriguing results, which was unexpected. A potential influence of the particle charge on critical saturations needs further investigation.

The activation model developed in this work reduces uncertainties in predicting critical saturations from several orders of magnitude to less than a factor of 2. It predicts that MSPs down to about 0.6 nm in radius activate ice particle growth at typical summer mesopause conditions ($T_p=120$ K and $n_{\text{H}_2\text{O}}=2 \times 10^{14} \text{ m}^{-3}$). This result supports the importance of MSPs as condensation nuclei for PMCs. In addition, a heating of MSPs in the summer mesopause only marginally influences onset conditions for PMC formation.

The activation model developed in this work can be used in future model studies to compare model results with observations. In this way, other uncertainties involved in PMC formation may also be constrained. [Wilms et al. \[2016\]](#) showed for example that the vertical wind as well as the the size dependent concentration profile of MSPs strongly influence model results on PMC properties.

8. CO₂ nucleation experiments*

This chapter reports on adsorption and nucleation experiments of CO₂ on nanometer-sized silica (SiO₂) and iron oxide (Fe₂O₃) particles using the MICE-TRAPS setup. The microphysical nucleation process in the Martian mesosphere is described by classical heterogeneous nucleation induced by surface diffusion (CNT). This approach assumes that the adsorbed CO₂ molecules diffuse on the surface of the particle, collide and combine to clusters of different sizes. These clusters may eventually reach the critical size resulting in a nucleation event. Consequently, the concentration of adsorbed molecules $c_{1,s}$ (Equation 7.2.2) on the surface of the nucleus is a critical parameter describing nucleation. The concentration of adsorbed molecules mainly depends on the desorption energy $\Delta F_{\text{des,pl}}$, which is a characteristic property of the nucleus material. This parameter and the contact parameter m are the main two parameters which govern nucleation rates in classical nucleation theory. The aim of the CO₂ nucleation experiments is to determine these two parameters and respond to the third question formulated in the introduction:

What are onset conditions for CO₂ ice cloud formation?

8.1. Methods

Singly-charged iron oxide and silica particles were exposed to a controlled supersaturation of CO₂ at temperatures between 63 and 74 K. In each individual experiment MICE was filled with particles of a well known size. The time resolved mass of the trapped particles was then periodically recorded by extracting small samples of the trapped particle population into the TOF mass spectrometer. Figure 8.1 shows measurements of CO₂ growth on silica particles of 2.5 nm initial radius for three different particle temperatures. The dotted lines are for guidance of the eye. For this series of measurements the CO₂ concentration is $n_{\text{CO}_2} = 3.7 \times 10^{15} \text{ m}^{-3}$. The particle temperature and with it the saturation differ between the individual measurements. Three different growth modes can be distinguished.

(1) Curve a) corresponds to a situation where the saturation is too low to activate nucleation. Only adsorption of CO₂ molecules on the particle surface is observed. Note that no nucleation occurs for a particle temperature of 68 K and a saturation as high as 1000. These conditions are already highly supersaturated even considering the

*In part based on [Nachbar et al., 2016]

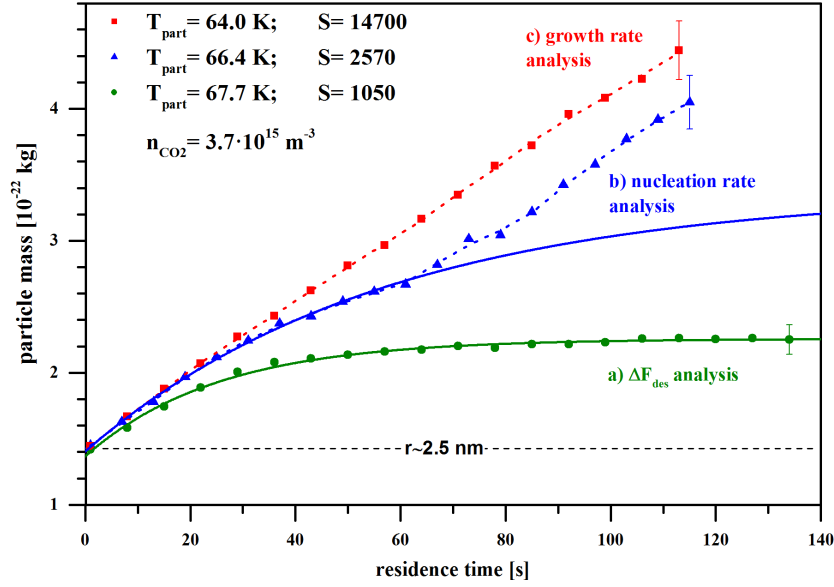


Figure 8.1.: Series of CO₂ deposition measurements on 2.5 nm silica particles at constant CO₂ concentration. By decreasing temperature, and thus increasing saturation, the deposition regime can be changed from adsorption only (curve a) to delayed nucleation and subsequent growth (curve b) and immediate growth (curve c). Figure adapted from Nachbar et al. [2016].

curvature of the particles (Kelvin effect). S_{eq} at 68 K is 19 for a 2.5 nm particle. Here, the amount of adsorbed CO₂ molecules increases with time until an equilibrium of adsorbing and desorbing is reached (Equation 7.2.2). The amount of adsorbed molecules in equilibrium was determined in the same way as for H₂O (Chapter 7). Equation 7.1.1 was fitted to the data to determine the mass of adsorbed CO₂ molecules in equilibrium (m_{ads}). The fit is represented by the solid green line in Figure 8.1, which yields $m_{\text{ads}} = 8.9 \times 10^{-23}$ kg or about 1200 CO₂ molecules. The surface concentration of adsorbed CO₂ molecules $c_{1,s}$ was calculated by dividing the amount of adsorbed molecules by the surface area of the particle. The size dependent desorption energy ΔF_{des} was calculated with Equation 7.1.2 and a linear fit to the data then determines the desorption energy $\Delta F_{\text{des,pl}}$ of the material for a planar surface.

(2) At slightly lower temperature (curve b, 66.4 K and $S \approx 2600$) the saturation is high enough to activate nucleation followed by growth. The concentration of adsorbed molecules on the surface of the nucleus governs nucleation rates with a $c_{1,s}^2$ dependency (Equation 4.3.1). In classical nucleation theory $c_{1,s}$ is calculated by assuming a steady state equilibrium. In contrast, in the experiments presented here the trapped nanoparticles are not in steady state initially as they are not covered with CO₂, but acquire CO₂ molecules over time. The actual concentration of adsorbed CO₂ molecules on the particle surface is a function of residence time in MICE. Therefore, the nucleation

rate is a function of time in the experiments. The nucleation rate increases during the adsorption process until either the critical surface concentration to induce nucleation or the equilibrium surface concentration is reached. This process is visible in curve b). The mass growth curve initially follows a simple exponential growth (blue line). At 61 s residence time, it diverges from the adsorption mode behavior. Such a deviation indicates nucleation occurring on the trapped particles, enabling the transition to the mass growth regime. The critical surface concentration triggering nucleation is inferred from the total mass of adsorbed CO₂ molecules at the transition point at 61 s. Here, $m_{\text{ads}} = 1.26 \times 10^{-22}$ kg or about 1700 CO₂ molecules. It has to be noted that an increase in the standard deviation of the measured particle mass distributions of curve b) is not observed. This leads to the conclusion that nucleation-induced broadening of the particle mass distribution is insignificant. Nucleation on the majority of the particles sets in within one experimental time step. Consequently, the nucleation rate at the critical surface concentration is on the order of 1/(time step) which in this case is 1/(6 s). The nucleation rate, the critical surface concentration, the particle radius, the temperature, and the ambient CO₂ concentration can be used to calculate the contact parameter m by numerically solving Equation 4.3.1. This procedure of estimating the contact parameter is justified by the fact that by solving Equation 4.3.1 the contact parameter is only a weak function of the nucleation rate, i.e. changing the nucleation rate by one order of magnitude results in a 1% change of m . An additional error of 1% is added to Δm in order to account for errors made in estimating the nucleation rate.

(3) At the lowest particle temperature and hence highest saturation in Figure 8.1 (curve c, 64 K and $S \approx 15000$), the transition to the growth regime is not visible anymore. At such high saturation, nucleation already occurs during the adsorption process, i.e. in the first steep section of the curve. The rate of mass accretion in this first part of the growth is limited only by the supply of molecules from the vapor phase. Growth at such conditions were used to determine the saturation vapor pressure above the ice covered surfaces in MICE. The results of these measurements are presented in Chapter 6. Note that after nucleation in curve b), the particles grow with the same rate as for conditions represented by curve c). Here, the conditions for both curves are highly supersaturated so that the CO₂ flux emitted by the particles is insignificant. Growth rates only dependent on the particle size and the incoming CO₂ flux density which are identical for both runs.

MICE is able to produce CO₂ supersaturated conditions in the range between 60 and 90 K [Duft et al., 2015]. However, high supersaturations are required to onset nucleation. Consequently, the range of particle temperatures at which nucleation and growth was actually examined, was limited to temperatures between 63 and 74 K. These temperatures are close to the temperature range of interest in the Martian mesosphere (70 – 120 K). Slight temperature gradients across MICE and a measurement uncertainty of 0.1 K result in a particle temperature uncertainty of 0.4 K and an uncertainty of the CO₂ concentration of 10%. Due to the strong dependence of the

saturation vapor pressure on temperature, the relative uncertainty in S is 25 to 30 %.

Nachbar et al. [2016] refer to the CO₂ vapor pressure parameterization of James et al. [1992] and a constant CO₂ ice density of 1.5 g cm^{-3} [Luna et al., 2009] in the data analysis. Chapter 6 shows on the basis of a literature search and CO₂ vapor pressure measurements performed with MICE-TRAPS, that the CO₂ vapor pressure parameterization of Meyers and Van Dusen [1933] should be used.

Recently, Mangan et al. [2017] deposited CO₂ ice at 80 and 110 K and studied the CO₂ ice density between 80 and 130 K using X-ray diffraction. They provide a parameterization for the CO₂ ice density which is given in Table B.1.

I reanalyzed the data presented in Nachbar et al. [2016] with the vapor pressure parameterization from Meyers and Van Dusen [1933] and the CO₂ ice density parameterization from Mangan et al. [2017].

8.2. Results

8.2.1. Desorption energy

CO₂ adsorption at saturations below the critical saturation for nucleation was investigated on silica particles with radii between 2.4 and 3.2 nm, and on iron oxide particles with radii between 1.8 and 2.2 nm. The particle temperature was varied between 66 and 73 K. CO₂ concentrations were varied between 2×10^{15} and $3 \times 10^{16} \text{ m}^{-3}$ which corresponds to saturations between 400 and 1500.

The desorption energy was determined from the measured adsorbed mass of CO₂ molecules in equilibrium using Equation 7.1.2. This equation determines the effective desorption energy on the particles which is reduced with respect to the desorption energy $\Delta F_{\text{des,pl}}$ on a planar surface due to the curvature of the particles. The determined desorption energies for silica and iron oxide particles are shown in Figure 8.2 by the open black squares and open red triangles as a function of $1/r$. A weak dependency of the desorption energy on particle size is apparent in the data. This is due to a reduction of the binding energy of the adsorbed CO₂ molecules with decreasing particle size. The intercept of a linear fit to the data is the desorption energy for a planar surface and the slope reflects an effective surface tension σ_{des} . σ_{des} describes the influence of the particle size on the binding energy of an adsorbed CO₂ molecule. A linear fit to the data is shown by the black dotted line. The intercept yields $\Delta F_{\text{des,pl}} = (3.28 \pm 0.03) \cdot 10^{-20} \text{ J/molec}$, which is shown by the blue dashed line in Figure 8.2 with the shaded shaded area representing the uncertainty. This value is well below the sublimation energy of CO₂ for these conditions which is approximately $4.65 \times 10^{-20} \text{ J/molec}$ [Giauque and Egan, 1937]. The difference between the desorption energy and the sublimation energy indicates, that the CO₂ molecules on the nanoparticle surface are not represented by bulk properties of CO₂, unlike in the case of H₂O adsorption (Chapter 7). In particular, the representative surface tension is not represented by the surface tension of CO₂ ice. The effective surface tension

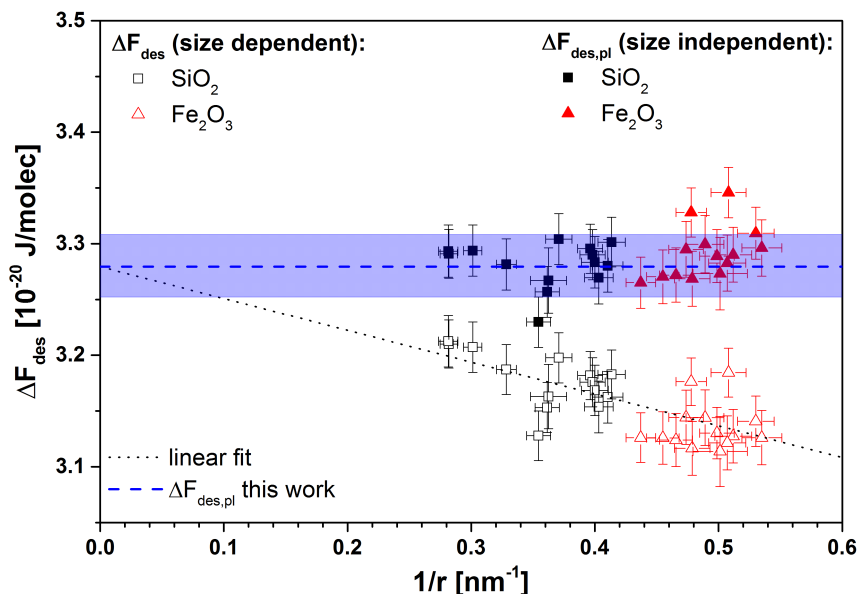


Figure 8.2.: CO₂ desorption energy as a function of $1/r$. The black squares show the results obtained for silica particles and red triangles the results obtained for iron oxide particles. The open data points show the results analyzed with Equation 7.1.2 and the black dotted line is a linear fit to the data. The filled data points show the particle size corrected values according to Equation 7.2.3, which represent the CO₂ desorption energy of the particle material for a planar surface. The horizontal blue dashed line is the mean value of the desorption energy with the shaded interval of uncertainty.

can be determined from the slope of the linear fit to the ΔF_{des} data. The fit results in $\sigma_{\text{des}} = (0.033 \pm 0.006) \text{ Nm}^{-1}$, which is smaller than the surface tension of CO₂ ice (0.08 Nm^{-1} [Wood, 1999]). The filled black squares and red triangles show the data for silica and iron oxide particles analyzed with Equation 7.2.3 and σ_{des} from the fit. The desorption energy is independent of the two nuclei materials within the uncertainty of the experiment.

8.2.2. Contact parameter

Experiments to determine the nucleation rate and the contact parameter were conducted with silica particles with initial radii between 2.4 and 3.1 nm, and with iron oxide particles with initial radii between 1.9 and 2.1 nm. The CO₂ concentration varied between 8×10^{14} and $4 \times 10^{17} \text{ m}^{-3}$ at particle temperatures between 64 and 73 K. The contact parameter m was calculated by numerically solving Equation 4.3.1 using the estimated nucleation rate, the measured critical surface concentration, the particle radius, the temperature, and the ambient CO₂ concentration. The results are shown in Figure 8.3 as a function of particle temperature. Since the nucleation rate is

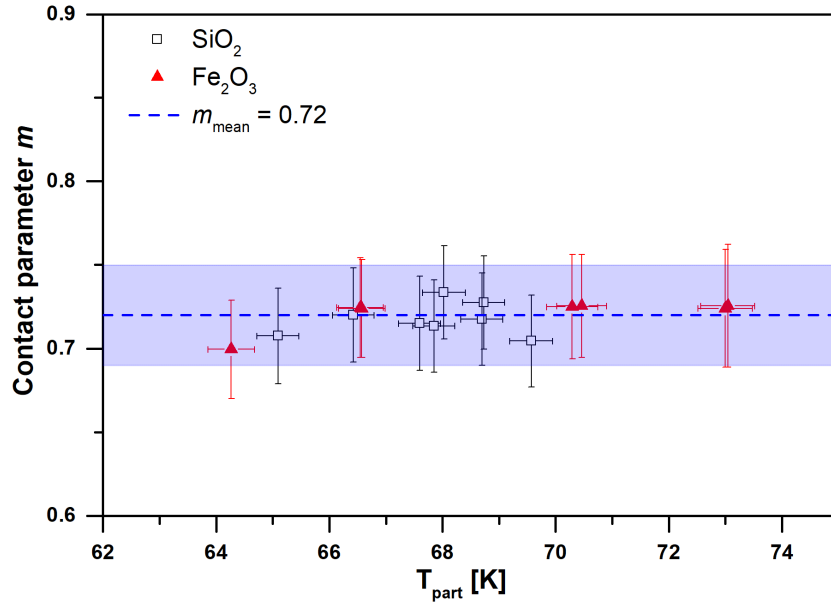


Figure 8.3.: CO₂ contact parameter as a function of particle temperature for iron oxide particles (red triangles) and silica particles (open black squares). The blue dashed line represents the determined mean value of 0.72 with the shaded interval representing the uncertainty ($\Delta m = 0.03$).

very sensitive to the particle temperature, the error of 0.4 K in particle temperature is mainly responsible for the uncertainty in m . The contact parameter m is the same for both particle materials. No effect of the particle size on the contact parameters is present. There is no apparent trend of the contact parameter with particle temperature. However, a possible trend of the contact parameter with temperature might be obscured by the uncertainty of the data in the small temperature range of only 10 K. The trend of the contact parameter with temperature is discussed in the next section. The mean value of m between 64 and 73 K is 0.72 ± 0.03 .

8.3. Discussion

8.3.1. Desorption energy and contact parameter

Desorption energy

The CO₂ desorption energy $\Delta F_{\text{des,pl}} = (3.28 \pm 0.03) \cdot 10^{-20}$ J/molec is essentially identical for iron oxide and silica particles. This experimental value for $\Delta F_{\text{des,pl}}$ is in good agreement with $3.25 \cdot 10^{-20}$ J/molec determined for Mauna-Kea palagonite [Zent and Quinn, 1995], which is regarded as a terrestrial analogue for Martian Dust Particles (MDPs). A high percentage of the composition of MDPs is silica and iron oxide, the

same materials used in this work as MSP analogues. Palagonite mainly consists of silica ($\approx 45\%$), Al_2O_3 ($\approx 20\%$) and Fe_2O_3 ($\approx 15\%$) [Morris et al., 2000]. Besides MSPs and MDPs, dirty ice particles may serve as nuclei in the mesosphere of Mars [Plane et al., 2018]. The desorption energy of CO_2 on H_2O ice is approximately 3.5×10^{-20} J/molec [Andersson et al., 2004], which is very close to the values for MSPs and MDPs. All these materials exhibit a low CO_2 affinity since the desorption energies are smaller than the heat of sublimation for CO_2 ice which is approximately 4.65×10^{-20} J/molec in the temperature range under investigation [Giauque and Egan, 1937].

Contact parameter

The contact parameter $m = 0.72 \pm 0.03$ is identical for iron oxide and silica particles between 64 and 73 K. The contact parameter is connected to the interfacial energy between the CO_2 ice germ and the nucleus. In general, a difference in the desorption energy between two materials likely reflects in the contact parameters. Materials with higher desorption energies are expected to exhibit a higher contact parameter, i.e. a smaller contact angle. Since the desorption energy of MDPs is essentially identical to the one determined here for MSPs, the contact parameter for MDPs must be close to 0.72. However, the contact parameter measured in the present study differs significantly from 0.95 determined by Glandorf et al. [2002] between 130 and 140 K for a water ice covered silicon surface. From the discussion in Glandorf et al. [2002], the uncertainty in their result is approximately 2%, which is too small to explain the apparent discrepancy. The discrepancy may be explained in two ways.

(1) The most obvious difference is that Glandorf et al. [2002] covered their surface with water-ice before introducing CO_2 . If the difference is caused by the substrate material, then the high contact parameter of 0.95 should only be applicable to dirty ice particles or MDPs and MSPs which have acquired layers of water ice prior to the nucleation of CO_2 . However, the CO_2 desorption energy on H_2O ice (3.5×10^{-20} J/molec [Andersson et al., 2004]) is very close to the desorption energy for MDPs and MSPs (3.25×10^{-20} and 3.28×10^{-20} J/molec) which makes a large difference between the contact parameters of the three materials unlikely.

(2) Glandorf et al. [2002] determined m at temperatures between 130 and 140 K, so a temperature dependency of m may provide another explanation. A temperature dependency of the contact parameter is reported for water ice [Fortin et al., 2003; Trainer et al., 2009; Iraci et al., 2010; Phebus et al., 2011; Thomson et al., 2015]. In order to explain the difference between the results of this work and Glandorf et al. [2002], a linear dependence of m on T should have a slope of approximately 0.003 K^{-1} over the temperature span encompassing the ranges of both experiments (60 to 140 K). Within the 10 K temperature range of the measurements in this work and in Glandorf et al. [2002], this corresponds to a change in m of 0.03 which is within the uncertainty limits of either experiment. Consequently, a temperature dependence of m can explain the difference between the values found in both experiments. This is discussed in more detail below.

Possible temperature dependency of the contact parameter m

Figure 8.4 shows experimental data for the contact parameter as a function of temperature. The red squares are the combined results from the CO₂ nucleation experiments

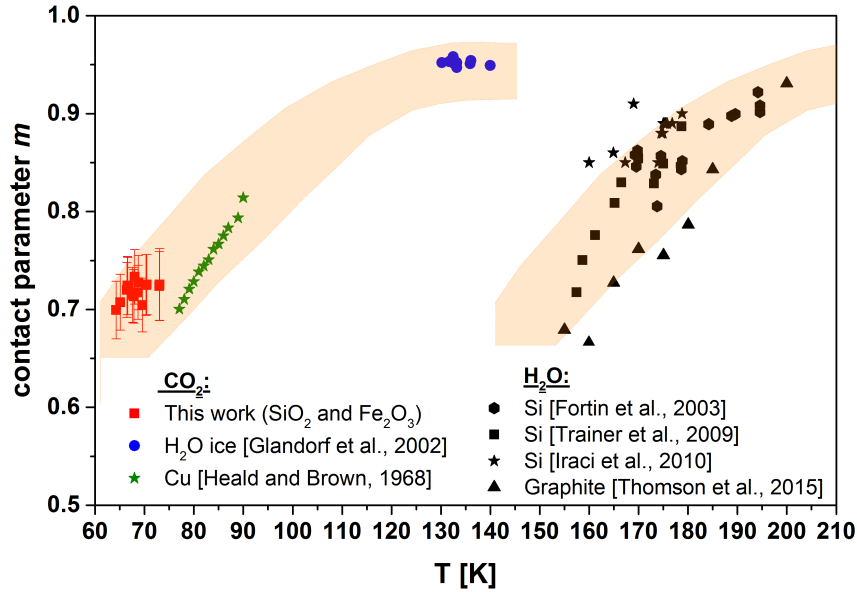


Figure 8.4.: Comparison of experimentally determined contact parameters m for CO₂ and H₂O as a function of temperature. For H₂O data, only materials with a low water affinity are shown here. The orange shaded areas serve as guidance to the eye.

on silica and iron oxide particles between 64 and 73 K. The blue dots represent the data for CO₂ nucleation on H₂O ice obtained by Glandorf et al. [2002]. Heald and Brown [1968] report critical saturations for CO₂ nucleation on a planar polished copper surface between 77 and 90 K using a molecular beam chamber. They found critical saturations increasing with decreasing temperature. Their critical saturation data (Figure 11 in their work) was digitized and the nucleation rate equation (Equation 4.3.1) for a planar surface was numerically solved for the contact parameter m . Here, the CO₂ desorption energy for copper (3×10^{-20} J/molec [Chinchen et al., 1987]) was used. Note that the desorption energy for copper is very close to the desorption energy for MSPs. Therefore it is reasonable to assume that the contact parameters for the two materials behave similarly. The results are shown by the green stars in Figure 8.4. The calculations show that the contact parameter of CO₂ on copper is indeed close to the results found here for MSPs. However, the contact parameters calculated from the S_{cr} data of Heald and Brown [1968] increases with temperature which indicates that there might be a temperature dependence in m connecting the data below 90 K to the data obtained on H₂O ice between 130 and 140 K. The orange shaded area serves as guidance to the eye and illustrates the apparent increasing contact parameter with temperature.

A temperature dependent contact parameter is observed for H₂O ice [Fortin et al., 2003; Trainer et al., 2009; Iraci et al., 2010; Phebus et al., 2011; Thomson et al., 2015]. For comparison, the black data points in Figure 8.4 show experimental data for the H₂O contact parameter on silicon and graphite. These two surfaces were chosen because their H₂O desorption energies are smaller than the sublimation energy [Ranke, 1996; Ranke and Xing, 1997; Thomson et al., 2015]. Below 200 K, the contact parameter data decreases with decreasing temperature. The slope is comparable to the slope of the CO₂ data. The orange shaded area overlaying with the data for H₂O serves as a guidance to the eye. It was produced by shifting the orange shaded area for CO₂ by 80 K.

Figure 8.5 shows all data for the contact parameter plotted against the experimentally determined vapor pressure at which nucleation and thus growth sets in. Surprisingly,

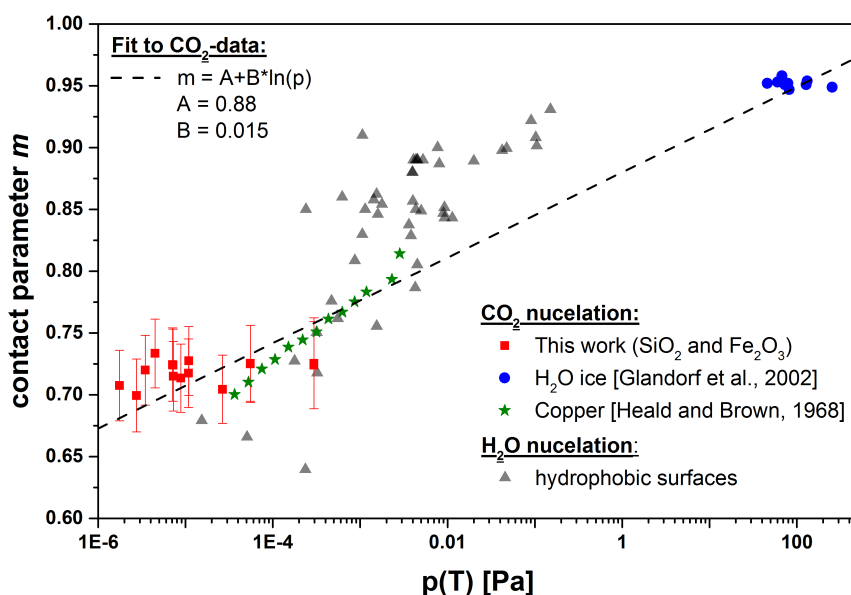


Figure 8.5.: Contact parameter as a function of the CO₂ vapor pressure at nucleation. A fit to the CO₂ data is represented by the dashed black curve. For comparison, the gray triangles represent H₂O contact parameters obtained on materials with a low water affinity.

the data for H₂O and CO₂, which were spread out when plotted against the temperature, now collapse onto the same region. This indicates, that the contact parameter may not depend on temperature, but on vapor pressure. However, the contact parameter depends on the surface energy of the nucleus/air, nucleus/ice and ice/air interface (Equation 4.3.7). These values should not be affected by the vapor pressure of the nucleating species. The increase of the contact parameters with rising temperature for CO₂ and H₂O at comparable nucleation vapor pressures indicates, that there might

be an underlying fundamental principle in the heterogeneous nucleation process which is not considered in CNT.

CO₂ ice cloud formation in the Martian mesosphere occurs at temperatures between 70 and 120 K for CO₂ vapor pressures between 1×10^{-6} and 1 Pa. The contact parameter has to be parameterized for these conditions when using CNT to derive onset conditions for cloud formation in the Martian mesosphere. In order to provide a rough estimate for the contact parameter at these conditions, the apparent trend of the CO₂ data with vapor pressure was fitted as follows:

$$\begin{aligned} m(p_{CO_2}) &= A + B \cdot \ln(p_{CO_2}) & (8.3.1) \\ A &= 0.882 \pm 0.004 \\ B &= 0.0150 \pm 0.0004 \end{aligned}$$

The result of the fitting procedure is shown by the black dashed line in Figure 8.5. It reasonably well combines all available data for CO₂ nucleation. Combining all contact parameter data available for CO₂ is justified by the fact that the CO₂ desorption energies on the different substrate materials are very similar. However, for a more reliable conclusion, additional CO₂ nucleation studies between 90 and 130 K or experiments with MSP or MDP analogues at the temperature range of the experiments of Glandorf et al. [2002] are desirable. Note that due to the nature of the linear fit, m becomes greater than 1 for pressures above 1 kPa, which contradicts the definition of m . However, Equation 8.3.1 is only intended to give a rough estimate for the contact parameter at mesospheric conditions with CO₂ vapor pressures between 1×10^{-6} and 1 Pa.

8.3.2. Onset conditions for cloud formation

The black line in Figure 8.6 represents the current scientific consensus of activation temperature T_{act} for CO₂ ice cloud formation with altitude as discussed in Chapter 3.3. These values were calculated for a typical CO₂ concentration profile with altitude by numerically solving the nucleation rate equation (Equation 4.3.1) for the temperature at which the nucleation rate per particle reaches 0.1 s^{-1} . This procedure is justified since nucleation rates react very sensitive to changes in temperature. At constant CO₂ concentration and nuclei size, a temperature change of only 1 K causes a variation of the nucleation rate by 3 orders of magnitude. Hence, the temperature at which ice particles form is well defined for a constant CO₂ concentration. For the desorption energy and contact parameter, the numerical values typically assumed by the scientific community were used ($\Delta F_{des,pl} = 3.25 \times 10^{-20} \text{ J/molec}$ and $m=0.95$ [e.g. Colaprete et al., 2003; Määttänen et al., 2005; Listowski et al., 2014]). In addition, calculations from Listowski et al. [2014] were used estimate a typical particle size profile with height. Listowski et al. [2014] estimate the altitude dependent upper and lower limit of the particle size in the Martian mesosphere by calculating the equilibrium between sedimentation and vertical mixing using a diffusion constant of $1000 \text{ m}^2\text{s}^{-1}$ and $100 \text{ m}^2\text{s}^{-1}$.

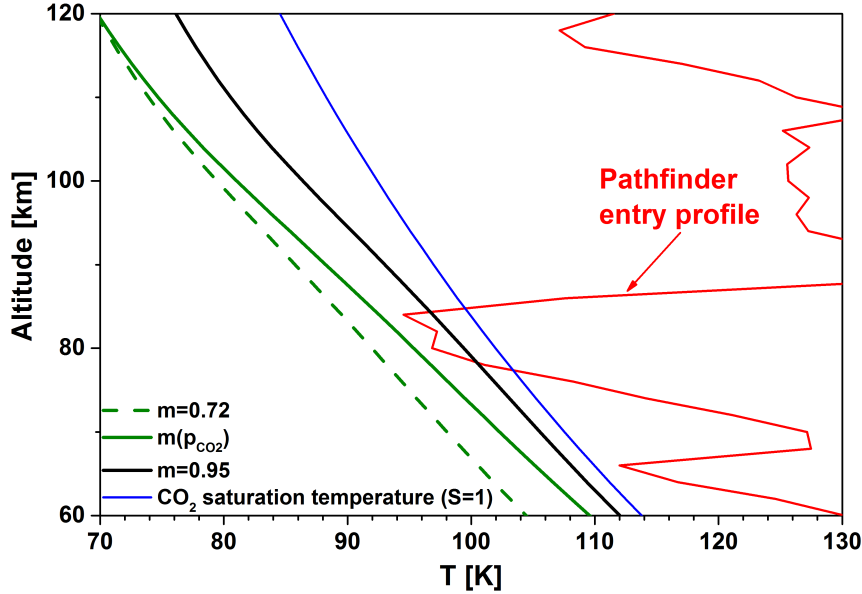


Figure 8.6.: Activation temperature T_{act} as a function of altitude. The black curve shows CNT calculations representing the current scientific consensus. For comparison, the blue curve shows the saturation temperature and the red curve shows the temperature measured by Pathfinder while descending through the mesosphere [Magalhaes et al., 1999]. The solid and dashed green curves represent activation temperatures calculated with a CO_2 vapor pressure dependent contact parameter (Equation 8.3.1) and $m=0.72$.

The range of their equilibrium profiles agrees well with typical dust mass mixing ratios during the main occurrence season of mesospheric CO_2 clouds. Here, the mean values of these upper and lower limits were used.

According to the current scientific consensus (black curve), activation temperatures T_{act} are 2 to 8 K below the saturation temperature (blue curve). For comparison, the red curve shows the temperature profile measured by Pathfinder while descending through the mesosphere [Magalhaes et al., 1999]. This temperature profile represents a rather common profile with temperatures falling below saturation temperature at an altitude of about 80 km [Forget et al., 2009]. According to this temperature profile and the current scientific consensus, CO_2 clouds would form regularly. This stands in contrast to observations. No clouds appear during most of the nights with temperatures falling below the saturation temperature [Forget et al., 2009].

If the contact parameter is independent on temperature, but material dependent, then $m=0.95$ would only be valid for H_2O ice particles. MDPs and MSPs would be represented by $m=0.72$ as determined in this work. Activation temperatures as a function of altitude calculated with this contact parameter are shown by the green dashed line, which results in colder activation temperatures than for the reference case. Activation temperatures in this case would be between 9 and 15 K below the saturation tempera-

ture. Here, no clouds would form for the temperature profile measured by Pathfinder. If the contact parameter is independent on the nucleus material, but depends on the CO₂ vapor pressure, Equation 8.3.1 can be used to estimate the dependency of the contact parameter on the CO₂ vapor pressure. The result of calculating activation temperatures using Equation 8.3.1 are shown by the green solid line. Activation temperatures are the same as for a constant contact parameter of 0.72 at 120 km altitude. For lower altitudes, activation temperatures approach the calculations for $m=0.95$. Dependent on altitude, temperatures 4 to 15 K below saturation temperature are needed to activate CO₂ ice particle formation. According to these calculations typical profiles with temperatures falling below saturation temperature (red curve) would not cause CO₂ ice particle formation.

In summary, the results of this work indicate that between 2 and 7 K colder temperatures are needed to activate CO₂ ice cloud formation compared to the current scientific consensus. These results explain the absence of clouds even for highly supersaturated conditions.

8.4. Conclusions

Adsorption and nucleation experiments of CO₂ on nanometer-sized silica (SiO₂) and iron oxide (Fe₂O₃) particles were performed. The particles serve as analogues for Meteoric Smoke Particles (MSPs). Measurements were conducted at temperatures between 63 and 74 K. CO₂ nucleation sets in at saturations significantly higher than the equilibrium saturation over the nuclei surface (Kelvin effect). Consequently, the surface diffusion approach of Classical Nucleation Theory (CNT) needs to be used to describe the CO₂ ice particle formation process. This approach assumes that the adsorbed CO₂ molecules diffuse on the surface of the particle, collide and combine to clusters of different sizes. These clusters may eventually reach the critical size resulting in a nucleation event. The two parameters mainly governing nucleation rates in this theory are the desorption energy of the nucleus material $\Delta F_{\text{des,pl}}$ and the contact parameter m . The desorption energy $\Delta F_{\text{des,pl}}$ and the contact parameter m are identical for the two particle materials. The desorption energy is $(3.28 \pm 0.02) \cdot 10^{-20}$ J/molec and the contact parameter m is 0.72 ± 0.03 .

Potential condensation nuclei in the Martian mesosphere are MSPs, Martian Dust Particles (MDPs) or H₂O ice particles. The desorption energy and the contact parameter are essentially identical for all nuclei materials. However, the contact parameter very likely depends on the CO₂ vapor pressure. The experiments presented here were performed between 63 and 74 K at CO₂ vapor pressures between 1×10^{-6} and 1×10^{-4} Pa. Conditions relevant for CO₂ ice cloud formation in the Martian mesosphere are 70 to 120 K with CO₂ vapor pressures ranging from 1×10^{-6} to 1 Pa. Hence, the results obtained in this work need to be extrapolated to higher temperatures and pressures to describe onset conditions of CO₂ cloud formation in the mesosphere of Mars. An empirical expression for the pressure dependent contact parameter is given in Equation 8.3.1.

The content of this chapter aims to answer the third question formulated in the introduction:

What are onset conditions for CO₂ ice cloud formation?

Using CNT with the parameters obtained in this work, activation temperatures for CO₂ ice cloud formation in the mesosphere of Mars are 2 to 7 K colder than previously assumed. Depending on altitude, onset temperatures for the formation of CO₂ ice clouds in the mesosphere of Mars are between 4 and 15 K below the saturation temperature. These results support the observations of highly supersaturated conditions during night in the absence of clouds. The parameters obtained in this work can be used in future model studies in order to compare the results with observations.

9. Summary

Polar Mesospheric Clouds (PMCs) are water ice clouds which form at high latitudes in the summer mesopause of Earth. They have a counterpart in the mesosphere of Mars. In contrast to Earth, these Martian clouds consist of CO₂ ice particles. Ice formation of both types of clouds most likely initiates heterogeneously on nanometer-sized recondensed meteoric material, so called Meteoric Smoke Particles (MSPs). However, until now, the initial formation process of the ice particles was only poorly understood. Therefore, I investigated mesospheric ice cloud formation by studying adsorption, nucleation and growth processes of H₂O and CO₂ on MSP analogues with the MICE-TRAPS setup. In the introduction, three key questions which are essential for understanding cloud observations in the mesopause of Earth ($T < 150$ K) and the mesosphere of Mars (70 to 120 K) are formulated. All three questions are answered on the basis of the experimental results. The next two sections recapitulate the answers to these questions and discuss remaining open questions as well as the importance of the results for other fields of research.

9.1. Polar mesospheric clouds on Earth

What is the predominant ice phase involved in PMC formation?

Using MICE-TRAPS, a new technique was established to measure the saturation vapor pressure of ice phases below 160 K with an unprecedented high level of accuracy. The measurements show that Amorphous Solid Water (ASW) is the primary phase which deposits at the extreme temperatures of the summer mesopause ($T < 150$ K). Thus, the formation of ice particles is dominated by the properties of ASW rather than crystalline ice. At the temperatures of the summer mesopause the saturation vapor pressure of ASW is between 2 and 4 times higher than previously assumed. Over time, ASW crystallizes to a nano-crystalline form of stacking disordered ice I_{sd}. This nano-crystalline ice polymorph was neglected up to now. It is stable for mesopause temperatures and PMC lifetimes and exhibits a 2 to 4 times higher vapor pressure than the stable hexagonal ice I_h. Depending on the thermal history of the PMC ice particles, the vapor pressure of ASW or of nano-crystalline ice I_{sd} determines the sublimation process.

What are onset conditions for PMC formation?

Although the saturation vapor pressure of ASW is significantly higher compared to crystalline ice, particle growth is activated at unexpectedly low critical saturations. This observation is explained by the fact that MSPs are hydrophilic materials which adsorb up to several layers of H₂O, thereby significantly increasing the particle size. An activation model which describes the measured critical saturations was developed. It is based on Kelvin effect calculations and reduces uncertainties in predicting critical saturations from several orders of magnitude to less than a factor of two. In general, the studied MSP analogues are very good ice nuclei. For example, particles with radii down to about 0.6 nm activate ice growth at 120 K and for a typical H₂O concentration in the summer mesopause. These findings support the importance of MSPs as nuclei for PMCs.

9.2. Mesospheric CO₂ clouds on Mars

What are onset conditions for CO₂ ice cloud formation?

In contrast to H₂O ice nucleation on Earth, CO₂ nucleation is activated on the MSP analogues (Fe₂O₃ and SiO₂) at saturations significantly higher than the Kelvin effect. In order to describe the onset conditions for CO₂ ice growth, the surface diffusion approach of Classical Nucleation Theory (CNT) was used. The two parameters mainly governing nucleation rates in this theory are the desorption energy of the nucleus material $\Delta F_{\text{des,pl}}$ and the contact parameter m . They are independent of the material of the MSP analogues and are $F_{\text{des,pl}} = (3.28 \pm 0.02) \cdot 10^{-20} \text{ J/molec}$ and $m = 0.72 \pm 0.03$ between 63 and 74 K. It is very likely that $\Delta F_{\text{des,pl}}$ and m are similar for all potential nuclei materials in the Martian mesosphere. However, the contact parameter m exhibits a dependency on the CO₂ vapor pressure (Equation 8.3.1).

Using CNT with the parameters obtained in this work, activation temperatures for CO₂ ice cloud formation in the mesosphere of Mars are 2 to 7 K colder than previously assumed. Depending on altitude, onset temperatures are between 4 and 15 K below the saturation temperature. These results may explain the absence of clouds during highly supersaturated conditions.

9.3. Outlook

The results of this work significantly improve the understanding of H₂O and CO₂ ice particle formation under the extreme conditions of the summer mesopause of Earth (T < 150 K) and the mesosphere of Mars (70 to 120 K). It is now up to the modeling community to include the H₂O activation model or the parameters for CO₂ nucleation to compare model results on cloud formation with observations.

Asmus et al. [2014] proposed that MSPs might heat up with respect to the temperature of the environment in the summer mesopause due to absorption of solar radiation. Using the results of their calculations, the maximum possible temperature increase for the majority of MSPs in the summer mesopause is estimated to 4 K. Accordingly, the activation model predicts that critical saturations with respect to the ambient temperature increase by a factor of at most 2.5. However, the influence of particle heating on critical saturations should still be confirmed experimentally. Recently, the TRAPS setup was extended with an optical system which allows to expose the particles levitated in MICE to an expanded laser beam simulating solar irradiation. First experiments show that the particle heating is reduced since the adsorption of H₂O molecules increases the effective surface area of the particles making the collisional cooling much more effective. These preliminary results indicate that the maximum temperature increase of MSPs in the mesopause is less than 4 K and has no severe impact on critical saturations. More measurements using the new setup will provide a more quantitative assessment of the light absorption effect on PMC formation.

The particles investigated in this work were singly charged. The experimental results did not show any influence of the particle charge on critical saturations down to particle radii of 1 nm. An absence of charge effects in the investigated particle size range is an intriguing result, which was unexpected. In order to draw conclusions about potential influences of the particle charge on critical saturations for smaller particles, further experimental investigations with particles smaller than 1 nm in radius are needed.

About 10% of the MSP population in the summer mesopause are expected to be negatively charged [Plane et al., 2014, 2015]. However, the TOF spectrometer is currently able to detect positively charged particles, only. Preparations to modify the TOF spectrometer so that negatively charged particles can be detected have already been undertaken. In the near future, experiments with negatively charged particles will be conducted to investigate if the polarity has any effect on critical saturations.

The results of this work are also important for other fields of research. The vapor pressures of metastable ice phases are important for modeling H₂O adsorption and desorption processes in interstellar environments as well as water residence times on interstellar grains [e.g. Fraser et al., 2001]. Additionally, the results are important for the formation of water ice clouds, which frequently form on Mars below 50 km altitude [e.g. Whiteway et al., 2009; McCleese et al., 2010; Guzewich et al., 2013]. At these altitudes, temperatures commonly fall below 160 K [Maltagliati et al., 2011, 2013; Trokhimovskiy et al., 2015]. In general, the results are significant for cloud formation processes in the atmospheres of other planets.

A. Characterization of the MSP analogues

The nucleation ability of particles depends on the particle material. Thus, experiments with particles composed of any kind of potential Meteoric Smoke Particle (MSP) materials are of desire. Therefore, it is important to know the exact composition of the MSP analogues produced with the microwave plasma source. Experiments were conducted to characterize the particles produced with the microwave plasma source. The results are published in Nachbar et al. [2018b]. Here, I briefly summarize the main results and refer the interested reader to the original work.

Iron oxide, silicon oxide and mixed iron-silicate particles were produced with the microwave plasma resonator by varying the temperature of the precursor materials. The produced particles were transferred to the Trapped Reactive Particle Spectrometer (TRAPS) where they were deposited on Transmission Electron Microscope (TEM) sample grids placed in front of the skimmer. The bulk composition of the particles deposited on the sample grids was analyzed with energy dispersive X-ray spectroscopy (EDS) in a scanning electron microscope. The EDS analysis shows that the organic parts of the precursors are sufficiently oxidized to CO₂ and H₂O and no carbon residue is included in the particle material. The particles are solely composed of silicon, iron, and oxygen. Figure A.1 shows the atomic [Fe]/[Si] ratio determined with the EDS measurements as a function of the vapor pressure ratio of the two precursor materials. Here, [Fe] is the concentration of iron atoms and [Si] the concentration of silicon atoms. Applied TEOS temperatures were 5 °C, 15 °C, 23 °C and 24 °C (blue, green, black and red squares, respectively). The temperature of ferrocene was varied between 45 °C and 90 °C for each of the four TEOS temperatures. The experiments were performed at 5 different days distributed over one month. At the beginning of each experimental day, the precursor reservoirs were refilled with fresh ferrocene and TEOS. The [Fe]/[Si] ratio is highly reproducible and shows a linear dependency on the vapor pressure ratio of the two precursor materials. A linear fit to the data yields:

$$\frac{[Fe]}{[Si]} = (0.007 \pm 0.014) + (0.332 \pm 0.012) \cdot \frac{p_{TEOS}}{p_{ferrocene}} \quad (\text{A.0.1})$$

The iron so silicon ratio of the particle material can be controlled solely by adjusting the temperature of the precursor materials according to Equation A.0.1.

Figure A.2 shows the element to oxygen ratio [M]:[O] of the particle material analyzed with EDS as a function of the relative iron content displayed as atomic [Fe]:([Fe]+[Si]) ratio. The red triangles show the atomic [Fe]:[O] ratio, the black dots the [Si]:[O] ratio and the blue squares the combined ([Fe]+[Si]):[O] ratio. In addition, the ([Fe]+[Si]):[O] ratios of the minerals magnetite (Fe₃O₄), hematite (Fe₂O₃), silica (SiO₂), fayalite

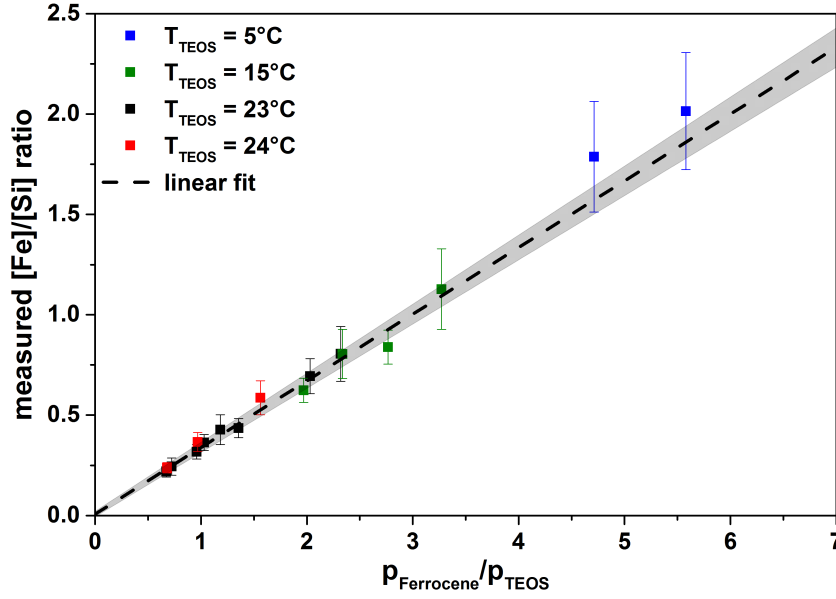


Figure A.1.: [Fe]/[Si] ratio of the MSP analogues determined with EDS measurements as a function of the vapor pressure ratio of the silicon (TEOS) and iron (ferrocene) precursors.

(Fe_2SiO_4) and ferrosilite (FeSiO_3) are shown.

Iron oxide particles ($[\text{Fe}]:([\text{Fe}]+[\text{Si}])=1$) are composed of Fe_2O_3 ($\rho = 5.2 \text{ gcm}^{-3}$). This is in agreement with results of similar experimental arrangements [Nadeem et al., 2012; Chou and Phillips, 1992; David et al., 2012]. Two Fe_2O_3 polymorphs exist, stable $\alpha\text{-Fe}_2\text{O}_3$ (hematite) and metastable and ferrimagnetic $\gamma\text{-Fe}_2\text{O}_3$ (maghemite). David et al. [2012] produced nano-particles in a similar experimental arrangement. Using XRD, Raman and Mössbauer spectroscopy measurements, they found out that the polymorph in their experiments is maghemite. On the basis of these results and since the formation of maghemite is thermodynamically favored with respect to hematite for particles smaller than 16 nm in diameter [Navrotsky et al., 2008], it is likely that the microwave particle source produces maghemite particles rather than hematite particles. Silicon oxide particles ($[\text{Fe}]:([\text{Fe}]+[\text{Si}])=0$) are composed of SiO_2 (silica, $\rho = 2.3 \text{ gcm}^{-3}$). This result is consistent with a previous investigation using a similar experimental arrangement [Knipping et al., 2004].

Mixed iron silicates, however, are not composed of a mixture of SiO_2 and Fe_2O_3 . For iron to silicon ratios of $0.2 < [\text{Fe}]:([\text{Fe}]+[\text{Si}]) < 0.8$, they are composed of $\text{Fe}_x\text{Si}_{1-x}\text{O}_3$ ($0 < x < 1$). This stoichiometric composition is shown by the red, black and blue lines with the colors indicating the different [M]:[O] ratios. Rearrangement to more stable silicates like FeSiO_3 or Fe_2SiO_4 does not occur. The fact that $\text{Fe}_x\text{Si}_{1-x}\text{O}_3$ particles are produced indicates that particle formation occurs via initial aggregation of FeO_3 and/or SiO_3 molecules from the gas phase.

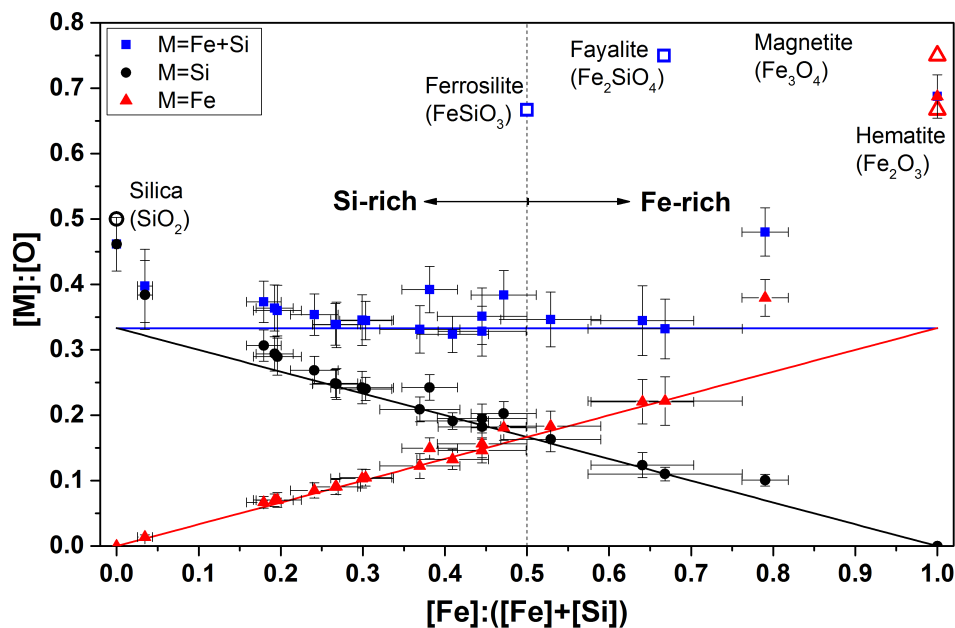


Figure A.2.: Element to oxygen ratio $[M]:[O]$ of the MSP analogues as a function of the iron content displayed as atomic $[Fe]:([Fe]+[Si])$ ratio. The red triangles, black dots and blue squares shows the results for $M=Fe$, $M=Si$ and $M=Fe+Si$, respectively. The colored lines represent a composition according to $Fe_xSi_{1-x}O_3$. Element to oxygen ratios of naturally occurring minerals are shown for comparison. Reproduced from Nachbar et al. [2018b], with permission of De Gruyter.

Information about whether more than one particle type is produced in the microwave plasma source or not can not be obtained with EDS measurements. The EDS analysis averages over many particles deposited on the TEM grids and therefore reflects the mean stoichiometric composition of the particles. H_2O adsorption measurements as a function of the iron to silicon content were used to gain information about the mixing state of the particles. The results of such measurements are presented in Chapter 7. The results show, that only one kind of particle is produced, that the particles are internally mixed and differential coating to a core shell structure does not occur.

B. List of parameters

Table B.1 summarizes all material properties or parameters of H₂O and CO₂ which are used in this work.

Table B.1.: Summary of parameters.

Parameter	Symbol	Unit	Value	Reference
H₂O				
Surface tension of ASW	σ_a	N m ⁻¹	$0.001 \cdot (75.662 - 0.13935 \cdot T[^\circ\text{C}])$	linear fit to [Vins et al., 2015]
Surface tension of crystalline ice	σ_c	N m ⁻¹	$0.001 \cdot (141 - 0.15 \cdot T[\text{K}])$	[Hale and Plummer, 1974]
Density of ice	ρ	g cm ⁻³	$0.9167 - 1.75 \cdot 10^{-4} \cdot T[^\circ\text{C}] - 5 \cdot 10^{-7} \cdot T[^\circ\text{C}]^2$	[Pruppacher and Klett, 2010]
Vibrational frequency	ν	s ⁻¹	10^{13}	[Pruppacher and Klett, 2010]
Mean jumping distance of a molecule	d	nm	0.32	[Pruppacher and Klett, 2010]
Hard sphere collision radius	r	nm	0.228	[Zamith et al., 2013]
relative permittivity	ϵ_r	-	$3.2 + \frac{24620}{T-6.2}$	[Johari and Whalley, 1981]
dipole moment	μ	C m	$1.84 \cdot 3.33564 \cdot 10^{-30}$	[Fernandez et al., 1997]
polarizability	p	C ² m ² J ⁻¹	$1.636 \cdot 10^{-40}$	[Fernandez et al., 1997]
CO₂				
Surface tension	σ	N m ⁻¹	0.08	[Wood, 1999]
Density of ice	ρ	g cm ⁻³	$1.72391 - 2.53 \cdot 10^{-4} \cdot T[\text{K}] - 2.87 \cdot 10^{-6} \cdot T[\text{K}]^2$	[Mangan et al., 2017]
Vibrational frequency	ν	s ⁻¹	$2.9 \cdot 10^{12}$	[Sandford and Allamandola, 1990]
Mean jumping distance of a molecule	d	nm	0.4	[Wood, 1999]
Hard sphere collision radius	r	nm	0.197	[Hirschfelder et al., 1966]
relative permittivity	ϵ_r	-	5	[Garry, 2001]
polarizability	p	C ² m ² J ⁻¹	$2.93 \cdot 10^{-40}$	[Lewis et al., 2000]

Bibliography

- Adolfsson, L. G., Gustafson, B. A. S., and Murray, C. D. The Martian atmosphere as a meteoroid detector. *Icarus*, 119(1):144–152, 1996. doi:10.1006/icar.1996.0007.
- Akmaev, R. A. and Fomichev, V. I. Cooling of the mesosphere and lower thermosphere due to doubling of CO₂. *Annales Geophysicae - Atmospheres Hydrospheres and Space Science*, 16(11):1501–1512, 1998. doi:10.1007/s00585-998-1501-z.
- Andersson, P. U., Nagard, M. B., Witt, G., and Pettersson, J. B. C. Carbon dioxide interactions with crystalline and amorphous ice surfaces. *Journal of Physical Chemistry A*, 108(21):4627–4631, 2004. doi:10.1021/jp049346c.
- Antonsen, T., Havnes, O., and Mann, I. Estimates of the Size Distribution of Meteoric Smoke Particles From Rocket-Borne Impact Probes. *Journal of Geophysical Research - Atmospheres*, 122(22):12353–12365, 2017. doi:10.1002/2017JD027220.
- Arnold, E. D., G. P. and Finch, Rabideau, S. W., and Wenzel, R. G. Neutron-Diffraction study of ice polymorphs III. Ice Ic. *Journal of Chemical Physics*, 49(10), 1968. doi:10.1063/1.1669883.
- Asmus, H., Wilms, H., Strelnikov, B., and Rapp, M. On the heterogeneous nucleation of mesospheric ice on meteoric smoke particles: Microphysical modeling. *Journal of Atmospheric and Solar-Terrestrial Physics*, 118:180–189, 2014. doi:10.1016/j.jastp.2014.03.009.
- Asmus, H., Staszak, T., Strelnikov, B., Luebken, F.-J., Friedrich, M., and Rapp, M. Estimate of size distribution of charged MSPs measured in situ in winter during the WADIS-2 sounding rocket campaign. *Annales Geophysicae*, 35(4):979–998, 2017. doi:10.5194/angeo-35-979-2017.
- Azreg-Ainou, M. Low-temperature data for carbon dioxide. *Monatshefte fuer Chemie*, 136(12):2017–2027, 2005. doi:10.1007/s00706-005-0370-3.
- Backus, E. H. G. and Bonn, M. Theory of bulk, surface and interface phase transition kinetics in thin films. *Journal of Chemical Physics*, 121(2):1038–1049, 2004. doi:10.1063/1.1760737.
- Bardeen, C. G., Toon, O. B., Jensen, E. J., Marsh, D. R., and Harvey, V. L. Numerical simulations of the three-dimensional distribution of meteoric dust in the mesosphere and upper stratosphere. *Journal of Geophysical Research - Atmospheres*, 113(D17), 2008. doi:10.1029/2007JD009515.

- Bardeen, C. G., Toon, O. B., Jensen, E. J., Hervig, M. E., Randall, C. E., Benze, S., Marsh, D. R., and Merkel, A. Numerical simulations of the three-dimensional distribution of polar mesospheric clouds and comparisons with Cloud Imaging and Particle Size (CIPS) experiment and the Solar Occultation For Ice Experiment (SOFIE) observations. *Journal of Geophysical Research - Atmospheres*, 115, 2010. doi:10.1029/2009JD012451.
- Batista, E. R., Ayotte, P., Bilic, A., Kay, B. D., and Jonsson, H. What determines the sticking probability of water molecules on ice? *Physical Review Letters*, 95(22), 2005. doi:10.1103/PhysRevLett.95.223201.
- Berger, U. Modeling of middle atmosphere dynamics with LIMA. *Journal of Atmospheric and Solar-Terrestrial Physics*, 70(8-9):1170–1200, 2008. doi:10.1016/j.jastp.2008.02.004.
- Berger, U. and Luebken, F. J. Trends in mesospheric ice layers in the Northern Hemisphere during 1961-2013. *Journal of Geophysical Research - Atmospheres*, 120(21): 11277–11298, 2015. doi:10.1002/2015JD023355.
- Berger, U. and von Zahn, U. The two-level structure of the mesopause: A model study. *Journal of Geophysical Research - Atmospheres*, 104(D18):22083–22093, 1999. doi:10.1029/1999JD900389.
- Bielska, K., Havey, D. K., Scace, G. E., Lisak, D., Harvey, A. H., and Hodges, J. T. High-accuracy measurements of the vapor pressure of ice referenced to the triple point. *Geophysical Research Letters*, 40(23):6303–6307, 2013. doi:10.1002/2013GL058474.
- Brown, D., George, S., Huang, C., Wong, E., Rider, K., Smith, R., and Kay, B. H₂O condensation coefficient and refractive index for vapor-deposited ice from molecular beam and optical interference measurements. *Journal of Physical Chemistry*, 100(12):4988–4995, 1996. doi:10.1021/jp952547j.
- Bryson, C. E., Cazarra, V., and Levenson, L. L. Sublimation rates and vapor-pressures of H₂O, CO₂, N₂O, and Xe. *Journal of Chemical and Engineering Data*, 19(2):107–110, 1974. doi:10.1021/je60061a021.
- Carrillo-Sanchez, J. D., Plane, J. M. C., Feng, W., Nesvorny, D., and Janches, D. On the size and velocity distribution of cosmic dust particles entering the atmosphere. *Geophysical Research Letters*, 42(15):6518–6525, 2015. doi:10.1002/2015GL065149.
- Carrillo-Sanchez, J. D., Nesvorny, D., Pokorny, P., Janches, D., and Plane, J. M. C. Sources of cosmic dust in the Earth's atmosphere. *Geophysical Research Letters*, 43(23):11979–11986, 2016. doi:10.1002/2016GL071697.
- Castleman, A. W. and Tang, I. Role of Small Clusters in Nucleation about Ions. *Journal of Chemical Physics*, 57(9), 1972. doi:10.1063/1.1678819.

- Chinchen, G. C., Spencer, M. S., Waugh, K. C., and Whan, D. A. Promotion of methanol synthesis and the water-gas shift reactions by adsorbed oxygen on supported copper-catalyst. *Journal of the Chemical Society - Faraday Transactions I*, 83 (7):2193–2212, 1987. doi:10.1039/f19878302193.
- Chonde, M., Brindza, M., and Sadtchenko, V. Glass transition in pure and doped amorphous solid water: An ultrafast microcalorimetry study. *Journal of Chemical Physics*, 125(9), 2006. doi:10.1063/1.2338524.
- Chou, C. H. and Phillips, J. Plasma production of metallic nanoparticles. *Journal of Materials Research*, 7(8):2107–2113, 1992. doi:10.1557/JMR.1992.2107.
- Clancy, R. T., Wolff, M. J., Whitney, B. A., Cantor, B. A., and Smith, M. D. Mars equatorial mesospheric clouds: Global occurrence and physical properties from Mars Global Surveyor Thermal Emission Spectrometer and Mars Orbiter Camera limb observations. *Journal of Geophysical Research - Planets*, 112(E4), 2007. doi:10.1029/2006JE002805.
- Clancy, R. and Sandor, B. CO₂ ice clouds in the upper atmosphere of Mars. *Geophysical Research Letters*, 25(4):489–492, 1998. doi:10.1029/98GL00114.
- Colaprete, A., Haberle, R., and Toon, O. Formation of convective carbon dioxide clouds near the south pole of Mars. *Journal of Geophysical Research - Planets*, 108 (E7), 2003. doi:10.1029/2003JE002053.
- Creasey, J., Forbes, J., and Hinson, D. Global and seasonal distribution of gravity wave activity in Mars' lower atmosphere derived from MGS radio occultation data. *Geophysical Research Letters*, 33(1), 2006. doi:10.1029/2005GL024037.
- Crismani, M. M. J., Schneider, N. M., Plane, J. M. C., Evans, J. S., Jain, S. K., Chaffin, M. S., Carrillo-Sanchez, J. D., Deighan, J. I., Yelle, R. V., Stewart, A. I. F., McClintock, W., Clarke, J., Holsclaw, G. M., Stiepen, A., Montmessin, F., and Jakosky, B. M. Detection of a persistent meteoric metal layer in the Martian atmosphere. *Nature Geoscience*, 10(6), 2017. doi:10.1038/NGEO2958.
- David, B., Pizurova, N., Schneeweiss, O., Santava, E., Kudrle, V., and Jasek, O. gamma-Fe₂O₃ Nanopowders Synthesized in Microwave Plasma and Extraordinarily Strong Temperature Influence on Their Mossbauer Spectra. *Journal of Nanoscience and Nanotechnology*, 12(12):9277–9285, 2012. doi:10.1166/jnn.2012.6767.
- DeLand, M. T., Shettle, E. P., Thomas, G. E., and Olivero, J. J. Latitude-dependent long-term variations in polar mesospheric clouds from SBUV version 3 PMC data. *Journal of Geophysical Research: Atmospheres*, 112(D10), 2007. doi:10.1029/2006JD007857. D10315.

- Demissie, T. D., Espy, P. J., Kleinknecht, N. H., Hatlen, M., Kaifler, N., and Baumgarten, G. Characteristics and sources of gravity waves observed in noctilucent cloud over Norway. *Atmospheric Chemistry and Physics*, 14(22):12133–12142, 2014. doi:10.5194/acp-14-12133-2014.
- Dohnalek, Z., Kimmel, G., Ayotte, P., Smith, R., and Kay, B. The deposition angle-dependent density of amorphous solid water films. *Journal of Chemical Physics*, 118(1):364–372, 2003. doi:10.1063/1.1525805.
- Dowell, L. G. and Rinfret, A. P. Low temperature forms of ice as studied by X-ray diffraction. *Nature*, 188(4757):1144–1148, 1960. doi:10.1038/1881144a0.
- Duft, D., Nachbar, M., Eritt, M., and Leisner, T. A Linear Trap for Studying the Interaction of Nanoparticles with Supersaturated Vapors. *Aerosol Science and Technology*, 49(9):682–690, 2015. doi:10.1080/02786826.2015.1063583.
- Eremenko, M., Petelina, S., Zasetsky, A., Karlsson, B., Rinsland, C., Llewellyn, E., and Sloan, J. Shape and composition of PMC particles derived from satellite remote sensing measurements. *Geophysical Research Letters*, 32(16), 2005. doi:10.1029/2005GL023013.
- Feistel, R. and Wagner, W. A new equation of state for H₂O ice Ih. *Journal of Physical and Chemical Reference Data*, 35(2):1021–1047, 2006. doi:10.1063/1.2183324.
- Feistel, R. and Wagner, W. Sublimation pressure and sublimation enthalpy of H₂O ice Ih between 0 and 273.16 K. *Geochimica et Cosmochimica Acta*, 71(1):36–45, 2007. doi:10.1016/j.gca.2006.08.034.
- Fernandez, D., Goodwin, A., Lemmon, E., Sengers, J., and Williams, R. A formulation for the static permittivity of water and steam at temperatures from 238 K to 873 K at pressures up to 1200 MPa, including derivatives and Debye-Huckel coefficients. *Journal of Physical and Chemical Reference Data*, 26(4):1125–1166, 1997. doi:10.1063/1.555997.
- Fernicola, V., Rosso, L., and Giovannini, M. Investigation of the Ice-Water Vapor Equilibrium Along the Sublimation Line. *International Journal of Thermophysics*, 33:1363–1373, 2012. doi:10.1007/s10765-011-1128-2.
- Fletcher, N. H. Size Effect in Heterogeneous Nucleation. *Journal of Chemical Physics*, 29(3):572–576, 1958. doi:10.1063/1.1744540.
- Floriano, M. A., Handa, Y. P., Klug, D. D., and Whalley, E. Nature of the transformations of ice-I and low-density amorphous ice to high-density amorphous ice. *Journal of Chemical Physics*, 91(11):7187–7192, 1989. doi:10.1063/1.457285.
- Forget, F., Montmessin, F., Bertaux, J.-L., Gonzalez-Galindo, F., Lebonnois, S., Quemerais, E., Reberac, A., Dimarellis, E., and Lopez-Valverde, M. A. Density and

- temperatures of the upper Martian atmosphere measured by stellar occultations with Mars Express SPICAM. *Journal of Geophysical Research - Planets*, 114, 2009. doi:10.1029/2008JE003086.
- Fortin, T., Drdla, K., Iraci, L., and Tolbert, M. Ice condensation on sulfuric acid tetrahydrate: Implications for polar stratospheric ice clouds. *Atmospheric Chemistry and Physics*, 3:987–997, 2003. doi:10.5194/acp-3-987-2003.
- Fraser, H., Collings, M., McCoustra, M., and Williams, D. Thermal desorption of water ice in the interstellar medium. *Monthly Notices of the Royal Astronomical Society*, 327(4):1165–1172, 2001. doi:10.1046/j.1365-8711.2001.04835.x.
- Fung, K. H. and Tang, I. N. Thermal-accommodation measurement of helium on a suspended water droplet. *Physical Review A*, 37(7):2557–2561, 1988. doi:10.1103/PhysRevA.37.2557.
- Ganta, D., Dale, E. B., Rezac, J. P., and Rosenberger, A. T. Optical method for measuring thermal accommodation coefficients using a whispering-gallery microresonator. *Journal of Chemical Physics*, 135(8), 2011. doi:10.1063/1.3631342.
- Garry, J. R. C. The Measured Permittivity of CO₂ Ice Grown under Martian Polar Conditions. In *Conference on the Geophysical Detection of Subsurface Water on Mars*, 2001.
- Ghormley, J. Enthalpy changes and heat-capacity changes in transformations from high-surface-area amorphous ice to stable hexagonal ice. *Journal of Chemical Physics*, 48(1), 1968. doi:10.1063/1.1667954.
- Giauque, W. F. and Egan, C. J. Carbon Dioxide. The heat capacity and vapor pressure of the solid. The heat of sublimation. Thermodynamic and spectroscopic values of the entropy. *The Journal of Chemical Physics*, 5(45), 1937. doi:10.1063/1.1749929.
- Gibson, K. D., Killelea, D. R., Yuan, H., Becker, J. S., and Sibener, S. J. Determination of the sticking coefficient and scattering dynamics of water on ice using molecular beam techniques. *Journal of Chemical Physics*, 134(3), 2011. doi:10.1063/1.3528116.
- Giesen, B., Wiggers, H., Kowalik, A., and Roth, P. Formation of Si-nanoparticles in a microwave reactor: Comparison between experiments and modelling. *Journal of Nanoparticle Research*, 7(1):29–41, 2005. doi:10.1007/s11051-005-0316-z.
- Glandorf, D., Colaprete, A., Tolbert, M., and Toon, O. CO₂ snow on Mars and early Earth: Experimental constraints. *Icarus*, 160(1):66–72, 2002. doi:10.1006/icar.2002.6953.
- Gonzalez-Galindo, F., Maattanen, A., Forget, F., and Spiga, A. The martian mesosphere as revealed by CO₂ cloud observations and General Circulation Modeling. *Icarus*, 216(1):10–22, 2011. doi:10.1016/j.icarus.2011.08.006.

- Gumbel, J. and Megner, L. Charged meteoric smoke as ice nuclei in the mesosphere: Part 1-A review of basic concepts. *Journal of Atmospheric and Solar-Terrestrial Physics*, 71(12):1225–1235, 2009. doi:10.1016/j.jastp.2009.04.012.
- Guzewich, S. D., Talaat, E. R., Toigo, A. D., Waugh, D. W., and McConnochie, T. H. High-altitude dust layers on Mars: Observations with the Thermal Emission Spectrometer. *Journal of Geophysical Research - Planets*, 118(6):1177–1194, 2013. doi:10.1002/jgre.20076.
- Hale, B. N. and Plummer, P. L. M. Molecular model for ice clusters in a supersaturated vapor. *Journal of Chemical Physics*, 61(10):4012–4019, 1974. doi:10.1063/1.1681694.
- Hallbrucker, A. and Mayer, E. Calorimetric study of the vitrified liquid water to the cubic ice phase-transition. *Journal of Physical Chemistry*, 91(3):503–505, 1987. doi:10.1021/j100287a002.
- Hallbrucker, A., Mayer, E., and Johari, G. P. Glass-Liquid transition and the enthalpy of devitrification of annealed vapor-deposited amorphous solid water - a comparison with hyperquenched glassy water. *Journal of Physical Chemistry*, 93(12):4986–4990, 1989. doi:10.1021/j100349a061.
- Handa, Y., Mishima, O., and Whalley, E. High-density amorphous ice 3. Thermal-properties. *journal of Chemical Physics*, 84(5):2766–2770, 1986. doi:10.1063/1.450301.
- Hansen, T. C., Koza, M. M., Lindner, P., and Kuhs, W. F. Formation and annealing of cubic ice: II. Kinetic study. *Journal of Physics - Condensed Matter*, 20(28), 2008. doi:10.1088/0953-8984/20/28/285105.
- Havnes, O., Gumbel, J., Antonsen, T., Hedin, J., and La Hoz, C. On the size distribution of collision fragments of NLC dust particles and their relevance to meteoric smoke particles. *Journal of Atmospheric and Solar-Terrestrial Physics*, 118:190–198, 2014. doi:10.1016/j.jastp.2014.03.008.
- Heald, J. H. and Brown, R. F. Measurements of condensation and evaporation of carbon dioxide, nitrogen, and argon at cryogenic temperatures using a molecular beam. Technical report, Aerospace environmental facility, Arnold engineering development center, Air force systems command, Arnold air force station, Tennessee, 1968.
- Heavens, N. G., McCleese, D. J., Richardson, M. I., Kass, D. M., Kleinboehl, A., and Schofield, J. T. Structure and dynamics of the Martian lower and middle atmosphere as observed by the Mars Climate Sounder: 2. Implications of the thermal structure and aerosol distributions for the mean meridional circulation. *Journal of Geophysical Research - Planets*, 116, 2011a. doi:10.1029/2010JE003713.

- Heavens, N. G., Richardson, M. I., Kleinboehl, A., Kass, D. M., McCleese, D. J., Abdou, W., Benson, J. L., Schofield, J. T., Shirley, J. H., and Wolkenberg, P. M. The vertical distribution of dust in the Martian atmosphere during northern spring and summer: Observations by the Mars Climate Sounder and analysis of zonal average vertical dust profiles. *Journal of Geophysical Research - Planets*, 116, 2011b. doi:10.1029/2010JE003691.
- Heavens, N. G., Cantor, B. A., Hayne, P. O., Kass, D. M., Kleinboehl, A., McCleese, D. J., Piqueux, S., Schofield, J. T., and Shirley, J. H. Extreme detached dust layers near Martian volcanoes: Evidence for dust transport by mesoscale circulations forced by high topography. *Geophysical Fluid Dynamics*, 42(10):3730–3738, 2015. doi:10.1002/2015GL064004.
- Heavens, N. G., Johnson, M. S., Abdou, W. A., Kass, D. M., Kleinboehl, A., McCleese, D. J., Shirley, J. H., and Wilson, R. J. Seasonal and diurnal variability of detached dust layers in the tropical Martian atmosphere. *Journal of Geophysical Research - Planets*, 119(8):1748–1774, 2014. doi:10.1002/2014JE004619.
- Hervig, M. E. and Gordley, L. L. Temperature, shape, and phase of mesospheric ice from Solar Occultation for Ice Experiment observations. *Journal of Geophysical Research - Atmospheres*, 115(D15), 2010. doi:10.1029/2010JD013918.
- Hervig, M. E., Gordley, L. L., Deaver, L. E., Siskind, D. E., Stevens, M. H., Russell, J. M., III, Bailey, S. M., Megner, L., and Bardeen, C. G. First Satellite Observations of Meteoric Smoke in the Middle Atmosphere. *Geophysical Research Letter*, 36, 2009. doi:10.1029/2009GL039737.
- Hervig, M. E., Deaver, L. E., Bardeen, C. G., Russell, J. M., III, Bailey, S. M., and Gordley, L. L. The content and composition of meteoric smoke in mesospheric ice particles from SOFIE observations. *Journal of Atmospheric and Solar-Terrestrial Physics*, 84-85:1–6, 2012. doi:10.1016/j.jastp.2012.04.005.
- Hervig, M. E., Berger, U., and Siskind, D. E. Decadal variability in PMCs and implications for changing temperature and water vapor in the upper mesosphere. *Journal of Geophysical Research - Atmospheres*, 121(5):2383–2392, 2016. doi:10.1002/2015JD024439.
- Hill, C. R., Mitterdorfer, C., Youngs, T. G. A., Bowron, D. T., Fraser, H. J., and Loerting, T. Neutron Scattering Analysis of Water’s Glass Transition and Micropore Collapse in Amorphous Solid Water. *Physical Review Letters*, 116(21), 2016. doi:10.1103/PhysRevLett.116.215501.
- Hirschfelder, J. C., Curtiss, F., and Bird, R. B. *Molecular Theory of Gases and Liquids*. John Wiley and Sons, 1966.
- Hobbs, P. V. *Ice Physics*. Oxford University Press, 1974.

- Holton, J. R. The Role of Gravity Wave Induced Drag and Diffusion in the Momentum Budget of the Mesosphere. *Journal of the Atmospheric Sciences*, pages 791–799, 1982. doi:10.1175/1520-0469(1982)039<0791:TROGWI>2.0.CO;2.
- Hondo, T., Itoh, T., Amakai, S., Goto, K., and Higashi, A. Formation and annihilation of stacking-faults in pure ice. *Journal of Physical Chemistry*, 87(21):4040–4044, 1983. doi:10.1021/j100244a008.
- Hudait, A., Qiu, S., Lupi, L., and Molinero, V. Free energy contributions and structural characterization of stacking disordered ices. *Physical Chemistry Chemical Physics*, 18(14):9544–9553, 2016. doi:10.1039/c6cp00915h.
- Hunten, D. M., Turco, R. P., and Toon, O. B. Smoke and dust particle of meteoric origin in the mesosphere and stratosphere. *Journal of Atmospheric Science*, 37(6): 1342–1357, 1980. doi:10.1175/1520-0469(1980)037<1342:SADPOM>2.0.CO;2.
- Iraci, L. T., Phebus, B. D., Stone, B. M., and Colaprete, A. Water ice cloud formation on Mars is more difficult than presumed: Laboratory studies of ice nucleation on surrogate materials. *Icarus*, 210(2):985–991, 2010. doi:10.1016/j.icarus.2010.07.020.
- James, P. B., Kieffer, H. H., and A., P. D. *The seasonal cycle of carbon dioxide on Mars in Mars*. Univ. Ariz. Press, 1992.
- Jansco, G., Pupezin, J., and Van Hook, W. A. The vapor pressure of Ice between $1E-2$ and $1E+20$. *The Journal of Physical Chemistry*, 74 (15):2984–2989, 1970.
- Janzen, C., Kleinwechter, H., Knipping, J., Wiggers, H., and Roth, P. Size analysis in low-pressure nanoparticle reactors: comparison of particle mass spectrometry with in situ probing transmission electron microscopy. *Journal of Aerosol Science*, 33(6): 833–841, 2002. doi:10.1016/S0021-8502(02)00048-4.
- Jenniskens, P. and Blake, D. F. Crystallization of amorphous water ice in the solar system. *Astrophysical Journal*, 473, 1996. doi:10.1086/178220.
- Johari, G. P. and Whalley, E. The Dielectric-Properties of Ice Ih in the Range 272-133 K. *Journal of Chemical Physics*, 75(3):1333–1340, 1981. doi:10.1063/1.442139.
- Johari, G., Fleissner, G., Hallbrucker, A., and Mayer, E. Thermodynamic continuity between glassy and normal water. *Journal of Physical Chemistry*, 98(17):4719–4725, 1994. doi:10.1021/j100068a038.
- Kaifler, N., Baumgarten, G., Fiedler, J., and Luebken, F.-J. Quantification of waves in lidar observations of noctilucent clouds at scales from seconds to minutes. *Atmospheric Chemistry and Physics*, 13(23):11757–11768, 2013. doi:10.5194/acp-13-11757-2013.

- Keesee, R. G. Nucleation and particle formation in the upper atmosphere. *Journal of Geophysical Research - Atmospheres*, 94(D12):14683–14692, 1989. doi:10.1029/JD094iD12p14683.
- Kendelewicz, T., Kaya, S., Newberg, J. T., Bluhm, H., Mulakaluri, N., Moritz, W., Scheffler, M., Nilsson, A., Pentcheva, R., and Brown, G. E., Jr. X-ray Photoemission and Density Functional Theory Study of the Interaction of Water Vapor with the Fe₃O₄(001) Surface at Near-Ambient Conditions. *Journal of Physical Chemistry C*, 117(6):2719–2733, 2013. doi:10.1021/jp3078024.
- Keyser, L. F. and Leu, M. T. Morphology of Nitric-Acid and Water Ice Films. *Microscopy Research and Technique*, 25(5-6):434–438, 1993. doi:10.1002/jemt.1070250514.
- Kiliani, J., Baumgarten, G., Luebken, F. J., and Berger, U. Impact of particle shape on the morphology of noctilucent clouds. *Atmospheric Chemistry and Physics*, 15(22):12897–12907, 2015. doi:10.5194/acp-15-12897-2015.
- Kimmel, G., Dohnalek, Z., Stevenson, K., Smith, R., and Kay, B. Control of amorphous solid water morphology using molecular beams. II. Ballistic deposition simulations. *Journal of Chemical Physics*, 114(12):5295–5303, 2001a. doi:10.1063/1.1350581.
- Kimmel, G., Stevenson, K., Dohnalek, Z., Smith, R., and Kay, B. Control of amorphous solid water morphology using molecular beams. I. Experimental results. *Journal of Chemical Physics*, 114(12):5284–5294, 2001b. doi:10.1063/1.1350580.
- Kirkwood, S., Dalin, P., and Rehou, A. Noctilucent clouds observed from the UK and Denmark - trends and variations over 43 years. *Annales Geophysicae*, 26(5):1243–1254, 2008. doi:10.5194/angeo-26-1243-2008.
- Knipping, J., Wiggers, H., Rellinghaus, B., Roth, P., Konjhodzic, D., and Meier, C. Synthesis of high purity silicon nanoparticles in a low pressure microwave reactor. *Journal of Nanoscience and Nanotechnology*, 4(8):1039–1044, 2004. doi:10.1166/jnn.2004.149.
- Kondo, T., Kato, H. S., Bonn, M., and Kawai, M. Morphological change during crystallization of thin amorphous solid water films on Ru(0001). *Journal of Chemical Physics*, 126(18), 2007. doi:10.1063/1.2739504.
- Kong, X., Papagiannakopoulos, P., Thomson, E. S., Markovic, N., and Pettersson, J. B. C. Water Accommodation and Desorption Kinetics on Ice. *Journal of Physical Chemistry A*, 118(22):3973–3979, 2014. doi:10.1021/jp503504e.
- Korner, U. and Sonnemann, G. Global three-dimensional modeling of the water vapor concentration of the mesosphere-mesopause region and implications with respect to the noctilucent cloud region. *Journal of Geophysical Research - Atmospheres*, 106(D9):9639–9651, 2001. doi:10.1029/2000JD900744.

- Kouchi, A., Yamamoto, T., Kozasa, T., Kuroda, T., and Greenberg, J. M. Conditions for condensation and preservation of amorphous ice and crystallinity of astrophysical ices. *Astronomy and Astrophysics*, 290(3):1009–1018, 1994.
- Kuhs, W. F., Bliss, D. V., and Finney, J. L. High resolution neutron powder diffraction study of ice Ic. *Journal de Physique Archives*, 48(C-1):631–636, 1987. doi:10.1051/jphyscol:1987187.
- Kuhs, W. F., Sippel, C., Falenty, A., and Hansen, T. C. Extent and relevance of stacking disorder in ice Ic. *Proceedings of the National Academy of Sciences of the United States of America*, 109(52):21259–21264, 2012. doi:10.1073/pnas.1210331110.
- Kumai, M. Hexagonal Ice and Cubic Ice at low Temperatures. *Journal of Glaciology*, 7:95–108, 1968. doi:10.3189/S0022143000020438.
- Lapshin, V., Yablokov, M., and Palei, A. Vapor pressure over a charged drop. *Russian Journal of Physical Chemistry*, 76(10):1727–1729, 2002.
- Le Texier, H., Solomon, S. C., and Garcia, R. R. The role of molecular-hydrogen and methane oxidation in the water-vapor budget of the stratosphere. *Quarterly Journal of the Royal Meteorological Society*, 114(480):281–295, 1988. doi:10.1002/qj.49711448002.
- Lengyel, J., Kocisek, J., Poterya, V., Pysanenko, A., Svrckova, P., Farnik, M., Zaouris, D. K., and Fedor, J. Uptake of atmospheric molecules by ice nanoparticles: Pickup cross sections. *Journal of Chemical Physics*, 137(3), 2012. doi:10.1063/1.4733987.
- Leslie, R. C. Sky Glows. *Nature*, 1885. doi:10.1038/032245a0.
- Leslie, R. C. Luminous Clouds. *Nature*, 34:264, 1886. doi:10.1038/034264b0.
- Lewis, M., Wu, Z., and Glaser, R. Polarizabilities of carbon dioxide and carbodiimide. Assessment of theoretical model dependencies on dipole polarizabilities and dipole polarizability anisotropies. *Journal of Physical Chemistry - A*, 104(48):11355–11361, 2000. doi:10.1021/jp002927r.
- Listowski, C., Maeaettaenen, A., Riipinen, I., Montmessin, F., and Lefevre, F. Near-pure vapor condensation in the Martian atmosphere: CO₂ ice crystal growth. *Journal of Geophysical Research - Planets*, 118(10):2153–2171, 2013. doi:10.1002/jgre.20149.
- Listowski, C., Maeaettaenen, A., Montmessin, F., Spiga, A., and Lefevre, F. Modeling the microphysics of CO₂ ice clouds within wave-induced cold pockets in the martian mesosphere. *Icarus*, 237:239–261, 2014. doi:10.1016/j.icarus.2014.04.022.
- Loerting, T., Bauer, M., Kohl, I., Watschinger, K., Winkel, K., and Mayer, E. Cryoflotation: Densities of Amorphous and Crystalline Ices. *Journal of Physical Chemistry B*, 115(48):14167–14175, 2011. doi:10.1021/jp204752w.

- Luebken, F.-J., Lautenbach, J., Hoeffner, J., Rapp, M., and Zecha, M. First continuous temperature measurements within polar mesosphere summer echoes. *Journal of Atmospheric and Solar - Terrestrial Physics*, 71(3-4, SI):453–463, 2009. doi:10.1016/j.jastp.2008.06.001.
- Luna, R., Millan, C., Santonja, C., and Satorre, M. A. Triple test under high vacuum conditions to control the reliability of thin ice film accretion and desorption for astrophysical applications. *Vacuum*, 83(6):942–948, 2009. doi:10.1016/j.vacuum.2008.10.007.
- Lupi, L., Hudait, A., Peters, B., Gr nwald, M., Gotchy Mullen, R., Nguyen, A. H., and Molinero, V. Role of stacking disorder in ice nucleation. *Nature*, 551:218, 2017. doi:10.1038/nature24279.
- Macfarlane, D. R. and Angell, C. A. Nonexistent glass-transition for amorphous solid water. *Journal of Physical Chemistry*, 88(4):759–762, 1984. doi:10.1021/j150648a029.
- Magalhaes, J., Schofield, J., and Seiff, A. Results of the Mars Pathfinder atmospheric structure investigation. *Journal of Geophysical Research - Planets*, 104(E4):8943–8955, 1999. doi:10.1029/1998JE900041 .
- Majima, T., Santambrogio, G., Bartels, C., Terasaki, A., Kondow, T., Meinen, J., and Leisner, T. Spatial distribution of ions in a linear octopole radio-frequency ion trap in the space-charge limit. *Physical Review A*, 85(5), 2012. doi:10.1103/PhysRevA.85.053414.
- Malkin, T. L., Murray, B. J., Salzmann, C. G., Molinero, V., Pickering, S. J., and Whale, T. F. Stacking disorder in ice I. *Physical Chemistry Chemical Physics*, 17(1):60–76, 2015. doi:10.1039/c4cp02893g.
- Maltagliati, L., Montmessin, F., Fedorova, A., Korablev, O., Forget, F., and Bertaux, J. L. Evidence of Water Vapor in Excess of Saturation in the Atmosphere of Mars. *Science*, 333(6051):1868–1871, 2011. doi:10.1126/science.1207957.
- Maltagliati, L., Montmessin, F., Korablev, O., Fedorova, A., Forget, F., Maeaettaenen, A., Lefevre, F., and Bertaux, J. L. Annual survey of water vapor vertical distribution and water-aerosol coupling in the martian atmosphere observed by SPICAM/MEx solar occultations. *Icarus*, 223(2):942–962, 2013. doi:10.1016/j.icarus.2012.12.012.
- Mangan, T. P., Salzmann, C. G., Plane, J. M. C., and Murray, B. J. CO₂ ice structure and density under Martian atmospheric conditions. *Icarus*, 294:201–208, 2017. doi:10.1016/j.icarus.2017.03.012.
- Marti, J. and Mauersberger, K. A survey and new measurements of ice vapor-pressure at temperatures between 170 and 20 K. *Geophysical Research Letters*, 20(5):363–366, 1993. doi:10.1029/93GL00105.

- Mauersberger, K. and Krankowsky, D. Vapor pressure above ice at temperatures below 170 K. *Geophysical Research Letters*, 30(3), 2003. doi:10.1029/2002GL016183.
- Mayer, E. and Hallbrucker, A. Cubic ice from liquid water. *Nature*, 325(6105):601–602, 1987. doi:10.1038/325601a0.
- Mayer, E. and Pletzer, R. Astrophysical implications of amorphous ice - a microporous solid. *Nature*, 319(6051):298–301, 1986. doi:10.1038/319298a0.
- Mc Millan, J. A. and Los, S. C. Vitreous ice - irreversible transformations during warm-up. *Nature*, 206(4986):806–807, 1965. doi:10.1038/206806a0.
- McCleese, D. J., Heavens, N. G., Schofield, J. T., Abdou, W. A., Bandfield, J. L., Calcutt, S. B., Irwin, P. G. J., Kass, D. M., Kleinbohl, A., Lewis, S. R., Paige, D. A., Read, P. L., Richardson, M. I., Shirley, J. H., Taylor, F. W., Teanby, N., and Zurek, R. W. Structure and dynamics of the Martian lower and middle atmosphere as observed by the Mars Climate Sounder: Seasonal variations in zonal mean temperature, dust, and water ice aerosols. *Journal of Geophysical Research - Planets*, 115, 2010. doi:10.1029/2010JE003677.
- Megner, L. and Gumbel, J. Charged meteoric particles as ice nuclei in the mesosphere: Part 2 A feasibility study. *Journal of Atmospheric and Solar - Terrestrial Physics*, 71(12):1236–1244, 2009. doi:10.1016/j.jastp.2009.05.002.
- Megner, L., Gumbel, J., Rapp, M., and Siskind, D. E. Reduced meteoric smoke particle density at the summer pole - Implications for mesospheric ice particle nucleation. *Advances in Space Research*, 41(1):41–49, 2008a. doi:10.1016/j.asr.2007.09.006.
- Megner, L., Siskind, D. E., Rapp, M., and Gumbel, J. Global and temporal distribution of meteoric smoke: A two-dimensional simulation study. *Journal of Geophysical Research - Atmospheres*, 113(D3), 2008b. doi:10.1029/2007JD009054.
- Meinen, J., Khasminkaya, S., Ruehl, E., Baumann, W., and Leisner, T. The TRAPS Apparatus: Enhancing Target Density of Nanoparticle Beams in Vacuum for X-ray and Optical Spectroscopy. *Aerosol Science and Technology*, 44(4):316–328, 2010. doi:10.1080/02786821003639692.
- Meinen, J. *TRAPS - The key to atmospheric nano-science*. PhD thesis, Ruperto-Carola University of Heidelberg, 2010.
- Meyers, C. H. and Van Dusen, M. S. The vapor pressure of liquid and solid carbon dioxide. *Bureau of Standards Journal Research*, 10:381–412, 1933.
- Mitchell, E. H., Raut, U., Teolis, B. D., and Baragiola, R. A. Porosity effects on crystallization kinetics of amorphous solid water: Implications for cold icy objects in the outer solar system. *Icarus*, 285:291–299, 2017. doi:10.1016/j.icarus.2016.11.004.

- Mitterdorfer, C., Bauer, M., Youngs, T. G. A., Bowron, D. T., Hill, C. R., Fraser, H. J., Finney, J. L., and Loerting, T. Small-angle neutron scattering study of micropore collapse in amorphous solid water. *Physical Chemistry Chemical Physics*, 16(30): 16013–16020, 2014. doi:10.1039/c4cp00593g.
- Montmessin, F., Gondet, B., Bibring, J. P., Langevin, Y., Drossart, P., Forget, F., and Fouchet, T. Hyperspectral imaging of convective CO₂ ice clouds in the equatorial mesosphere of Mars. *Journal of Geophysical Research - Planets*, 112(E11), 2007. doi:10.1029/2007JE002944.
- Montmessin, F., Bertaux, J.-L., Quemerais, E., Korablev, O., Rannou, P., Forge, F., Perrier, S., Fussen, D., Lebonnois, S., Reberac, A., and Dimarellis, E. Subvisible CO₂ ice clouds detected in the mesosphere of Mars. *Icarus*, 183(2):403–410, 2006. doi:10.1016/j.icarus.2006.03.015.
- Morishige, K., Yasunaga, H., and Uematsu, H. Stability of Cubic Ice in Mesopores. *Journal of Physical Chemistry C*, 113(8):3056–3061, 2009. doi:10.1021/jp8088935.
- Morris, R., Golden, D., Bell, J., Shelfer, T., Scheinost, A., Hinman, N., Furniss, G., Mertzman, S., Bishop, J., Ming, D., Allen, C., and Britt, D. Mineralogy, composition, and alteration of Mars Pathfinder rocks and soils: Evidence from multi-spectral, elemental, and magnetic data on terrestrial analogue, SNC meteorite, and Pathfinder samples. *Journal of Geophysical Research - Planets*, 105(E1):1757–1817, 2000. doi:10.1029/1999JE001059.
- Murphy, D. and Koop, T. Review of the vapour pressures of ice and supercooled water for atmospheric applications. *Quarterly Journal of the Royal Meteorological Society*, 131(608, B):1539–1565, 2005. doi:10.1256/qj.04.94.
- Murray, B. J. and Jensen, E. J. Homogeneous nucleation of amorphous solid water particles in the upper mesosphere. *Journal of Atmospheric and Solar - Terrestrial Physics*, 72(1):51–61, 2010. doi:10.1016/j.jastp.2009.10.007.
- Murray, B. J., Malkin, T. L., and Salzmann, C. G. The crystal structure of ice under mesospheric conditions. *Journal of Atmospheric and Solar - Terrestrial Physics*, 127 (SI):78–82, 2015. doi:10.1016/j.jastp.2014.12.005.
- Määttänen, A., Vehkamäki, H., Lauri, A., Merikallio, S., Kauhanen, J., Savijärvi, H., and Kulmala, M. Nucleation studies in the Martian atmosphere. *Journal of Geophysical Research - Planets*, 110(E2), 2005. doi:10.1029/2004JE002308.
- Määttänen, A., Montmessin, F., Gondet, B., Scholten, F., Hoffmann, H., Gonzalez-Galindo, F., Spiga, A., Forget, F., Hauber, E., Neukum, G., Bibring, J. P., and Bertaux, J. L. Mapping the mesospheric CO₂ clouds on Mars: MEx/OMEGA and MEx/HRSC observations and challenges for atmospheric models. *Icarus*, 209(2): 452–469, 2010. doi:10.1016/j.icarus.2010.05.017.

- Määttänen, A., Vehkamäki, H., Lauri, A., Napari, I., and Kulmala, M. Two-component heterogeneous nucleation kinetics and an application to Mars. *Journal of Chemical Physics*, 127(13), 2007. doi:10.1063/1.2770737.
- Nachbar, M., Duft, D., and Leisner, T. The vapor pressure over nano-crystalline ice. *Atmospheric Chemistry and Physics*, 18(5):3419–3431, 2018a. doi:10.5194/acp-18-3419-2018.
- Nachbar, M. Laboratory experiments on ice nucleation and growth rates on meteoric smoke particles at mesospheric conditions. Master's thesis, Institute of Environmental Physics, University of Heidelberg, 2014.
- Nachbar, M., Duft, D., Kiselev, A., and Leisner, T. Composition, Mixing State and Water Affinity of Meteoric Smoke Analogue Nanoparticles Produced in a Non-Thermal Microwave Plasma Source. *Zeitschrift fuer Physikalische Chemie*, 2018b. doi:10.1515/zpch-2017-1053.
- Nachbar, M., Duft, D., Mangan, T. P., Martin, J. C. G., Plane, J. M. C., and Leisner, T. Laboratory measurements of heterogeneous CO₂ ice nucleation on nanoparticles under conditions relevant to the Martian mesosphere. *Journal of Geophysical Research - Planets*, 121(5):753–769, 2016. doi:10.1002/2015JE004978.
- Nadeem, K., Krenn, H., Traussnig, T., Wuerschum, R., Szabo, D. V., and Letofsky-Papst, I. Spin-glass freezing of maghemite nanoparticles prepared by microwave plasma synthesis. *Journal of Applied Physics*, 111(11), 2012. doi:10.1063/1.4724348.
- Navrotsky, A., Mazeina, L., and Majzlan, J. Size-driven structural and thermodynamic complexity in iron oxides. *Science*, 319(5870):1635–1638, 2008. doi:10.1126/science.1148614.
- Pertsev, N., Dalin, P., Perminov, V., Romejko, V., Dubietis, A., Balciunas, R., Cernis, K., and Zalcik, M. Noctilucent clouds observed from the ground: sensitivity to mesospheric parameters and long-term time series. *Earth Planets and Space*, 66, 2014. doi:10.1186/1880-5981-66-98.
- Phebus, B. D., Johnson, A. V., Mar, B., Stone, B. M., Colaprete, A., and Iraci, L. T. Water ice nucleation characteristics of JSC Mars-1 regolith simulant under simulated Martian atmospheric conditions. *Journal of Geophysical Research - Planets*, 116, 2011. doi:10.1029/2010JE003699.
- Plane, J. M. C., Carrillo-Sanchez, J. D., Mangan, T. P., Crismani, M. M. J., Schneider, N. M., and Määttänen, A. Meteoric Metal Chemistry in the Martian Atmosphere. *Journal of Geophysical Research: Planets*, 2018. doi:10.1002/2017JE005510. 2017JE005510.

- Plane, J. The role of sodium bicarbonate in the nucleation of noctilucent clouds. *Annales Geophysicae - Atmospheres Hydrospheres and Space Science*, 18(7):807–814, 2000. doi:10.1007/s005850000198.
- Plane, J. M. C. Cosmic dust in the earth's atmosphere. *Chemical Society Reviews*, 41(19):6507–6518, 2012. doi:10.1039/c2cs35132c.
- Plane, J. M. C., Saunders, R. W., Hedin, J., Stegman, J., Khaplanov, M., Gumbel, J., Lynch, K. A., Bracikowski, P. J., Gelinias, L. J., Friedrich, M., Blindheim, S., Gausa, M., and Williams, B. P. A combined rocket-borne and ground-based study of the sodium layer and charged dust in the upper mesosphere. *Journal of Atmospheres and Solar - Terrestrial Physics*, 118(B, SI):151–160, 2014. doi:10.1016/j.jastp.2013.11.008.
- Plane, J. M. C., Feng, W., and Dawkins, E. C. M. The Mesosphere and Metals: Chemistry and Changes. *Chemical Reviews*, 115(10):4497–4541, 2015. doi:10.1021/cr500501m.
- Pruppacher, H. R. and Klett, J. D. *Microphysics of Clouds and Precipitation*. Springer, second revised and expanded edition, 2010. doi:DOI 10.1007/978-0-306-48100-0.
- Ranke, W. Precursor kinetics of dissociative water adsorption on the Si(001) surface. *Surface Science*, 369(1-3):137–145, 1996. doi:10.1016/S0039-6028(96)00912-0.
- Ranke, W. and Xing, Y. Kinetics of dissociative water adsorption on stepped Si(001), on Si(115), Si(113), Si(5,5,12) and Si(112). *Surface Science*, 381(1):1–11, 1997. doi:10.1016/S0039-6028(97)00064-2.
- Rapp, M. and Lubken, F. Polar mesosphere summer echoes (PMSE): review of observations and current understanding. *Atmospheric Chemistry and Physics*, 4:2601–2633, 2004. doi:10.5194/acp-4-2601-2004.
- Rapp, M. and Thomas, G. Modeling the microphysics of mesospheric ice particles: Assessment of current capabilities and basic sensitivities. *Journal of Atmospheric and Solar - Terrestrial Physics*, 68(7):715–744, 2006. doi:10.1016/j.jastp.2005.10.015.
- Rapp, M., Lubken, F., Mullemann, A., Thomas, G., and Jensen, E. Small-scale temperature variations in the vicinity of NLC: Experimental and model results. *Journal of Geophysical Research - Atmospheres*, 107(D19), 2002. doi:10.1029/2001JD001241.
- Rapp, M., Plane, J. M. C., Strelnikov, B., Stober, G., Ernst, S., Hedin, J., Friedrich, M., and Hoppe, U. P. In situ observations of meteor smoke particles (MSP) during the Geminids 2010: constraints on MSP size, work function and composition. *Annales Geophysicae*, 30(12):1661–1673, 2012. doi:10.5194/angeo-30-1661-2012.
- Raut, U., Fama, M., Teolis, B. D., and Baragiola, R. A. Characterization of porosity in vapor-deposited amorphous solid water from methane adsorption. *Journal of Chemical Physics*, 127(20), 2007. doi:10.1063/1.2796166.

- Robertson, S., Dickson, S., Horanyi, M., Sternovsky, Z., Friedrich, M., Janches, D., Megner, L., and Williams, B. Detection of meteoric smoke particles in the mesosphere by a rocket-borne mass spectrometer. *Journal of Atmospheric and Solar - Terrestrial Physics*, 118(B, SI):161–179, 2014. doi:10.1016/j.jastp.2013.07.007.
- Roble, R. G. and Dickinson, R. E. How will changes in carbon dioxide and methane modify the mean structure of the mesosphere and thermosphere? *Geophysical Research Letters*, 16(12):1441–1444, 1989. doi:10.1029/GL016i012p01441.
- Roedel, W. and Wagner, T. *Physik unserer Umwelt: Die Atmsophaere*, volume 4. Springer, 2011. doi:10.1007/978-3-642-15729-5.
- Rong, P. P., Yue, J., Russell, J. M., III, Lumpe, J. D., Gong, J., Wu, D. L., and Randall, C. E. Horizontal winds derived from the polar mesospheric cloud images as observed by the CIPS instrument on the AIM satellite. *Journal of Geophysical Research - Atmospheres*, 120(11):5564–5584, 2015. doi:10.1002/2014JD022813.
- Sack, N. J. and Baragiola, R. A. Sublimation of vapor-despoited water below 170 K, and its dependence on growth-conditions. *Physical Review B*, 48(14):9973–9978, 1993. doi:10.1103/PhysRevB.48.9973.
- Sandford, S. A. and Allamandola, L. J. The Physical and Infrared Spectral Properties of CO₂ in Astrophysical Ice Analogues. *Astrophysical Journal*, 355:357–372, 1990. doi:10.1086/168770.
- Schmidt, F., Baumgarten, G., Berger, U., Fiedler, J., and Luebken, F.-J. Local Time Dependence of Polar Mesospheric Clouds: A model study. *Atmospheric Chemistry and Physics Discussions*, 2017:1–22, 2017. doi:10.5194/acp-2017-772.
- Seele, C. and Hartogh, P. Water vapor of the polar middle atmosphere: Annual variation and summer mesosphere conditions as observed by ground-based microwave spectroscopy. *Geophysical Research Letters*, 26(11):1517–1520, 1999. doi:10.1029/1999GL900315.
- Sepulveda, A., Leon-Gutierrez, E., Gonzalez-Silveira, M., Rodriguez-Tinoco, C., Clavaguera-Mora, M. T., and Rodriguez-Viejo, J. Glass transition in ultrathin films of amorphous solid water. *Journal of Chemical Physics*, 137(24), 2012. doi:10.1063/1.4771964.
- Shallcross, F. V. and Carpenter, G. B. X-Ray Diffraction Study of the Cubic Phase of Ice. *The Journal of Chemical Physics*, 26:782–784, 1957. doi:10.1063/1.1743404.
- Shilling, J. E., Tolbert, M. A., Toon, O. B., Jensen, E. J., Murray, B. J., and Bertram, A. K. Measurements of the vapor pressure of cubic ice and their implications for atmospheric ice clouds. *Geophysical Research Letters*, 33(17), 2006. doi:10.1029/2006GL026671.

- Smith, P., Bell, J., Bridges, N., Britt, D., Gaddis, L., Greeley, R., Keller, H., Herkenhoff, K., Jaumann, R., Johnson, J., Kirk, R., Lemmon, M., Maki, J., Malin, M., Murchie, S., Oberst, J., Parker, T., Reid, R., Sablotny, R., Soderblom, L., Stoker, C., Sullivan, R., Thomas, N., Tomasko, M., Ward, W., and Wegryn, E. Results from the Mars Pathfinder camera. *Science*, 278(5344):1758–1765, 1997. doi:10.1126/science.278.5344.1758.
- Smith, R. S., Matthiesen, J., Knox, J., and Kay, B. D. Crystallization Kinetics and Excess Free Energy of H₂O and D₂O Nanoscale Films of Amorphous Solid Water. *Journal of Physical Chemistry A*, 115(23):5908–5917, 2011. doi:10.1021/jp110297q.
- Smith, R., Huang, C., Wong, E., and Kay, B. Desorption and crystallization kinetics in nanoscale thin films of amorphous water ice. *Surface Science*, 367(1):L13–L18, 1996. doi:10.1016/S0039-6028(96)00943-0.
- Sneh, O., Cameron, M., and George, S. Adsorption and desorption kinetics of H₂O on a fully hydroxylated SiO₂ surface. *Surface Science*, 364(1):61–78, 1996. doi:10.1016/0039-6028(96)00592-4.
- Souda, R. Glass-liquid transition of carbon dioxide and its effect on water segregation. *Journal of Physical Chemistry B*, 110(36):17884–17888, 2006. doi:10.1021/jp061400x.
- Speedy, R. Evidence for a new phase of water - water II. *Journal of Physical Chemistry*, 96(5):2322–2325, 1992. doi:10.1021/j100184a056.
- Speedy, R., Debenedetti, P., Smith, R., Huang, C., and Kay, B. The evaporation rate, free energy, and entropy of amorphous water at 150 K. *Journal of Physical Chemistry*, 105(1):240–244, 1996. doi:10.1063/1.471869.
- Spiga, A., Gonzalez-Galindo, F., Lopez-Valverde, M. A., and Forget, F. Gravity waves, cold pockets and CO₂ clouds in the Martian mesosphere. *Geophysical Research Letters*, 39, 2012. doi:10.1029/2011GL050343.
- Stevens, M. H., Siskind, D. E., Evans, J. S., Jain, S. K., Schneider, N. M., Deighan, J., Stewart, A. I. F., Crismani, M., Stiepen, A., Chaffin, M. S., McClintock, W. E., Holsclaw, G. M., Lefevre, F., Lo, D. Y., Clarke, J. T., Montmessin, F., and Jakosky, B. M. Martian mesospheric cloud observations by IUVS on MAVEN: Thermal tides coupled to the upper atmosphere. *Geophysical Research Letters*, 44(10):4709–4715, 2017. doi:10.1002/2017GL072717.
- Stevenson, K., Kimmel, G., Dohnalek, Z., Smith, R., and Kay, B. Controlling the morphology of amorphous solid water. *Science*, 283(5407):1505–1507, 1999. doi:10.1126/science.283.5407.1505.

- Sugisaki, M., Suga, H., and Seki, S. Calorimetric study of glassy state .4. heat capacities of glassy water and cubic ice. *Bulletin of the Chemical Society of Japan*, 41(11): 2591+, 1968. doi:10.1246/bcsj.41.2591.
- Tanaka, H. Thermodynamic stability and negative thermal expansion of hexagonal and cubic ices. *Journal of Chemical Physics*, 108(12):4887–4893, 1998. doi:10.1063/1.475897.
- Tanaka, H. and Okabe, I. Thermodynamic stability of hexagonal and cubic ices. *Chemical Physics Letters*, 259(5-6):593–598, 1996. doi:10.1016/0009-2614(96)00824-X.
- Thomas, G. E., Olivero, J. J., Jensen, E. J., Schroeder, W., and Toon, O. B. Relation between increasing methane and the presence of ice clouds at the mesopause. *Nature*, 338(6215):490–492, 1989. doi:10.1038/338490a0.
- Thomas, G. E. Mesospheric clouds and the physics of the mesopause region. *Reviews of Geophysics*, 29(4):553–575, 1991. doi:10.1029/91RG01604.
- Thomas, G. E., Olivero, J. J., Deland, M., and Shettle, E. P. P. Comment on Are noctilucent clouds truly a Miner’s Canary for Global Change? *Eos, Transactions American Geophysical Union*, 84(36):352–353, 2003. doi:10.1029/2003EO360008.
- Thomas, G. and Olivero, J. Noctilucent clouds as possible indicators of global change in the mesosphere. In *Greenhouse gases, Aerosols and Dust*, volume 28, pages 937–946. Elsevier Science, 2001. doi:10.1016/S0273-1177(01)80021-1.
- Thomson, E. S., Kong, X., Papagiannakopoulos, P., and Pettersson, J. B. C. Deposition-mode ice nucleation reexamined at temperatures below 200 K. *Atmospheric Chemistry and Physics*, 15(4):1621–1632, 2015. doi:10.5194/acp-15-1621-2015.
- Thuermer, K. and Nie, S. Formation of hexagonal and cubic ice during low-temperature growth. *Proceedings of the National Academy of Sciences of the United States of America*, 110(29):11757–11762, 2013. doi:10.1073/pnas.1303001110.
- Trainer, M. G., Toon, O. B., and Tolbert, M. A. Measurements of Depositional Ice Nucleation on Insoluble Substrates at Low Temperatures: Implications for Earth and Mars. *Journal of Physical Chemistry - C*, 113(6):2036–2040, 2009. doi:10.1021/jp805140p.
- Trokhimovskiy, A., Fedorova, A., Korablev, O., Montmessin, F., Bertaux, J.-L., Rodin, A., and Smith, M. D. Mars’ water vapor mapping by the SPICAM IR spectrometer: Five martian years of observations. *Icarus*, 251:50–64, 2015. doi:10.1016/j.icarus.2014.10.007.

- Turco, R. P., Toon, O. B., Whitten, R. C., Keesee, R. G., and Hollenbach, D. Noctilucent clouds - simulation studies of their genesis, properties and global influences. *Planetary and Space Science*, 30(11):1147–1181, 1982. doi:10.1016/0032-0633(82)90126-X.
- Vehkamaeki, H., Maeettaenen, A., Lauri, A., Napari, I., and Kulmala, M. Technical note: The heterogeneous zeldovich factor. *Atmospheric Chemistry and Physics*, 7: 309–313, 2007. doi:10.5194/acp-7-309-2007.
- Venables, J. A., Spiller, G. D. T., and Hanbucken, M. Nucleation and Growth of Thin-Films. *Reports on Progress in Physics*, 47(4):399–459, 1984. doi:10.1088/0034-4885/47/4/002.
- Vincendon, M., Pilorget, C., Gondet, B., Murchie, S., and Bibring, J.-P. New near-IR observations of mesospheric CO₂ and H₂O clouds on Mars. *Journal of Geophysical Research - Planets*, 116, 2011. doi:10.1029/2011JE003827.
- Vins, V., Fransen, M., Hykl, J., and Hruby, J. Surface Tension of Supercooled Water Determined by Using a Counterpressure Capillary Rise Method. *Journal of Physical Chemistry B*, 119(17):5567–5575, 2015. doi:10.1021/acs.jpcc.5b00545.
- Vins, V., Hosek, J., Hykl, J., and Hruby, J. Surface Tension of Supercooled Water: Inflection Point-Free Course down to 250 K Confirmed Using a Horizontal Capillary Tube. *Journal of Chemical and Engineering Data*, 62(11):3823–3832, 2017. doi:10.1021/acs.jced.7b00519.
- von Zahn, U. Are noctilucent clouds a Miner’s Canary for global change? *Eos, Transactions American Geophysical Union*, 84(28):261–264, 2003. doi:10.1029/2003EO280001.
- Vondrak, T., Plane, J. M. C., Broadley, S., and Janches, D. A chemical model of meteoric ablation. *Atmospheric Chemistry and Physics*, 8(23):7015–7031, 2008. doi:10.5194/acp-8-7015-2008.
- Wagner, W. International equations for the pressure along the melting and along the sublimation curve of ordinary water substance. *Journal of Physical and Chemical Reference Data*, 23(3):515–525, 1994.
- Wagner, W., Riethmann, T., Feistel, R., and Harvey, A. H. New Equations for the Sublimation Pressure and Melting Pressure of H₂O Ice Ih. *Journal of Physical and Chemical Reference Data*, 40(4), 2011. doi:10.1063/1.3657937.
- Weida, M., Sperhac, J., and Nesbitt, D. Sublimation dynamics of CO₂ thin films: A high resolution diode laser study of quantum state resolved sticking coefficients. *Journal of Chemical Physics*, 105(2):749–766, 1996. doi:10.1063/1.472814.

- Weller, R., Levin, I., Schmithuesen, D., Nachbar, M., Asseng, J., and Wagenbach, D. On the variability of atmospheric Rn-222 activity concentrations measured at Neumayer, coastal Antarctica. *Journal Chemistry and Physics*, 14(8):3843–3853, 2014. doi:10.5194/acp-14-3843-2014.
- Whalley, C. L. and Plane, J. M. C. Meteoric ion layers in the Martian atmosphere. *Faraday Discussions*, 147:349–368, 2010. doi:10.1039/c003726e.
- Whiteway, J. A., Komguem, L., Dickinson, C., Cook, C., Illnicki, M., Seabrook, J., Popovici, V., Duck, T. J., Davy, R., Taylor, P. A., Pathak, J., Fisher, D., Carswell, A. I., Daly, M., Hipkin, V., Zent, A. P., Hecht, M. H., Wood, S. E., Tampari, L. K., Renno, N., Moores, J. E., Lemmon, M. T., Daerden, F., and Smith, P. H. Mars Water-Ice Clouds and Precipitation. *Science*, 325(5936):68–70, 2009. doi:10.1126/science.1172344.
- Wilms, H., Rapp, M., and Kirsch, A. Nucleation of mesospheric cloud particles: Sensitivities and limits. *Journal of Geophysical Research - Space Physics*, 121(3):2621–2644, 2016. doi:10.1002/2015JA021764.
- Wood, S. E. *Nucleation and Growth of CO₂ Ice Crystals in the Martian Atmosphere*. PhD thesis, University of California, Los Angeles, 1999.
- Zamith, S., de Tournadre, G., Labastie, P., and L’Hermite, J.-M. Attachment cross-sections of protonated and deprotonated water clusters. *Journal of Chemical Physics*, 138(3), 2013. doi:10.1063/1.4775401.
- Zent, A. P. and Quinn, R. C. Simultaneous adsorption of CO₂ and H₂O under Mars-like conditions and application to the evolution of the Martian climate. *Journal of Geophysical Research - Planets*, 100(E3):5341–5349, 1995. doi:10.1029/94JE01899.

Danksagung

An dieser Stelle möchte ich mich bei all denjenigen bedanken, ohne die diese Arbeit so nicht möglich gewesen wäre:

- Zu aller Erst möchte ich *Herrn Prof. Leisner* danken. Danke, dass Sie es mir ermöglicht haben meine Doktorarbeit am IMK-AAF durchzuführen. Herzlichen Dank auch für die vielen hilfreichen Anregungen bezüglich meiner Arbeit in den Gruppensitzungen.
- Ein weiterer Dank gilt meinem Betreuer, *Dr. Denis Duft*, für die gute Betreuung sowie die kritische Korrektur meiner Arbeit. Hier ist auch *Dr. Thomas Dresch* zu nennen. Ich habe sehr viel dazugelernt!
- Zudem möchte ich *Herrn Prof. Pfeilsticker* für das Gutachten der Arbeit und die wertvollen Anmerkungen danken.
- Ein ganz besonderer Dank gilt meiner Verlobten, *Julia*. Danke, dass Du immer Verständnis hattest wenn ich wegen der Arbeit etwas weniger Freizeit hatte. Danke für das Korrekturlesen meiner Arbeit und die super Unterstützung in der stressigen Schlussphase. Danke, dass Du immer für mich da bist!
- Zu aller Letzt möchte ich meiner Familie und meinen Freunden danken, ohne deren Unterstützung ich das Physikstudium und diese Arbeit nicht annähernd so sorglos, gelassen und mit Freude hätte durchführen könnte.

Mein Dank gilt natürlich auch all denjenigen, welche ich nicht gesondert genannt beziehungsweise vergessen habe, die jedoch in irgendeiner Weise eine Hilfe bezüglich der Fertigstellung dieser Arbeit waren.